

UNIVERSITY OF ZÜRICH

MASTER THESIS

---

**Exceptional Topological Insulator:  
Realization of a Weyl Semimetal using Topolectric Metamaterials**

---

*Author*  
Nelson Herbosa Labiano

*Supervisors*  
Prof. Dr. Titus Neupert  
Dr. M. Michael Denner

September 9, 2024

# Table of Contents

|            |   |           |
|------------|---|-----------|
| <b>I</b>   | <b>Introduction</b>                           | <b>3</b>  |
| <b>II</b>  | <b>Theory</b>                                 | <b>5</b>  |
| <b>1</b>   | <b>Hermitian Topology</b>                     | <b>5</b>  |
| 1.1        | Chern Insulator . . . . .                     | 6         |
| 1.2        | 3D Topological Insulators . . . . .           | 9         |
| 1.3        | Weyl Semimetals . . . . .                     | 10        |
| <b>2</b>   | <b>Non-Hermitian Topology</b>                 | <b>17</b> |
| 2.1        | Non-Hermitian Energy Gaps . . . . .           | 17        |
| 2.2        | Exceptional Points . . . . .                  | 18        |
| 2.3        | Complex Vortices . . . . .                    | 18        |
| 2.4        | Non-Hermitian Skin Effect . . . . .           | 19        |
| 2.5        | Exceptional Topological Insulator . . . . .   | 20        |
| <b>3</b>   | <b>Topoelectrical Circuits</b>                | <b>24</b> |
| 3.1        | Circuit Laplacian . . . . .                   | 24        |
| 3.2        | Circuit Simulations . . . . .                 | 26        |
| 3.3        | Bandstructure Simulations . . . . .           | 26        |
| 3.4        | Impedance Simulations . . . . .               | 27        |
| <b>4</b>   | <b>Circuit Configurations</b>                 | <b>28</b> |
| 4.1        | Weyl Circuit . . . . .                        | 28        |
| 4.2        | Trivial Non-Hermitian Configuration . . . . . | 30        |
| 4.3        | Non-Hermitian TI Configuration . . . . .      | 31        |
| <b>III</b> | <b>Experimental Setup</b>                     | <b>34</b> |
| <b>5</b>   | <b>ETI Circuit Board</b>                      | <b>34</b> |
| 5.1        | Multiplexer Boards . . . . .                  | 36        |
| <b>6</b>   | <b>Board Measurements</b>                     | <b>38</b> |
| 6.1        | Impedance Measurements . . . . .              | 38        |
| 6.2        | Frequency Determination . . . . .             | 39        |
| 6.3        | Bandstructure Measurements . . . . .          | 40        |
| 6.4        | Surface Propagation . . . . .                 | 41        |
| <b>IV</b>  | <b>Experimental Findings</b>                  | <b>42</b> |
| <b>7</b>   | <b>Weyl Semimetal Measurements</b>            | <b>42</b> |
| 7.1        | 8-Boards . . . . .                            | 42        |
| 7.2        | 6-Boards . . . . .                            | 46        |

|  |           |
|--|-----------|
| <b>8 Measurement Simplification</b>    | <b>49</b> |
| 8.1 Flat Band Ribbons . . . . .        | 49        |
| 8.2 Multiplexer Measurements . . . . . | 50        |
| <b>9 Disorder</b>                      | <b>53</b> |
| 9.1 Component Deviations . . . . .     | 54        |
| 9.2 Current Stabilization . . . . .    | 60        |
| <b>10 Layout Influence</b>             | <b>61</b> |
| <b>V Conclusion</b>                    | <b>69</b> |
| <b>References</b>                      | <b>71</b> |

# Part I

## Introduction

Weyl semimetals (WSMs) are a relatively new class of materials that have been the subject of significant scientific interest in recent years. They are a type of topological semimetal, which means that they have unique electronic properties that are protected by the topology of their band structure [1]. One of the key features of WSMs is their unique band structure exhibiting pairs of Weyl points, which are conical band touching points in momentum space [2]. Low energy excitations of WSMs behave as Weyl fermion quasiparticles, which are massless particle solutions of the Weyl equation [3].

The Weyl points are topologically protected and act as sources and sinks of Berry curvature [4]. As a result, for open boundary conditions (OBC), the WSM exhibits Fermi arcs connecting the pairs of Weyl points [5]. The Fermi arcs are zero energy surface states, therefore only found at the boundaries, and are also protected by topology as they are the manifestation of the Chern insulator's edge states [1]. Therefore, the Fermi arcs inherit the chirality of the Chern insulator edge states, giving rise to monodirectional edge currents [6].

Beyond their theoretical study, WSMs have gained the attention of scientists for their potential practical applications. WSMs can help improve fields such as electronics, optic and quantum computing, where the Weyl fermions and Fermi arcs can be of use [7][8][9]. Additionally, the study of WSMs can deepen the fundamental understanding of physics, possibly offering insights into exotic quantum phenomena that were once purely theoretical.

WSMs have been successfully realized experimentally by Xu *et al.* in 2015 using TaAs [10]. However, discovering and synthesizing WSMs in real materials can be challenging and for some candidates the Weyl points are too close in momentum space to be detected [5]. Metamaterials offer a promising and viable alternative to simulate WSMs, as they allow for the engineering of artificial structures with tailored properties. They can mimic the behavior of natural materials by establishing a correspondence between the description of metamaterials and quantum materials. This approach has been, for instance, successfully applied in photonic and electronic meta-materials [11][12].

This leaves two open questions: Firstly, why use a WSM and secondly, why simulate a WSM using electronic circuits if this has been done previously? The motivation lies in the ulterior motive of investigating non-Hermitian (NH) topological phases that can arise, for which WSMs form the ideal basis [13]. NH systems are quite common in various physical systems, such as open or strongly interacting systems. There, the well established Hermitian formalism can break down, giving rise to new, intrinsic NH effects [14]. Due to the dissipative nature of circuit boards using resistors, they provide a good platform, in addition to their tunability.

The scope of this thesis is focused on the realization of a WSM circuit, where the necessary theoretical and experimental concepts will be explained in Part II and Part III, respectively. Additionally, two NH circuit configurations, trivial and non-trivial, are presented. These phases can be achieved using the same circuit, however, they have not been realized experimentally due to time constraints. Therefore, the basic principles and possible observations of the NH phases are discussed in parts II and III for future endeavors. The experimental Part IV contains exclusively the results of the first stage, the Hermitian circuits, as will become apparent later, the circuit does not yet perform well enough to proceed to the NH circuits.

All data and code used in this research are available at <https://github.com/Hafefif/ETI-Master-Thesis.git>.

# Part II

## Theory

This theoretical part provides a comprehensive overview of the relevant concepts and theories used in this thesis. It begins by introducing some Hermitian topological phases such as topological insulators (TIs) and WSMs, as well as their characterization using topological invariants. Next, the concepts of NH energy gaps and the emerging NH topological phases are presented. This is then followed by the topoelectrical circuit formalism needed to understand their connection to quantum systems. We conclude with a short outline of the circuit configurations for the different phases and their characterization.

### 1 Hermitian Topology

TIs are phases of matter whose bandstructures are topologically distinct from the simplest possible insulator, the case of isolated atoms known as the atomic limit. This means that the two phases cannot be adiabatically transformed into each other, without closing the bulk energy gap. This fact leads to an interesting scenario: The bulk of a TI will exhibit a gapped, topologically non-trivial bandstructure, while the surrounding vacuum is trivially gapped, meaning that at some point, the band gap has to close. This observation is indicative of the presence of topologically protected, conducting surface states, as illustrated in Fig. 1. As a consequence, local or symmetry preserving perturbations of the system do not destroy these conducting states [15].

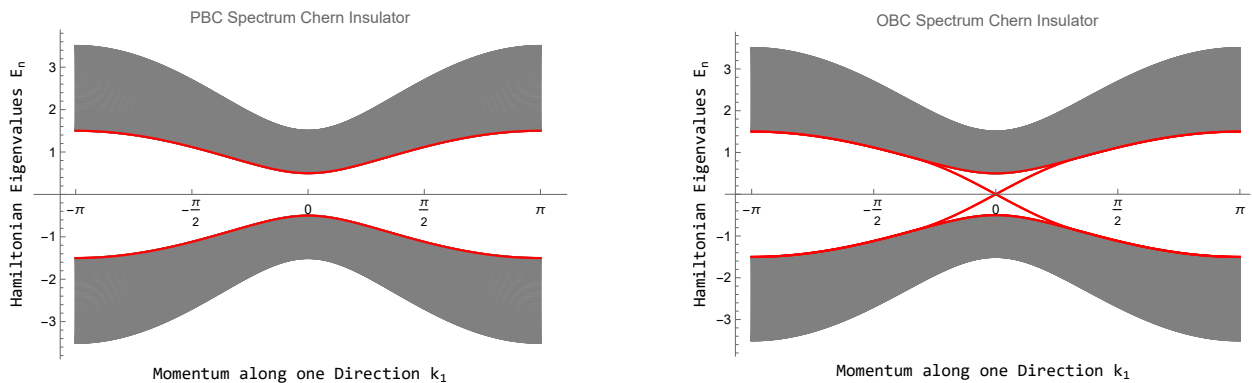


Figure 1: Example of a 2D TI with open and closed boundary conditions in one direction and the emergence of surface localized, conducting states that cross the bulk energy gap.

For Hermitian TIs, these topological phases are characterized by topological invariants such as a Chern or winding number. The underlying symmetries and dimensionality of the system determine the type and possible values of the invariants. More specifically, interesting, non-trivial phases emerge when systems feature anti-unitary and commuting symmetries, e.g. time-reversal  $\mathcal{T}$ , anti-unitary and anti-commuting symmetries, e.g. particle-hole symmetry  $\mathcal{P}$ , or unitary and anti-commuting symmetries, e.g. chiral symmetry  $\mathcal{C}$ , which is a combination of particle-hole and time-reversal symmetry [16]. The conditions for the different symmetries on the first-quantized Hamiltonian  $\mathcal{H}$  are shown in Tab. 1 [17][18][19].

Table 1: Action of the three above mentioned symmetries  $\mathcal{T}$ ,  $\mathcal{P}$  and  $\mathcal{C}$  on an Hamiltonian  $\mathcal{H}$ .  $U_i$  are the corresponding operators of the symmetries.

| Symmetry      | Condition  |
|---------------|--|
| $\mathcal{T}$ | $U_{\mathcal{T}}^{\dagger} \mathcal{H}^* U_{\mathcal{T}} = \mathcal{H}$  |
| $\mathcal{P}$ | $U_{\mathcal{P}}^{\dagger} \mathcal{H}^* U_{\mathcal{P}} = -\mathcal{H}$ |
| $\mathcal{C}$ | $U_{\mathcal{C}}^{\dagger} \mathcal{H} U_{\mathcal{C}} = -\mathcal{H}$   |

Unitary and commuting symmetries allow for a common eigenbasis of the Hamiltonian and the symmetry, which leads to a block diagonal structure whose blocks form independent sub-systems that can be transformed to trivial insulators independently [15]. Since this cannot be done for  $\mathcal{T}$ ,  $\mathcal{P}$  and  $\mathcal{C}$ , these three symmetries separate TIs into equivalency classes, as can be seen in Tab. 2 [15].

Table 2: Tenfold way of TIs showing the values of the topological invariants for different spacial dimensions of the different symmetry classes [20].

| Class | Symmetry      |               |               | Dimension      |                |                |
|-------|---------------|---------------|---------------|----------------|----------------|----------------|
|       | $\mathcal{T}$ | $\mathcal{P}$ | $\mathcal{C}$ | 1              | 2              | 3              |
| A     | 0             | 0             | 0             | 0              | $\mathbb{Z}$   | 0              |
| AIII  | 0             | 0             | 1             | $\mathbb{Z}$   | 0              | $\mathbb{Z}$   |
| AI    | 1             | 0             | 0             | 0              | 0              | 0              |
| BDI   | 1             | 1             | 1             | $\mathbb{Z}$   | 0              | 0              |
| D     | 0             | 1             | 0             | $\mathbb{Z}_2$ | $\mathbb{Z}$   | 0              |
| DIII  | -1            | 1             | 1             | $\mathbb{Z}_2$ | $\mathbb{Z}_2$ | $\mathbb{Z}$   |
| AII   | -1            | 0             | 0             | 0              | $\mathbb{Z}_2$ | $\mathbb{Z}_2$ |
| CII   | -1            | -1            | 1             | $\mathbb{Z}$   | 0              | $\mathbb{Z}_2$ |
| C     | 0             | -1            | 0             | 0              | $\mathbb{Z}$   | 0              |
| CI    | 1             | -1            | 1             | 0              | 0              | $\mathbb{Z}$   |

Where  $\mathcal{T}$  and  $\mathcal{P}$  can be absent or present individually and can square either to +1 or -1, allowing for 9 permutations. The fact that  $\mathcal{C}$  is the combination of both  $\mathcal{T}$  and  $\mathcal{P}$  means that both have to be either present or absent for  $\mathcal{C}$  to be present [15]. Additionally, since  $\mathcal{C}$  is unitary, it squares to +1, adding only one more case to complete the 10 equivalency classes known as the tenfold way [20].

In the following Secs., the relevant TIs and topological invariants are introduced to set the stage for topological semimetals, specifically the WSM.

## 1.1 Chern Insulator

The integer quantum Hall effect (IQHE) of a 2D metallic system describes the observation of a quantized, perpendicular conductivity and resistivity in the presence of an external magnetic field. Fig. 2 depicts the characteristic resistivity behaviour of an IQHE as a function of the magnetic field in the z-direction.

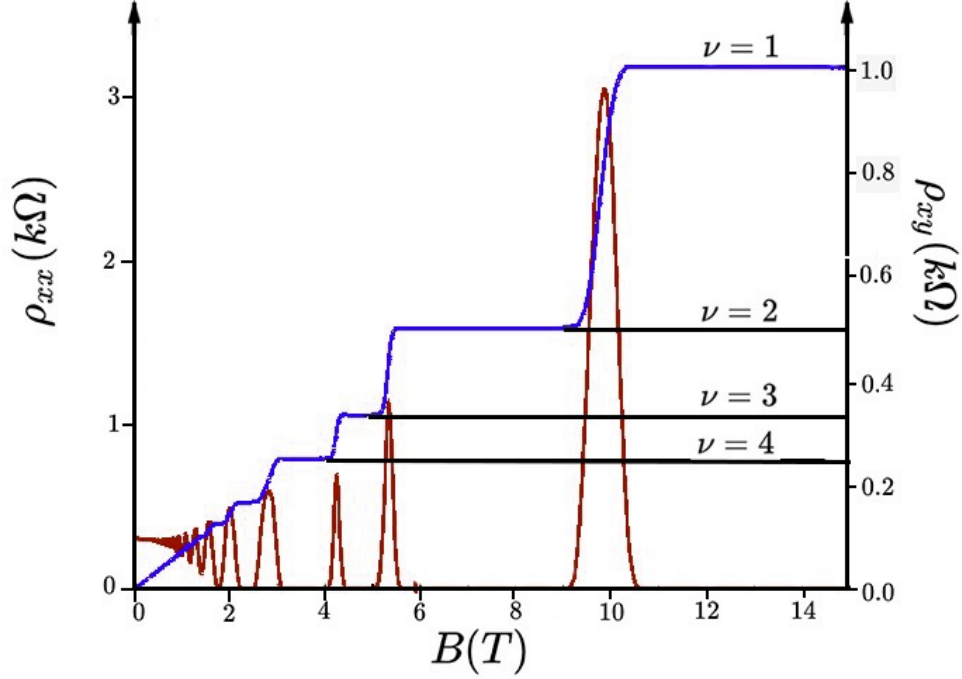


Figure 2: Illustration of the IQHE showing the resistivity along the direction of current flow  $\rho_{xx}$  in red and the perpendicular direction  $\rho_{xy}$  in blue as a function of the magnetic field  $B$ .  $\rho_{xx}$  vanishes at the plateaus of  $\rho_{xy}$ , which are labeled by the corresponding filling factor  $\nu$  [21].

The quantization can be understood to arise due to the Landau quantization of the Fermi sea. The energies of the Landau levels (LLs) are, however, very sharp. Therefore, the energy of the electrons that fill the LLs needs to match exactly. This energy is controlled by the magnetic field and thus, only certain field strengths fulfill this condition. The presence of impurities broadens the LLs spectrum by creating bound states, though, too many impurities can destroy the IQHE. Electrons can now fill the LLs even if the energy, hence  $B$ , is not exact. However, these bound states do not contribute to conduction, which enables the formation of the quantized plateaus [22].

The values of the perpendicular conductivity  $\sigma_{xy}$  are integer multiples of  $e^2/h$ , with  $e$  being the fundamental charge and  $h$  the Planck constant, where the integer corresponds to the number of filled Landau levels and is equal to the Chern number [23].

Chern insulators are 2D TIs which exhibit the IQHE. However, they don't require an external magnetic field and are therefore also known as anomalous quantum Hall insulators. Quantization is still possible due to the non-trivial topology of the energy bands, which is also characterized by the Chern number, as for the IQHE [24]. This topological non-triviality is also responsible for the presence of conducting surface states, since the Chern number counts the number of chiral edge states at a boundary, i.e. it counts the number of band crossings [25]. Fig. 3 shows an example of a Chern insulator with chiral edge states and corresponding dispersion relations.

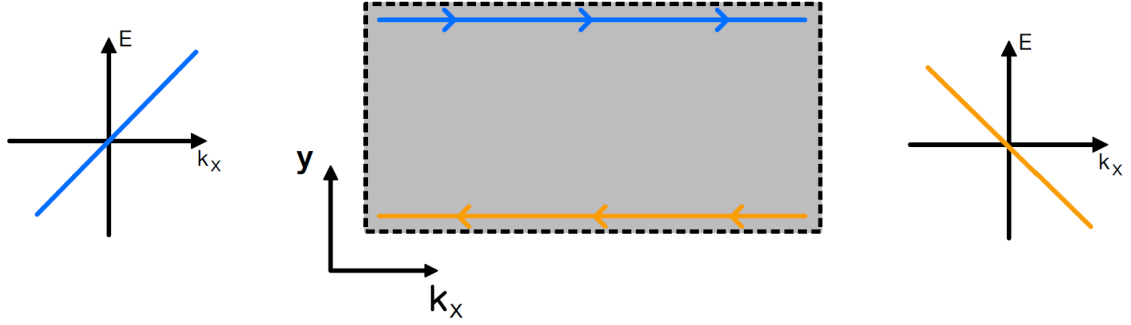


Figure 3: Illustration of a Chern insulator (middle) with periodic boundaries in x-direction and two edges in y-direction, giving rise to directional currents (blue and orange). Dispersion relations of individual edges are plotted left and right of the center panel, while the bulk spectrum is not shown, but is gapped.

### 1.1.1 Chern Number

The Chern number can be calculated as seen in Eq. (1), where  $n$  indicates the occupied band with eigenstates  $u^n(\mathbf{k})$  [26]

$$C^n = \frac{1}{2\pi} \int_{\text{BZ}} d^2k (\partial_{k_x} A_y^n(\mathbf{k}) - \partial_{k_y} A_x^n(\mathbf{k})) , \quad A_j^n(\mathbf{k}) = i \langle u^n(\mathbf{k}) | \partial_{k_j} | u^n(\mathbf{k}) \rangle . \quad (1)$$

$A_j^n(\mathbf{k})$  is known as the Berry connection or Berry potential, which can be thought of as a vector potential in momentum space that depends on the topology of the bands  $u^n(\mathbf{k})$  [27]. Thus, the expression inside the integral is the 2D curl of a vector potential, known as the Berry curvature, and acts like a magnetic field in momentum space. The integral is guaranteed to yield a multiple of  $2\pi$  due to the gauge invariance of the Berry curvature, making the Chern number integer-valued [28].

The Berry curvature also explains the anomalous quantum Hall effect nicely, as the externally applied magnetic field is not necessary due to the emerging magnetic field in momentum space as a result of the band topology. However, a non-zero Berry curvature is not sufficient to observe the anomalous IQHE.

It is worth noting that the computation of the Chern number solely requires information about the bulk bandstructure and is independent of the edges. The behaviour of the corresponding boundaries is determined by the topology of the bulk, which is known as the bulk-boundary correspondence [29].

The Chern number can be evaluated numerically, as was done for the systems studied in this project. Therefore, the momenta are not continuous parameters anymore, but rather discretized. This numerical approach therefore requires an eigenvector to be taken for each pair of  $(k_x, k_y)$  momenta, which poses a problem, due to the fact that each of the chosen eigenvectors can have an arbitrary phase. This is not a problem in the continuous case, because the eigenstate of the band is chosen once and then integrated over, making this single phase factor an irrelevant, global phase. In the discrete case, this would lead to distinct, relative phases that can influence the result randomly. A solution to this problem is an adiabatic evolution of the Berry curvature  $\mathcal{F}_n(k_x, k_y)$  as follows [30]

$$\begin{aligned}
C^n &= \frac{1}{2\pi} \int_{\text{BZ}} d^2k \mathcal{F}_n(k_x, k_y), \\
\mathcal{F}_n(k_x, k_y) &= \frac{1}{\delta^2} \text{Im}(\log [U(0 | \delta_y) U(\delta_y | \delta_x + \delta_y) U(\delta_x + \delta_y | \delta_x) U(\delta_x | 0)]) \\
U(\delta_i | \delta_j) &= \langle \phi_n(\mathbf{k} + \delta \mathbf{e}_i) | \phi_n(\mathbf{k} + \delta \mathbf{e}_j) \rangle
\end{aligned} \tag{2}$$

Where  $U(\delta_i | \delta_j)$  takes the role of the discretized Berry potential with  $\delta_i$  being the spacings of the discrete momenta along  $k_i$ , therefore describing a plaquette around each point  $(k_x, k_y)$  in momentum space. This way of connecting the different  $U(\delta_i | \delta_j)$  will get rid of any phase obtained by the eigenvectors, since each phase appears exactly once in a bra and exactly once in a ket, therefore multiplying to unity.

## 1.2 3D Topological Insulators

There are four  $\mathbb{Z}_2$ -indices  $(\nu_0, \boldsymbol{\nu})$  that characterize time-reversal (TR) symmetric 3D TIs with discrete translational invariance [31]. Analogously to the 2D case, systems with the same sum of  $\mathbb{Z}_2$ -indices can be adiabatically transformed to one another and are therefore equivalent [32]. Additionally, one can consider a subsystem of a 3D TI, which describes a 2D system whose Chern number can be evaluated as previously discussed. Since the Chern numbers of these 2D slices are the decisive invariants for us, the four new 3D invariants are not explained in detail. Instead, they have been introduced to justify the categorisation of the 3D TIs.

Depending on the values of the four  $\mathbb{Z}_2$ -indices, one must distinguish between three cases; Trivial systems, weak TIs (WTIs) and strong TIs (STIs). Trivial systems exhibit  $\nu_i = 0$ , WTIs have  $\nu_0 = 0$  and  $\boldsymbol{\nu} \neq 0$ , while STIs require  $\nu_0 \neq 0$  [33]. The difference in 3D TIs can be understood as such: WTIs can be adiabatically transformed to the case of stacked 2D TIs and require more symmetries to be stabilized. For STIs this reduction is not possible. Unlike WTIs, STIs surface states are resilient against perturbations that preserve TR symmetry and cannot close the gap. Thanks to this, STIs host at least one surface with an odd number of Dirac cones, while WTIs can only host an even number [34]. The former is of interest, as this anomalous behaviour cannot be realized in purely 2D systems due to the fermion doubling theorem [35].

To construct a 3D TI one typically begins with a band inverted system, where the type of band inversion can lead to different topological phases [36]. Initially, when the two bands operate independently, they intersect at certain momenta and do not form a gap. Such a system would be considered a conductor as illustrated in Fig. 4. However, the introduction of spin-orbit coupling (SOC) between these bands can now open up a gap. SOC causes the former conduction band to contribute to the former valence band and vice versa, therefore mixing the bands, and creating a new set of conduction and valence bands. This introduces a band gap in the system and the bands can become topologically non-trivial as a result [37]. This process is known as band inversion and is illustrated in Fig. 4.

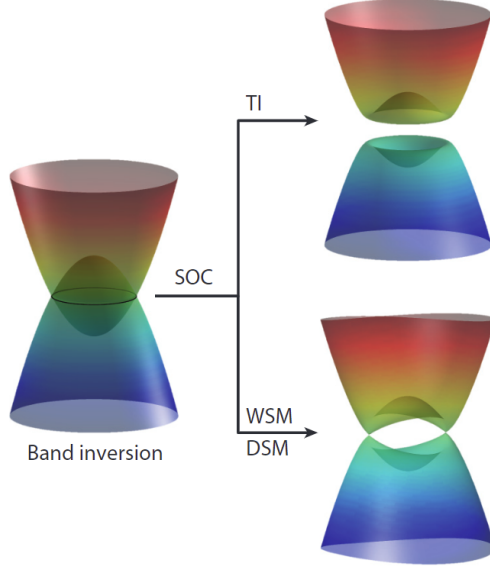


Figure 4: SOC in a band inverted system gaps the system either fully, making it a 3D TI, or everywhere except at linear crossing points, describing WSMs and Dirac semimetals [5].

### 1.3 Weyl Semimetals

As can be seen in Fig. 4, SOC does not necessarily have to gap the bands completely and can allow for linear crossings at critical points, Dirac points, or, if either time-reversal or inversion symmetry has been broken, Weyl points. Both Dirac and Weyl points are closely related to linear band crossings, as one can consider a Dirac node as two overlapping Weyl nodes in momentum space [38]. In the case of a WSM, the Weyl points need therefore to come in pairs of opposite chirality and act as sources and sinks of the Berry potential encountered in Sec. 1.1.1 [5].

It is worth noting that these Weyl points are robust and topologically protected, so long as the considered perturbation is translationally invariant. Consider as an example a Weyl point at momentum  $\mathbf{k} = 0$  that can be written in the form  $\mathbf{k} \cdot \boldsymbol{\sigma}$  [39]. Further, consider a translationally invariant perturbation, which in the vicinity of a Weyl point, written in the form of a Bloch Hamiltonian, yields

$$H(\mathbf{k}) = H_0 \sigma_0 + (k_x - M_1) \sigma_1 + (k_y - M_2) \sigma_2 + (k_z - M_3) \sigma_3. \quad (3)$$

Here,  $H_0$  is the eigenenergy and the  $M_i$  are the perturbations to each coefficient of the Pauli matrices  $\sigma_i$ . As can be seen, such a perturbation simply shifts the Weyl point to a different momentum, namely  $\mathbf{k} = (M_1, M_2, M_3)$ , but can never cause a gap to open.

The WSM differs from 3D TIs by the fact that the bulk spectrum exhibits band touchings, as can be seen on the left of Fig. 5. WSM are therefore not insulators and have a topological invariant of 0 when considering the whole BZ [40]. Due to the role of the Weyl points acting as sources and sinks of Berry potential, contours around the Weyl points yield opposite Chern numbers [41]. Consequently, considering the whole BZ encloses equally many sources and sinks, yielding a Chern number of 0. Still, WSMs are considered topological phases due to the emergence of topological features [42]. In order to observe these features, consider taking slices in the  $k_x k_y$  plane for fixed  $k_z$  momenta, as illustrated by the dashed line on the right of Fig. 5.

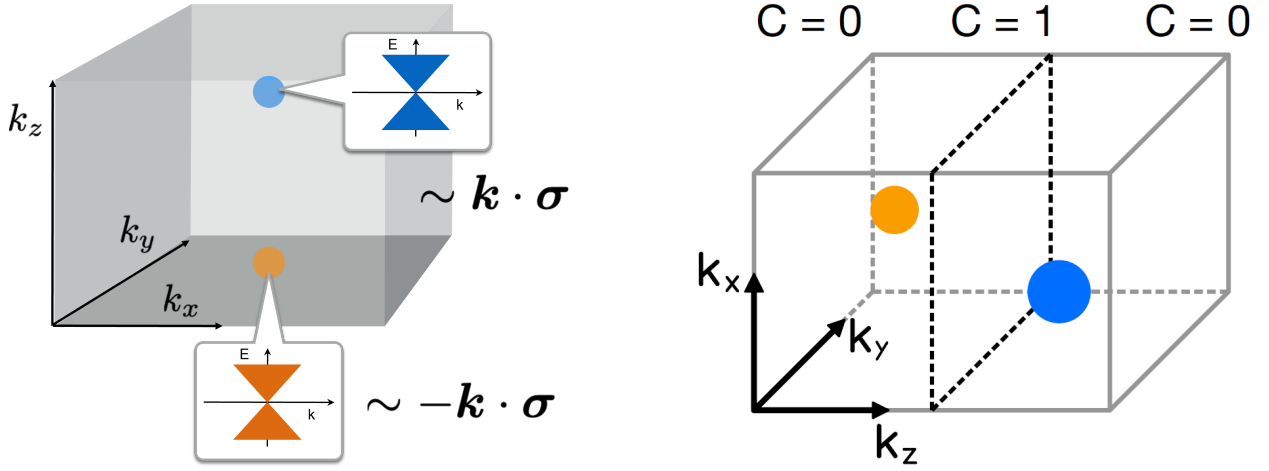


Figure 5: Brillouin zone of a WSM: On the left, two chirally opposite, conical Weyl cones separated in momentum space can be seen and on the right, the Chern number of 2D slices along  $k_z$  are indicated, where slices between the Weyl cones are topologically non-trivial.

As long as no Weyl point lies in the plane, this describes a 2D gapped system. Moreover, considering slices between two Weyl points describes a Chern insulator for each  $k_z$  momentum, as covered in Sec. 1.1, that will exhibit chiral, conducting edge states for OBC [43]. This is further explained in Sec. 1.3.1.

The WSM used in this thesis is a two sublattice model exhibiting time-reversal symmetry and breaking inversion symmetry in order to separate the Weyl cones in momentum space. Otherwise, the Weyl cones overlap in  $k$ -space and form a Dirac cone [44]. Time-reversal symmetry requires each Weyl point at some momentum  $\mathbf{k}_{\text{Weyl}}$  to be mapped to the opposite momentum  $-\mathbf{k}_{\text{Weyl}}$ , while preserving the chirality [1]. This effectively doubles the number of Weyl points for each split Dirac cone, in this case yielding four, as can be seen in Fig. 6.

$$\mathbf{k}_{\text{Weyl},1,2} = (0, \pm\pi/2, \pi)$$

$$\mathbf{k}_{\text{Weyl},3,4} = (\pi, \pm\pi/2, \pi)$$

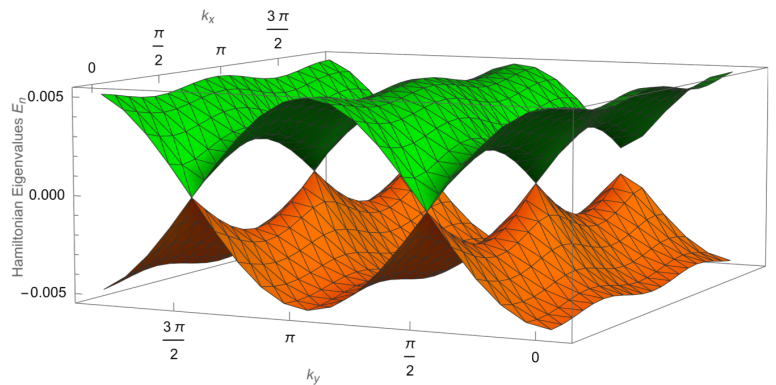


Figure 6: Bandstructure of the modelled WSM at  $\mathbf{k}_z = \pi$  with the four band touching Weyl points.

The bandstructure in Fig. 6 is given by the Hamiltonian

$$\begin{aligned} H(\mathbf{k}) = & - [(C_{Az} - \alpha) \cos(k_y)] \sigma_0 \\ & - [C_1 (1 + \cos(k_z)) + 2C_y \cos(k_y - k_x)] \sigma_x \\ & - [C_1 \sin(k_z)] \sigma_y - [(C_{Az} + \alpha) \cos(k_y)] \sigma_z, \end{aligned} \quad (4)$$

where  $C_i$  and  $\alpha$  are parameters that will be introduced later, as they do not influence the position

of the Weyl nodes in momentum space.

The Chern numbers can then be calculated according to Eq. (2) for different  $k_x$  momenta, where the 2D system is then integrated over the  $k_y, k_z$  momenta, as shown in Fig. 7.

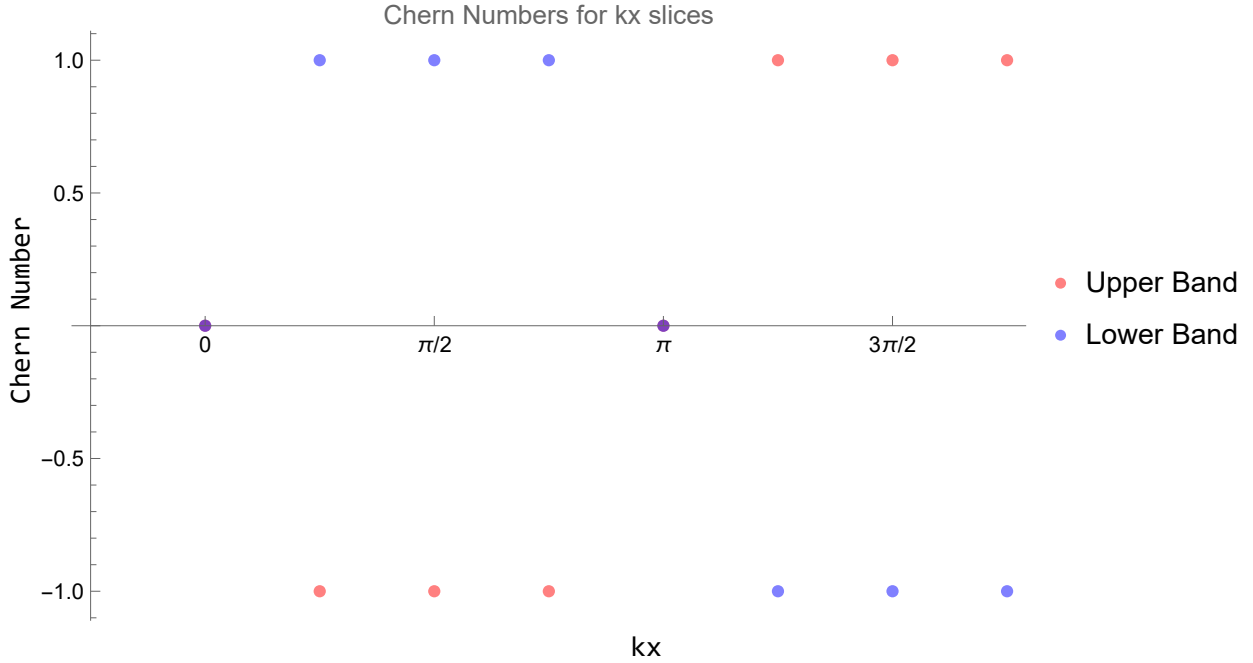


Figure 7: Chern numbers of the two bands for different  $k_x$  momenta.

As can be seen, traversing the BZ closes the gap, which allows for the value of the Chern number to change, consistent with the discussion above. Also important to note is the fact that the Chern numbers of the two bands are always opposite to each other, as the system as a whole has to be trivial and therefore has to add up to 0.

Lastly, while Fig. 6 shows the Weyl cones nicely, it is limited by the fact that one of the momenta needs to be fixed. Therefore, the bandstructure is presented as the eigenvalues along the high symmetry path shown in red in Fig. 8.

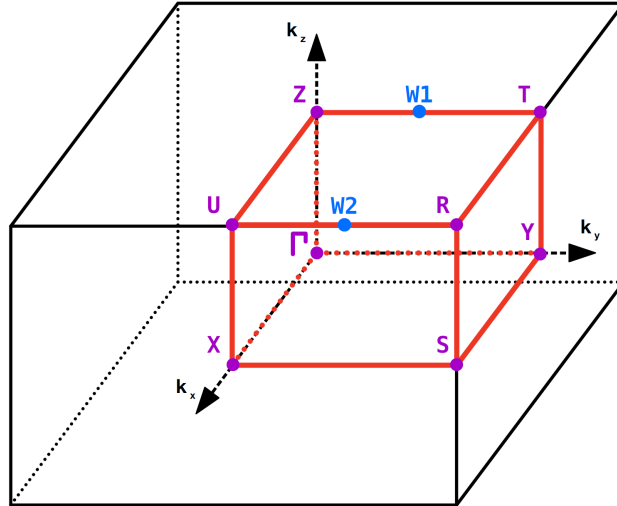


Figure 8: BZ of the WSM used in this thesis with two of the four Weyl points marked in blue, as well as the high symmetry points inside the BZ in violet and the path along BZ that is traced in red. The starting point is  $\Gamma$  and goes counter clockwise, continues to Z upon returning, where another counter clockwise round is traced. This yields the path  $\Gamma$ -X-S-Y- $\Gamma$ -Z-U-R-T

Tracing such a path now yields a 2D plot instead still showing the most important features of the bandstructure, such as the Weyl points. The high symmetry path bandstructure for the studied WSM model is shown in Fig. 9.

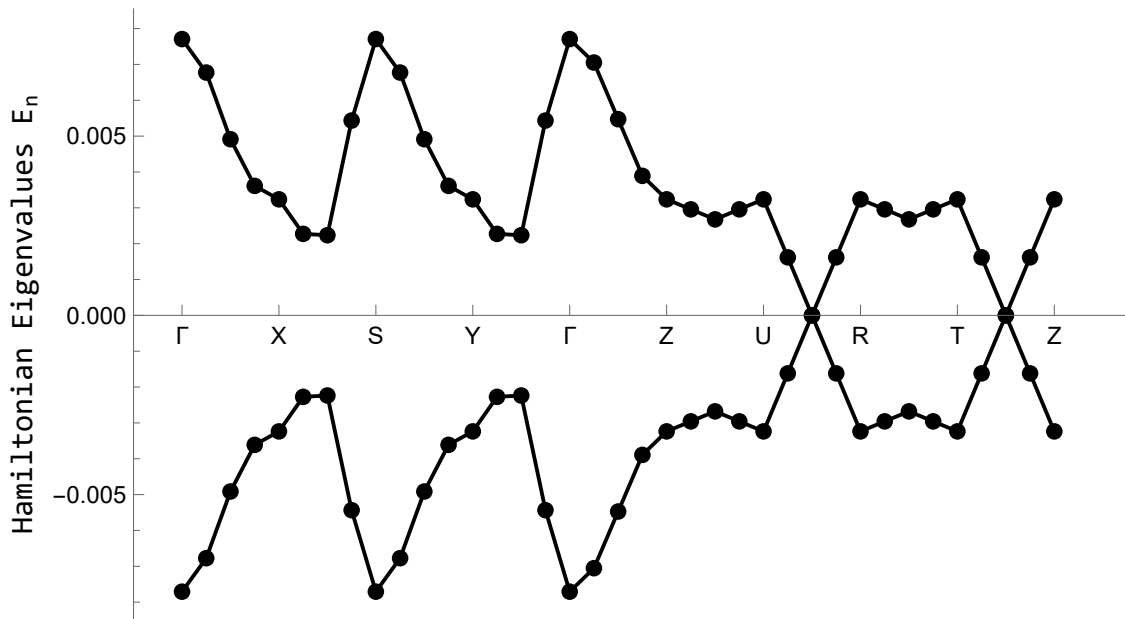


Figure 9: Theoretical WSM bandstructure for periodic boundary conditions (PBC) along the high symmetry path shown in Fig. 8. The black dots correspond to the momenta at which the Hamiltonian's energy was evaluated. The step-size is  $2\pi/8$  in order to reflect the resolution of the system of study.

Since the theoretical values are ideal, they will most likely never perfectly agree with experimental observations. For this reason, the theoretical bandstructure will be scaled to be comparable to the measured bandstructures, since the important feature is the shape of the bandstructure.

### 1.3.1 Fermi Arc

The fact that the volume between two Weyl points in momentum space consists of 2D slices of Chern insulators has an interesting consequence for the WSM bandstructure for OBC along one direction, e.g. the  $z$ -direction. Due to the termination of the crystal,  $k_z$  is not a good quantum number near the edges and the result are surface Brillouin zones (SBZs), which are characterized by the  $z$ -components of the boundaries in real space and  $k_x, k_y$  components in momentum space. The chiral edge states of the Chern slices are localized at these SBZs, where only one chirality is found per surface. These chiral edge states give rise to the so called Fermi arcs illustrated in Fig. 10, which connect two Weyl points of opposite chirality in the SBZ [5].

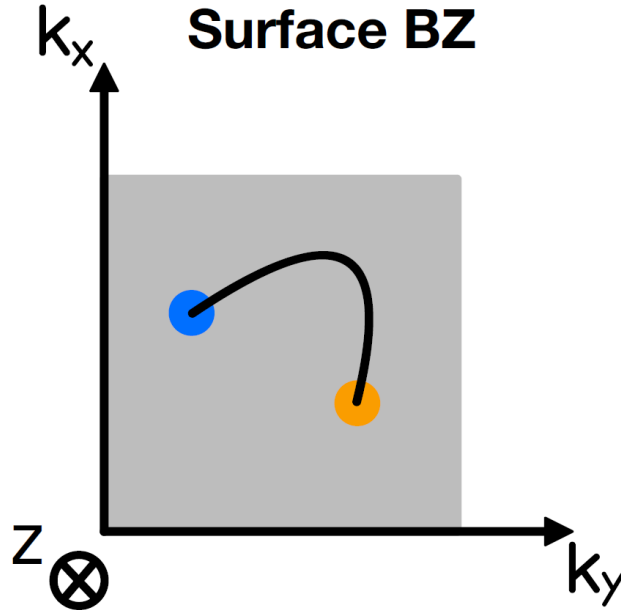


Figure 10: Illustration of a SBZ zone of a WSM with two Weyl points colored in blue and orange, as well as the Fermi arc connecting them.

This anomalous Fermi arc forms an open Fermi surface contour at the boundaries, which is not possible in purely 2D systems, as they require closed contours [10]. Due to the fact that spectral flow into the bulk is possible at the Weyl points, both surfaces, and thus both Fermi arcs, are connected via the bulk, hence when overlapping both SBZs, the closed contour is restored [45].

Since the used WSM model exhibits four Weyl points, therefore creating two sources and sinks of Berry curvature, two Fermi arcs emerge. As the Fermi arcs are the most important features, a similar high symmetry path is traced in the SBZ in order to present the OBC bandstructure in a clear way. There are now only two momenta left, making the traced path as easy as starting at  $(0,0)$  and going to each Weyl point in the following order:  $(0, \pi/2)$ , then to  $(\pi, \pi/2)$ ,  $(\pi, 3\pi/2)$ ,  $(2\pi, 3\pi/2)$  and finally back to  $(2\pi, 2\pi)$ . The bandstructure of the WSM for OBC along this path is shown in Fig. 11.

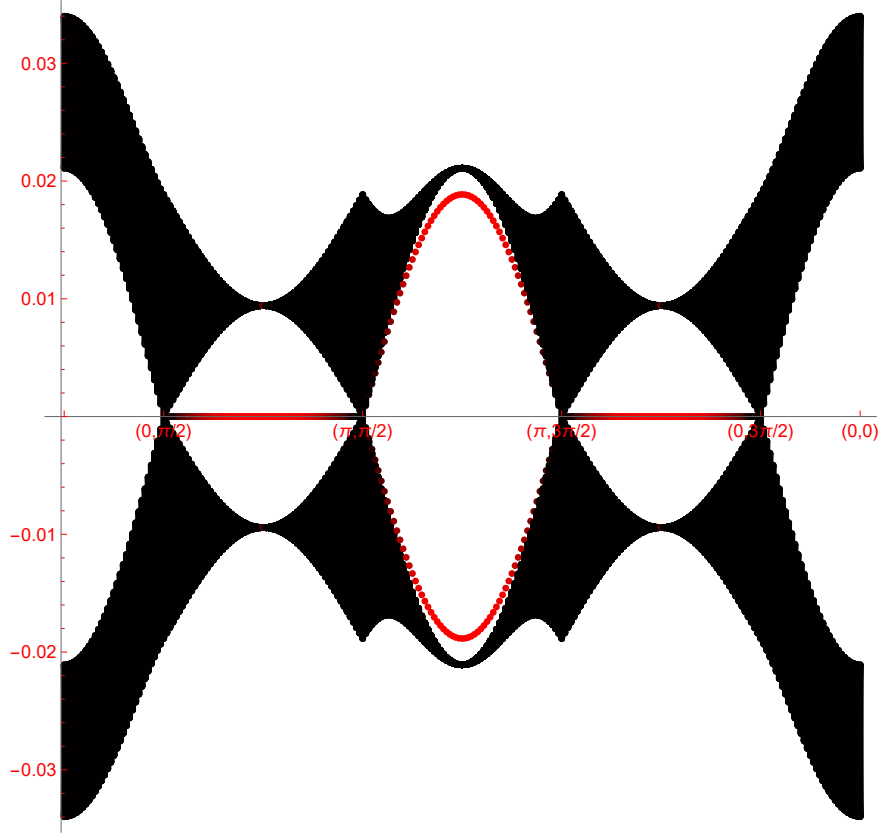


Figure 11: Dispersion relation of a WSM for OBC with the inverse participation ratio (IPR) localization of the eigenvalues indicated by the red hue. IPR is a measure of how localized the eigenvalue corresponding to an eigenstate is (see Eq. (5)).

The IPR of each eigenvalue shown in Fig. 11 indicates the surface localization of the Fermi arcs [46]. The IPR formula is given by

$$\text{IPR} = \frac{\sum_i |\psi_i|^4}{\sum_i |\psi_i|^2}, \quad (5)$$

where  $\psi_i$  is the normalized wavefunction of the site  $i$ . Further, the Fermi arcs for the two surfaces are localized on the two different sublattices of the two band tight-binding model, as can be seen in Fig. 12.

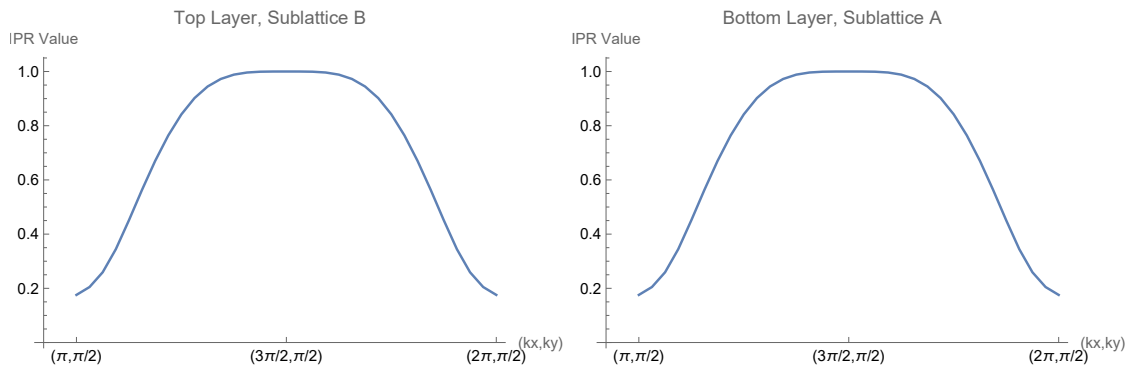


Figure 12: IPR localization of the Fermi arcs on the two surfaces. Two Fermi arcs on the same surface are localized on the same sublattice.

Lastly, the Fermi arcs seen in Fig. 11 show that the dispersion as a function of  $k_x$  is flat, however, this is not the case for  $k_y$ , as can be seen in Fig. 13.

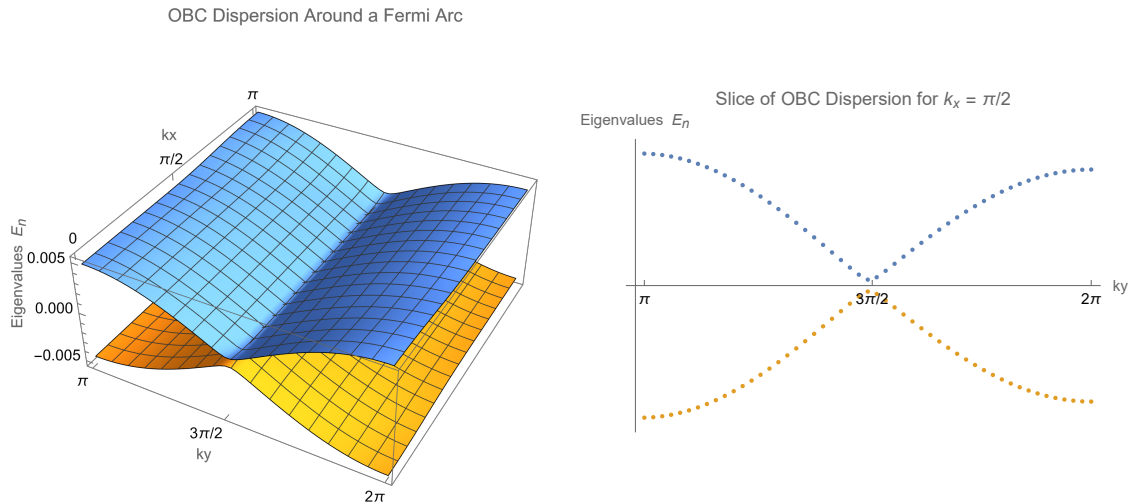


Figure 13: Theoretical dispersion of top and bottom layers of the WSM around the  $(\pi/2, 3\pi/2)$  Weyl point for OBC on the left and a slice for  $k_x = \pi/2$  of the bandstructure on the right.

As can be seen, the dispersion in the vicinity of a Fermi arc is, as already observed, independent of  $k_x$ , but linear in  $k_y$ . Therefore, the Fermi arc's dispersions are of the form

$$E_{FA}(k_x, k_y) \sim \pm v_{FA} \cdot k_y, \quad (6)$$

where  $v_{FA}$  is the velocity of the Weyl quasiparticles, resembling the expected dispersion seen in Fig. 3. The sign depends on the Chern number, hence, the dispersions of the two Fermi arcs with opposite chirality present per surface will vary by a sign.

As a consequence, injecting a wavepacket with momentum  $k_x = \pi/2$  should only be possible at the surfaces and for one sublattice. Further, this pulse should propagate monodirectionally along the y-direction, as indicated by Eq. (6).  $k_x = 3\pi/2$  would excite the other Fermi arc, however, due to the opposite Chern number, hence opposite chirality, the direction of propagation has to be opposite to that of the  $k_x = \pi/2$  pulse.

## 2 Non-Hermitian Topology

The Hermiticity of a quantum mechanical Hamiltonian is an important property, as it ensures a complete eigenbasis with real eigenvalues, as well as conservation of energy and probability. In the NH case, these properties not necessarily need to hold, which can arise in open systems, but also in strongly interacting systems with finite quasiparticle life times [47].

The study and description of NH systems can be challenging, as one must proceed more cautiously due to effects like the coalescence of eigenvectors at exceptional points, making the Hamiltonian defective, or the NH skin-effect [14]. Additionally, the concept of an energy gap needs to be adjusted, as the energy eigenvalues can be complex.

The upcoming Secs. aim to extend the concept of energy gaps and topological invariants in NH phases, categorize the emerging structures, introduce exceptional points and the NH skin-effect, in order to understand the role of the exceptional topological insulator (ETI), which is the ultimate object of interest.

### 2.1 Non-Hermitian Energy Gaps

Since the energy is now in general complex valued, the energies are projected on to the complex plane, consisting of real and imaginary part of the energy as seen in Fig. 14. The concept of an energy gap needs to be adapted, since one has to consider what structures can be formed for a complex valued energy spectrum. This establishes a non-Hermitian extension of an insulating gap.

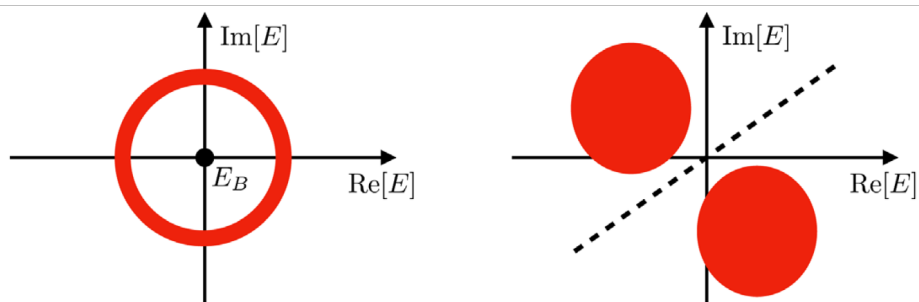


Figure 14: Projection of all the energy eigenvalues (red regions) on to the complex energy plane forming a point gap (left) and a line gap (right) [14].  $E_B$  represents an arbitrary energy inside the point gap.

One then differentiates between two energy gaps; a line gap, where one can always continuously deform the energies to return to the Hermitian or anti-Hermitian case, which is a separation of the energies at zero energy in the real or imaginary energy line. The other is a point gap, where this separation is not possible [48]. The line gap is therefore a generalization of the Hermitian gap, while the point gap is an intrinsically non-Hermitian effect [49].

A critical Hermitian bandstructure, like a WSM, is a suitable basis in order to achieve a point gap, which can be done by giving the Weyl cones different life times and hence different complex energies [5]. As mentioned in the Sec. 1.3.1, the projection of both Fermi arcs yields a closed contour, which stays intact even when the Weyl points acquire finite life times. Thus, by construction, the Fermi arc guarantees a point gap when proceeding to the NH case, as will be seen in Sec. 2.5.

## 2.2 Exceptional Points

Exceptional points (EPs) are band touching points in non-Hermitian systems, meaning that real and imaginary part coincide, which also have two or more coalescing eigenvectors. This distinguishes EPs from Hermitian band degeneracies, as the Hamiltonian becomes defective. EPs, specifically of second order, arise due to square-root singularities of a parameter in a Hamiltonian's eigenvalues and reduce to a 2D problem in the vicinity of such EPs [50]. Due to the complex valued behaviour of the square root function, for a two band model, the energy values form a two-sheeted Riemann surface, as shown in Fig. 15. One of the consequences is that tracing a path around an EP, illustrated by the purple path in Fig. 15, will not yield the initial eigenvector and eigenvalue, but rather the eigenvector and eigenvalue of the other band. Hence, to return to the initial case, an EP has to be encircled twice [14].

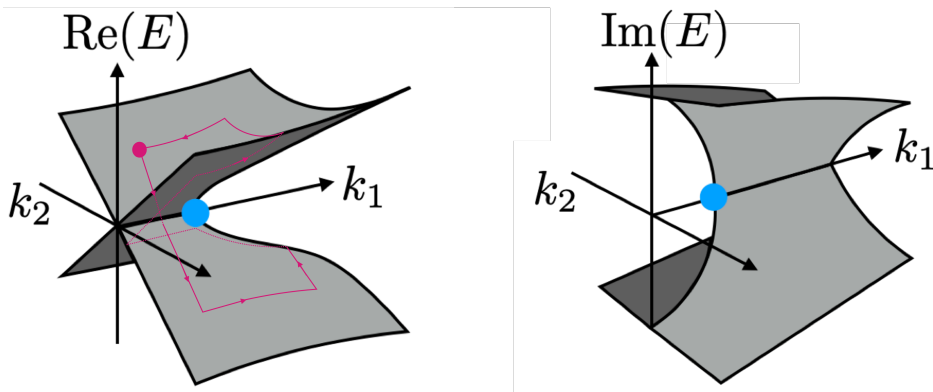


Figure 15: Real and imaginary part of the two-sheeted Riemann surface of two complex valued bands, with the EP marked in blue and the path encircling the EP in purple [51].

Similar to Dirac points in 2D, EPs are subject to the fermion doubling theorem and therefore can only come in pairs [52]. This can be directly seen in Fig. 15, since the edges of both real and imaginary bands in the  $k_1$  direction cannot be associated with each other, respectively, hence requiring a copy of the bands to achieve periodicity.

## 2.3 Complex Vortices

Another way band touching can occur are complex vortices. These vortices can be obtained from a two band model whose Bloch Hamiltonian coefficient can be complex valued, which has a generic form of

$$H(\mathbf{k}) = \mathbf{d}(\mathbf{k})\sigma + d_0(\mathbf{k})\sigma_0, \quad (7)$$

with  $\mathbf{d} = \mathbf{d}_R + i\mathbf{d}_I \in \mathbb{C}^3$ ,  $d_0 \in \mathbb{C}$  and  $\sigma_i$  the Pauli matrices with  $\sigma_0$  the  $2 \times 2$  identity. From the energy spectrum, after omitting the  $\mathbf{k}$  dependency,

$$E_{\pm} = d_0 \pm \sqrt{d_R^2 - d_I^2 + 2i\mathbf{d}_R \cdot \mathbf{d}_I}, \quad (8)$$

it is clear that only two condition have to be met in order to allow for band touching, namely

$$d_R^2 = d_I^2, \quad \mathbf{d}_R \cdot \mathbf{d}_I = 0. \quad (9)$$

Since only two real conditions are required, which are dependent on  $\mathbf{k}$ , these band touchings are already stable and topologically protected in 2D [53]. Furthermore, non-trivial solutions of the conditions in Eq. (9) inevitably lead to EPs as described above, while the case  $\mathbf{d}_R = \mathbf{d}_I = 0$  does not and instead can yield conical band touchings. These conical band touchings require further

adjustment of the Hamiltonian's parameters in order to appear [14]. In 2D, near these conical touching points, complex vortices of the form

$$E(\mathbf{k}) = k_x + ik_y, \quad (10)$$

which come in pairs of vortex and anti-vortex, are of interest.

Lastly, it is worth noting that EPs and complex vortices do not describe different topological phases, since they can be continuously transformed into each other without closing the bulk pointgap. Instead, one can switch between the two cases without having to change the phase, as will be seen in Sec. 2.5, where these band touchings manifest as surface states.

## 2.4 Non-Hermitian Skin Effect

The Hermiticity of a periodic system guarantees that the hopping matrix elements to the neighbors in a periodic system are equal. This is not necessarily the case in NH systems, which can give rise to the NH skin effect as illustrated in Fig. 16. The asymmetry of hopping probabilities for PBCs is not problematic, as the periodicity prohibits any sort of accumulation of probability at a site. However, this is not the case for OBCs, where the particle is exponentially localized towards the edge of increased hopping probability [54].

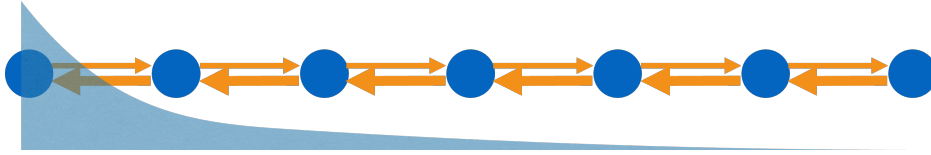


Figure 16: Illustration of asymmetric hopping probabilities (orange arrows) between sites of a 1D chain (blue circles) and the exponential localization of the particle at one end indicated by the blue curve.

Thus, the spectrum of a NH system can vastly differ depending on the boundary conditions, which poses a difficulty in the topological description of systems. As mentioned in Sec. 1, the bulk spectrum and its topology determine the behaviour of the edges for OBC. Due to the NH skin effect, the bulk-boundary correspondence cannot always be made for point-gapped systems, as can be seen in Fig. 17, because the point gap can collapse for OBC. However, it is possible to evade this problem by considering semi-infinite systems, as will be relevant later on [55].

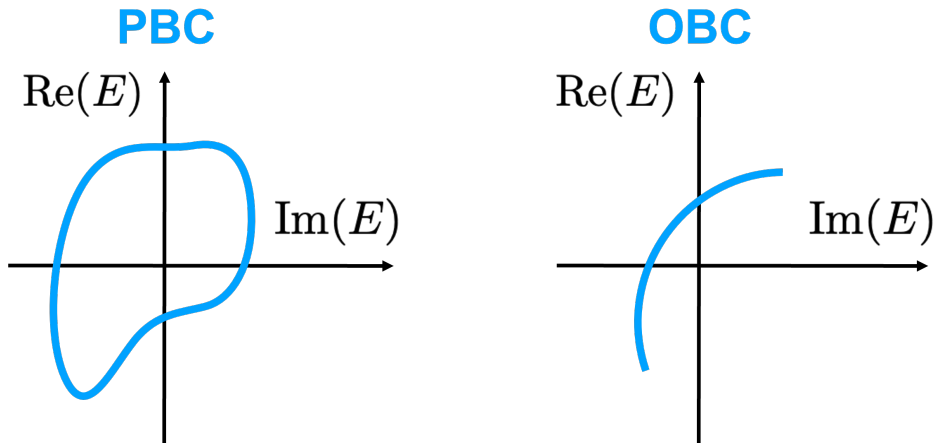


Figure 17: Illustration of the collapse of the point gap spectrum when changing from PBC to OBC as a consequence of the NH skin effect [51].

### 2.4.1 1D Winding Number

The presence of the NH skin effect for OBC is indicated by a non-zero 1D winding number of the point gap, as shown in Eq. (11) for the 1D case [56]. The 1D winding number counts a rather simple quantity: For an energy  $E_B$  inside the point gap, which can be the zero energy, it determines the times the complex energy values of  $H(k)$  encircle  $E_B$  as  $k$  goes from  $-\pi$  to  $\pi$ . The winding number can only be non-zero in NH systems and vanishes in the Hermitian case [57].

$$w_{1D} = \int_{\text{BZ}} \frac{dk}{2\pi i} \partial_k \ln \det [H(k) - E_B] \quad (11)$$

This winding number can be extended to odd, higher dimensions, as will be introduced in Sec. 2.5 for the 3D case [58].

## 2.5 Exceptional Topological Insulator

This Sec. covers the theoretical considerations of an exceptional topological insulator (ETI) based on the findings of Denner *et al.*[13]. It justifies and unites the themes which have been presented so far and is the actual system of interest.

The ETI can be seen as the NH extension of a 3D TI, as it exhibits anomalous surface states that are not possible in purely 2D NH systems. It can be constructed from a WSM by associating different life times to the Weyl points, guaranteeing an energy point gap, and the now complex eigenvalues of the Fermi arc form the surface states. The anomalous surface objects of study in this case are the EPs and vortices encountered in Sec. 2.2 and 2.3, which will cover the point gap. Occurrence of these objects at the surfaces are not overshadowed by the spectrum collapse for OBC in one direction due to the NH skin effect.

To see the emergence of the ETI from a WSM, consider the tight-binding, cubic, spinfull 3D TI model with s and p orbitals at each site given by

$$H(\mathbf{k}) = \left( \sum_{j=x,y,z} \cos k_j - M \right) \tau_z \sigma_0 + \sum_{j=x,y,z} \sin k_j \tau_x \sigma_j, \quad (12)$$

where the Pauli matrices  $\sigma_i$  act on the spin and the  $\tau_i$  act on the orbitals, and  $M$  is the mass term that controls the transition between a trivial 3D TI and a non-trivial one, which is the case for  $1 < |M| < 3$ . At exactly  $M \in \{1, 3\}$  the system becomes a Dirac semimetal. In the low energy regime near the Dirac points one gets for  $M = 3$  a Hamiltonian of the form

$$\tau_x (\mathbf{k} \cdot \boldsymbol{\sigma}) = \begin{pmatrix} 0 & \mathbf{k} \cdot \boldsymbol{\sigma} \\ \mathbf{k} \cdot \boldsymbol{\sigma} & 0 \end{pmatrix}, \quad (13)$$

with eigenvalues

$$E_{W1} = \pm |\mathbf{k}|, \quad E_{W2} = \pm |\mathbf{k}|, \quad (14)$$

which shows the dispersions of the two overlapping Weyl cones in momentum space. This system is both time-reversal and inversion ( $\mathcal{I}$ ) symmetric, consistent with the findings from Sec. 1.3.  $\mathcal{T}$  is given by  $\tau_0 \sigma_y$  which leaves the Hamiltonian invariant as

$$\mathcal{T} H(\mathbf{k}) \mathcal{T}^{-1} = H(\mathbf{k}), \quad (15)$$

while  $\mathcal{I}$  is given by  $\tau_z \sigma_0$  leaving the Hamiltonian invariant as

$$\mathcal{I} H(\mathbf{k}) \mathcal{I}^{-1} = H(\mathbf{k}). \quad (16)$$

To achieve a WSM,  $\mathcal{T}$  can be broken using a magnetic field term of the form

$$\tau_0 (\mathbf{B} \cdot \boldsymbol{\sigma}) \quad (17)$$

which yields the low energy Hamiltonian

$$H_{\text{eff}} = \tau_x (\mathbf{k} \cdot \boldsymbol{\sigma}) + \tau_0 (\mathbf{B} \cdot \boldsymbol{\sigma}) = \begin{pmatrix} 0 & \mathbf{k} \cdot \boldsymbol{\sigma} \\ \mathbf{k} \cdot \boldsymbol{\sigma} & 0 \end{pmatrix} + \begin{pmatrix} \mathbf{B} \cdot \boldsymbol{\sigma} & 0 \\ 0 & \mathbf{B} \cdot \boldsymbol{\sigma} \end{pmatrix}. \quad (18)$$

The energy eigenvalues of this Hamiltonian are now given by

$$E_{W1} = \pm |\mathbf{k} + \mathbf{B}|, \quad E_{W2} = \pm |\mathbf{k} - \mathbf{B}|, \quad (19)$$

which describes two Weyl cones separated by the vector  $2\mathbf{B}$  in momentum space. Lastly, the NH term is added to achieve a separation in the complex plane, given by

$$\tau_x (i\delta\sigma_0). \quad (20)$$

This describes the Hamiltonian

$$H_{\text{eff}}^{\text{nh}} = \tau_x (\mathbf{k} \cdot \boldsymbol{\sigma}) + \tau_0 (\mathbf{B} \cdot \boldsymbol{\sigma}) + \tau_x (i\delta\sigma_0) = \begin{pmatrix} \mathbf{B} \cdot \boldsymbol{\sigma} & \mathbf{k} \cdot \boldsymbol{\sigma} \\ \mathbf{k} \cdot \boldsymbol{\sigma} & \mathbf{B} \cdot \boldsymbol{\sigma} \end{pmatrix} + \begin{pmatrix} 0 & i\delta\sigma_0 \\ i\delta\sigma_0 & 0 \end{pmatrix}, \quad (21)$$

with the eigenvalues

$$E_{W1} = +i\delta \pm |\mathbf{k} + \mathbf{B}|, \quad E_{W2} = -i\delta \pm |\mathbf{k} - \mathbf{B}|. \quad (22)$$

As a whole, the Hamiltonian is given by

$$H(\mathbf{k}) = \left( \sum_{j=x,y,z} \cos k_j - M \right) \tau_z \sigma_0 + \lambda \sum_{j=x,y,z} \sin k_j \tau_x \sigma_j \quad (23)$$

$$+ [\sin \alpha \tau_0 + \cos \alpha \tau_z] (\mathbf{B} \cdot \boldsymbol{\sigma}) + i\delta \tau_x \sigma_0.$$

This way, a WSM inevitably will yield a point gap as shown in the middle of Fig. 18.

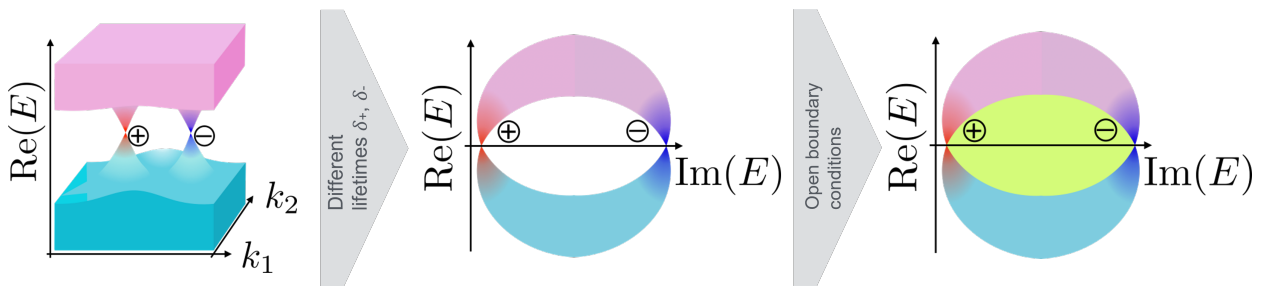


Figure 18: Illustration of the band touching of a WSM (left) whose Weyl points acquire different lifetimes and are therefore separated on the imaginary axis to form a point gap (middle), which is then covered by the Fermi arc eigenvalues for OBC indicated in green (right) [13].

The Hermitian WSM exhibited a Chern insulator for each slice in momentum space between the Weyl points, which then yielded the Fermi arc for OBC in the  $z$ -direction. The continuation of the Hermitian to the NH WSM leads to the same continuation of the Hermitian Chern insulator to the NH Chern insulator. The surface spectrum of the ETI for OBC in the  $z$ -direction is then the aforementioned single vortex that covers the point gap as a sheet of eigenvalues of the form  $k_x + ik_y$ , as can be seen on the left of Fig. 19, which is the NH equivalent of the Fermi arc. The

existence of a vortex on a surface without the anti-vortex is an anomalous NH surface state.

By changing the magnetic field term of Eq. (17) to  $\tau_z (\mathbf{B} \cdot \boldsymbol{\sigma})$ , an EP emerges inside the point gap. A single EP is anomalous and as well a unique feature of the NH 3D TI. Still, every energy value inside the point gap is covered, just like the single vortex, but the dispersion changes.

This shows that EPs and complex vortices are not two topologically distinct phases, as one can interpolate between the two cases without closing the point gap. The difference in their dispersions can be seen in Fig. 19.

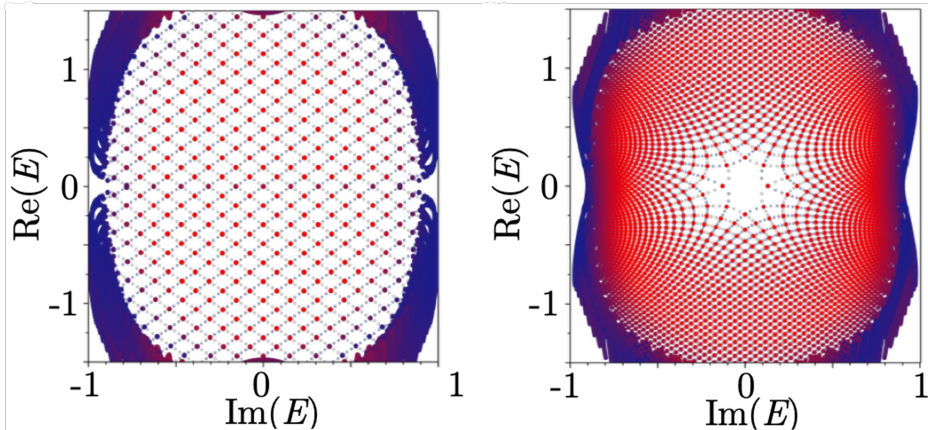


Figure 19: Complex vortex eigenvalues covering the point gap (left) vs. EP eigenvalues covering the point gap (right). Both cases cover the point gap completely and the difference is only visible due to the discreteness of the points in momentum space. The eightfold pattern on the right arises due to the fact that eight turns have to be made around the EP to return to the starting point, as seen in Fig. 15, while the left pattern only requires four [13].

### 2.5.1 ETI Winding Numbers

The ETI is characterized by a non-zero winding number given by

$$w_{3D} = - \int_{\text{BZ}} \frac{d^3 \mathbf{k}}{24\pi^2} \epsilon_{ijk} \text{Tr} [Q_i(\mathbf{k}) Q_j(\mathbf{k}) Q_k(\mathbf{k})], \quad (24)$$

$$Q_l(\mathbf{k}) = [H(\mathbf{k}) - E]^{-1} \partial_{k_l} [H(\mathbf{k}) - E],$$

where  $H(\mathbf{k})$  is the system's Hamiltonian,  $E$  is any arbitrary energy inside the point gap and  $\epsilon_{ijk}$  is the Levi-Civita symbol. The significance of  $w_{3D}$  can be seen by considering slices of the surface BZ as indicated in Fig. 20.

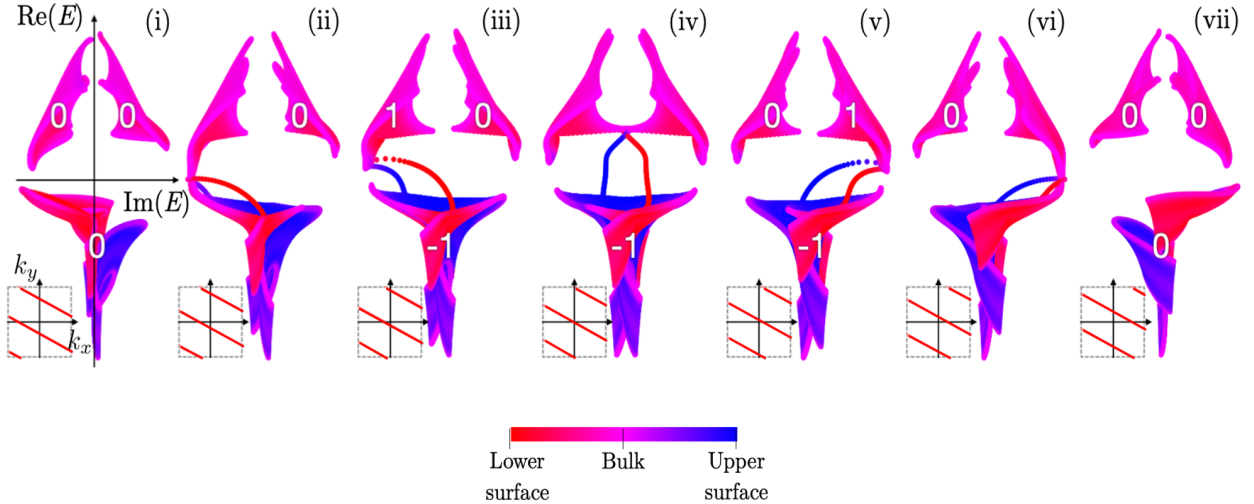


Figure 20: Energy eigenvalues for different slices of the BZ, as indicated on the bottom left of each picture. The surface localization is indicated by the color of the eigenvalues and the Chern number of the different regions, if defined, is written in white. Moving from left to right shows the evolution of the energy eigenvalues and the change in Chern numbers as the whole BZ is traversed [13].

For the system described by Eq. (23) the energies are split into 3 regions to which a Chern number can be assigned. Starting off at (i), the regions are trivial and gapped from each other. (ii) shows two of the bands connecting and exchanging Chern numbers by closing the gap, hence the Chern number is not defined, with strong surface localized energies reaching the other band, shown as the red and blue arcs. In (iii) the bands gap again with different Chern numbers, but still adding up to zero, and are connected by the surface states. This is then continued until all the slices covered the whole BZ as shown in (vii). Thus, traversing the BZ this way has pumped one quantum of Berry flux, as indicated by a +1 Chern number, in the clock-wise direction and would therefore yield a  $w_{3D} = 1$ . Hence,  $w_{3D}$  counts the quanta of Berry flux that circle around the point gap, which is known as chiral charge pumping.

Notice that the surface spectrum is the projection of all the slices, which will recover the point gap, but will also inevitably result in a covering of the point gap by the surface states.

Additionally, the weak 1D winding number, which is similar to the  $w_{1D}$  seen in Eq. (11) encountered in Sec. 2.4.1, can be calculated as follows

$$w_{1D,i} = - \int_{\text{BZ}} \frac{d^3 \mathbf{k}}{(2\pi)^3} \text{Tr} [Q_i(\mathbf{k})]. \quad (25)$$

The index  $i$  describes the axis direction, such that  $w_{1D,i}$  indicates whether the system exhibits the NH skin effect for OBC along the direction  $i \in x, y, z$ . In this case, the ETI has  $w_{1D,i} = 0$ , which is why the OBC spectrum can be observed without the collapse due to the NH skin effect. However, a higher order variant of the NH skin effect still occurs for OBC in two directions.

### 3 Topoelectrical Circuits

An ETI can be realized in metamaterials, for instance in an electric circuit consisting of resistors, inductances and capacitors (RLC) components, whose behaviour is described by its circuit Laplacian. The idea of metamaterials is to make a correspondence between the description of the meta-system, in this case the circuit Laplacian, and the Hamiltonian of a quantum mechanical system. Circuits in particular offer an accessible platform to model phases of matter which can be hard to realize in actual materials [59]. However, the limitations of such metamaterials are quantum mechanical effects such as fermion exclusion interactions or TR symmetry with  $\mathcal{T}^2 = -1$  and the associated Kramer pairs [60]. Thus, the model in consideration is that of a single electron system.

Due to the fact that RLC circuits are intrinsically dissipative systems, they are good candidates to host NH phases of matter. However, they are not limited to loss of energy via resistors, but can also model gain of energy via active components such as amplifiers. Additionally, it is quite easy to measure voltages and currents at nodes, change between PBC and OBC using connectors, as well as to study phenomena which are localized at the boundaries of the circuit.

The next Secs. introduce the circuit Laplacian formalism, which will be illustrated with an example, before the more complicated ETI configurations are presented. Further, the objects of interest for the WSM circuit model, such as the bandstructure and surface spectral functions are shown, and lastly the simulations that are relevant for this project and how they are generated will be discussed.

#### 3.1 Circuit Laplacian

Kirchhoff's law describes the interplay of currents  $I_i$  and voltages  $V_i$  of nodes that are connected by circuit components as

$$I_i(\omega) = \sum_{j \neq i} J_{ij}(\omega) V_j(\omega), \quad (26)$$

where  $J_{ij}$  describes the components connecting the node  $i$  with the node  $j$ . The entries follow the current-voltage relations of RLC components known from electrodynamics, shown in Tab. 3.

Table 3: Current and voltage relations in the time (left) and frequency (center) domain, as well as the corresponding terms of the matrix elements of the circuit Laplacian.

| Time domain                  | Frequency domain         | Term in $J_{ij}$ |
|------------------------------|--------------------------|------------------|
| $V = R \times I$             | $V = R \times I$         | $1/R$            |
| $I = C \times \frac{dV}{dt}$ | $I = i\omega C \times V$ | $i\omega C$      |
| $V = L \times \frac{dI}{dt}$ | $V = i\omega L \times I$ | $1/(i\omega L)$  |

The form in Eq. (26) already suggests that  $J_{ij}$  are elements of a matrix, which is called the circuit Laplacian  $J$ . Hence, the Laplacian describes the relation of voltages and currents of a system as

$$\mathbf{I} = J\mathbf{V}. \quad (27)$$

The Laplacian can be written as the sum of three matrices; the total node conductance  $D$  which is a diagonal matrix denoting all the conductances from each node, the adjacency matrix  $C$  which

is an off-diagonal matrix describing how the nodes are interconnected and the circuit ground  $W$  which is a diagonal matrix describing how the nodes are connected to the circuit ground [59]. The Laplacian is then

$$J = D - C + W. \quad (28)$$

### 3.1.1 Example

A visualization of such a Laplacian can be seen in Fig. 21, which describes a three node system.

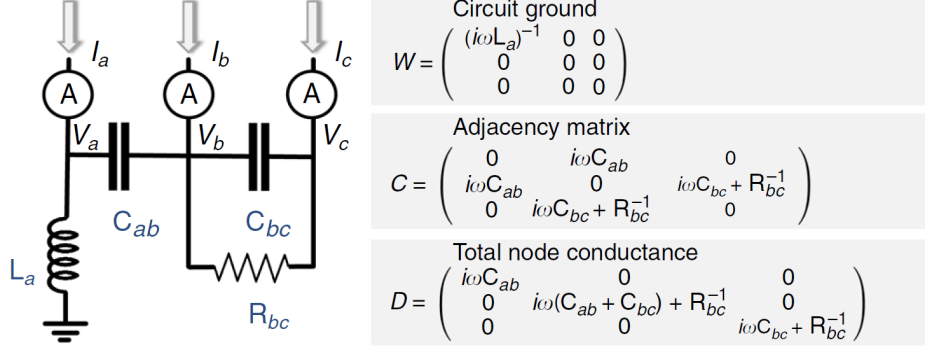


Figure 21: A small example of an RLC circuit where the  $D, C$  and  $W$  matrices describe the component relations at each of the three nodes (intersections) and can be used to create the Laplacian  $J = D - C + W$  [59].

### 3.1.2 Laplacian Reconstruction

In an experiment, the currents and voltages are the measured quantities and used to reconstruct the Laplacian. For a two sublattice,  $8 \times 8 \times 8$  system, this would require  $1024 \times 1024$  measurements, namely a measurement of the whole board for each of the 1024 nodes one can feed in a current. The translational invariance reduces this to  $2 \times 1024$  (PBC) or  $16 \times 1024$  (OBC) measurements, because translating the current input by one lattice vector will yield the same result. Only the two different sublattices will yield different results, while for OBC in the  $z$ -direction, the layers are not equivalent anymore, thus each layer requires two current inputs.

To determine the Laplacian, the current and voltage vectors are reordered to  $2048 \times 2048$  matrices with 4 blocks of  $1024 \times 1024$  entries

$$J = \mathbf{I}\mathbf{V}^{-1} = \begin{bmatrix} \left( \begin{array}{c} \text{Input Sublattice A} \\ \text{Nodes in Sublattice A} \end{array} \right) & \left( \begin{array}{c} \text{Input Sublattice A} \\ \text{Nodes in Sublattice B} \end{array} \right) \\ \left( \begin{array}{c} \text{Input Sublattice B} \\ \text{Nodes in Sublattice A} \end{array} \right) & \left( \begin{array}{c} \text{Input Sublattice B} \\ \text{Nodes in Sublattice B} \end{array} \right) \end{bmatrix}. \quad (29)$$

The blocks are ordered by the sublattice the current is put in, vertically, and by the sublattice the measured currents/voltages belong to, horizontally. Since there is only one current input at a time, the current matrix will only have diagonal entries and all except for 2 or 16 entries, depending on the boundary conditions, will be 0. For the voltage matrix, each block is symmetric by construction and generally not zero. Since each entry is associated with a node whose coordinates are described by  $(x, y, z)$ , the blocks can be Fourier transformed via summation with the appropriate complex weight  $e^{-i\Delta x k_x}$ ,  $e^{-i\Delta y k_y}$ ,  $e^{-i\Delta z k_z}$ , respectively, which yields a  $2 \times 2$  or  $16 \times 16$  matrix as a function of the quasimomenta  $k_x, k_y, k_z$ . For PBC (the OBC case is analogous) this yields the Fourier transformed matrices

$$\tilde{\mathbf{I}}(k_x, k_y, k_z) = \begin{bmatrix} \tilde{\mathbf{I}}_{AA} & 0 \\ 0 & \tilde{\mathbf{I}}_{BB} \end{bmatrix}, \quad \tilde{\mathbf{V}}(k_x, k_y, k_z) = \begin{bmatrix} \tilde{\mathbf{V}}_{AA} & \tilde{\mathbf{V}}_{AB} \\ \tilde{\mathbf{V}}_{BA} & \tilde{\mathbf{V}}_{BB} \end{bmatrix}, \quad (30)$$

where the indices of matrix elements describe the input sublattice and node sublattice, respectively. Finally, the Laplacian in Fourier space is determined by

$$\tilde{J}(k_x, k_y, k_z) = \tilde{\mathbf{I}}\tilde{\mathbf{V}}^{-1} = \frac{1}{\det \tilde{\mathbf{V}}} \begin{bmatrix} \tilde{\mathbf{I}}_{AA}\tilde{\mathbf{V}}_{BB} & -\tilde{\mathbf{I}}_{AA}\tilde{\mathbf{V}}_{AB} \\ -\tilde{\mathbf{I}}_{BB}\tilde{\mathbf{V}}_{BA} & \tilde{\mathbf{I}}_{BB}\tilde{\mathbf{V}}_{AA} \end{bmatrix} \quad (31)$$

The measured values depend on the frequency of the AC signal, but are fixed once decided upon. The frequency is chosen based on the theoretical position of the resonance frequency of the system, as well as absolute and relative deviations of the impedance spectra of the system's nodes.

### 3.2 Circuit Simulations

The simulations consist of building the Laplacian as seen in the example and then extracting the relevant information. This is done by fixing a node convention, assigning each column and row of the Laplacian a coordinate and then iterating over each matrix element. During this iteration, the coordinates of the column and row are compared and if the two nodes should be connected by a component, which depends on the model and boundary conditions, the relevant term from Tab. 3 is added, where the frequency  $\omega$  is left as a variable. This yields the Laplacian as a function of the frequency in real or reciprocal space. In the following, we focus on real space.

Real components never have the exact value given, but can deviate according to the specification of the manufacturer. Hence, if needed, such disorder can be taken into account by sampling each value of a component from a Gaussian that is centered around the ideal value and has a relative standard deviation given by the tolerance.

Further, one can include the resistances that real coils and capacitors have by adding a serial resistor. Then, the impedances are added up and one gets the following modifications to the terms in the Laplacian

$$\begin{aligned} i\omega C &\longrightarrow \frac{1}{R_C + 1/(i\omega C)}, \\ \frac{1}{i\omega L} &\longrightarrow \frac{1}{R_L + i\omega L}. \end{aligned} \quad (32)$$

Once the Laplacian is constructed, there are mainly two types of measurements one can compare the simulations to.

### 3.3 Bandstructure Simulations

The eigenvalues could be directly extracted via both approaches, however, the real space approach would require a Fourier transformation if one wants the quasimomenta. This is done via summation with the appropriate complex weights  $e^{-i\Delta x_{cr}k_x}$ ,  $e^{-i\Delta y_{cr}k_y}$ ,  $e^{-i\Delta z_{cr}k_z}$ , respectively, where  $\Delta x_{cr}, \Delta y_{cr}, \Delta z_{cr}$  are the differences of the coordinates of the columns and rows.

Alternatively, one can specify the currents and generate voltages as follows

$$\mathbf{V} = J^{-1}\mathbf{I}, \quad (33)$$

which allows to compare simulated voltages with measured voltages. Additionally, one can proceed with the generated data as described in Sec. 3.1.2, which seems like an overly complicated way to perform the above mentioned Fourier transform, but it helps to verify that the written code to extract the bandstructures works as intended.

To generate comparable data, a suitable current vector needs to be chosen. Under ideal conditions, all nodes that are equivalent after translation should have the same impedance  $Z_i = J_{ii}^{-1}$ , where  $J_{ii}^{-1}$  is the diagonal term of the inverted Laplacian for the node corresponding to  $i$ , by the same arguments as in Sec. 3.1.2. To be able to determine the current in an experiment, the voltage drop over a known shunt resistor  $R_{\text{Shunt}}$  is measured. Hence, for a source voltage  $V_{\text{Source}}$  and a total impedance of  $Z_{i,\text{Total}} = R_{\text{Shunt}} + Z_i$  the value of the current is given by Ohm's law

$$I_i = V_{\text{Source}}/Z_{i,\text{Total}}. \quad (34)$$

Thus, for each of the needed currents, the current vector corresponds to

$$\mathbf{I} = (0, 0, \dots, I_i, \dots, 0, 0)^{\text{T}}, \quad (35)$$

and is used to generate the voltages according to Eq. (33).

### 3.4 Impedance Simulations

The impedance of a node  $Z_i$  is obtained, as described above, by first inverting the Laplacian and then considering the diagonal term corresponding to a node. Though, this does not require the calculation of any current vector and is done as a function of  $\omega$ . This frequency sweep is of relevance due to the fact that it is used as a characterization method of the circuit.

## 4 Circuit Configurations

The purpose of this Sec. is to present the three different configurations that can be realized on the ETI circuit board. Interpolation between the different configurations is made possible by solder bridges, which add or remove components between the nodes.

In the following Secs., we present the schematics, components and connections, as well as the circuit Laplacians of the three configurations.

### 4.1 Weyl Circuit

The schematic of the WSM circuit unit cell is shown in Fig. 22, where A and B denote the sublattices, the black arrows indicate connections to other cells, the red paths indicate the connections to other layers in the z-direction and the red rectangles signify soldering bridges that are connected.

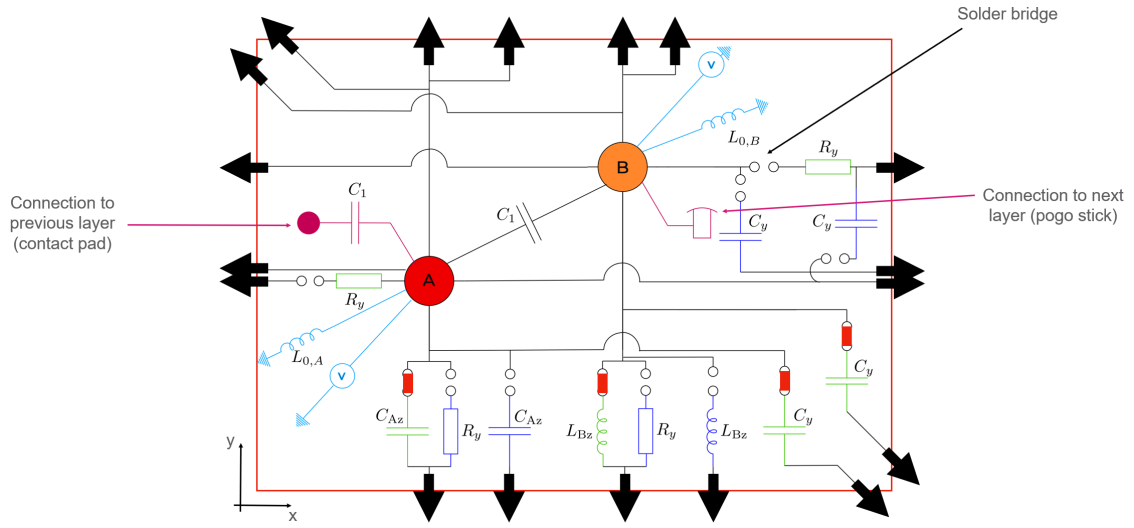


Figure 22: Schematic of the WSM circuit.

The voltage measurements, as indicated by the voltmeters, consist of measuring the potential of any point that is directly connected to the node, without passing through any components. Due to the periodicity, connections to other cells come with a phase factor depending on the direction, which allows the circuit Laplacian to be written directly in the Bloch Hamiltonian form. As an example, consider the capacitor  $C_{Az}$ , which connects the A sublattices in the y-direction, hence the term in the circuit Laplacian is given by  $C_{Az} e^{\pm i k_y}$  depending on whether one considers the connection in positive y-direction (-) or negative y-direction (+). The lattice constant was set to 1 in all directions, yielding the simplified form.

For clarity, the components are listed below along with the corresponding directional connections, which yield analogous phase factors.

Table 4: Components of the WSM circuit configuration that connect the nodes of the board.

|              | Same sublattice    | Different sublattice | Ground             |
|--------------|--------------------|----------------------|--------------------|
| Inter cell   | -                  | $C_1$                | $L_{0,A}, L_{0,B}$ |
| Y-direction  | $C_{A_z}, L_{B_z}$ | -                    | -                  |
| Z-direction  | -                  | $C_1$                | -                  |
| XY-direction | -                  | $C_y$                | -                  |

The values are as follow:

Table 5: Values of the used components.

| Component          | $C_y$ | $C_1$  | $C_{A_z}$ | $L_{0,A}$   | $L_{0,B}$  | $L_{B_z}$  |
|--------------------|-------|--------|-----------|-------------|------------|------------|
| Manufacturer Value | 75 nF | 150 nF | 150 nF    | 5.6 $\mu$ H | 27 $\mu$ H | 27 $\mu$ H |

Thus, the  $D, C$  and  $W$  matrices are given by

$$\begin{aligned}
 D &= i\omega \begin{pmatrix} 2C_{A_z} + 2C_1 + 2C_y & 0 \\ 0 & 2C_1 + 2C_y - \frac{2}{\omega^2 L_{B_z}} \end{pmatrix}, \\
 C &= i\omega \begin{pmatrix} 2C_{A_z} \cos(k_y) & C_1 + C_1 e^{-ik_z} + 2C_y \cos(k_y - k_x) \\ C_1 + C_1 e^{ik_z} + 2C_y \cos(k_y - k_x) & -\frac{2}{\omega^2 L_{B_z}} \cos(k_y) \end{pmatrix}, \\
 W &= i\omega \begin{pmatrix} -\frac{1}{\omega^2 L_{0,A}} & 0 \\ 0 & -\frac{1}{\omega^2 L_{0,B}} \end{pmatrix},
 \end{aligned} \tag{36}$$

and the circuit Laplacian is given by

$$\begin{aligned}
 J(\omega)/i\omega &= - \left[ \left( C_{A_z} - \frac{1}{\omega^2 L_{B_z}} \right) \cos(k_y) \right] \sigma_0 \\
 &\quad - [C_1 (1 + \cos(k_z)) + 2C_y \cos(k_y - k_x)] \sigma_x \\
 &\quad - [C_1 \sin(k_z)] \sigma_y - \left[ \left( C_{A_z} + \frac{1}{\omega^2 L_{B_z}} \right) \cos(k_y) \right] \sigma_z.
 \end{aligned} \tag{37}$$

As discussed in Sec. 1.3, this circuit exhibits 4 Weyl points at  $\mathbf{k}_{\text{Weyl}, 1, 2} = (0, \pm\pi/2, \pi)^\top$  and  $\mathbf{k}_{\text{Weyl}, 3, 4} = (\pi, \pm\pi/2, \pi)^\top$ . This can be seen by the low energy expansion near the Weyl points, which results in a dispersion of the form  $\pm \mathbf{k}\boldsymbol{\sigma}$ . By choosing  $\omega = \sqrt{\frac{1}{C_{A_z} L_{B_z}}}$  the  $\sigma_0$  coefficient in Eq. (37) vanishes, making the Weyl points touch at 0 energy.

It should be noted, that the form of Eq. (37) is only achievable in the case where  $L_{0,B}/L_{0,A} = 5$ . Unfortunately, components with this exact ratio were not available, which means that the  $\sigma_0$  and  $\sigma_z$  coefficients have a small, non-vanishing term. But as mentioned in Sec. 1.3, this simply shifts the Weyl points slightly and is therefore ignored in the following.

### 4.1.1 OBC Adjustment

For PBC, the capacitor in the B sublattice of the top board is connected to the bottom board due to periodicity. In the case of OBC, the bottom board has no connection to the previous layer, which means that the A sublattice is missing a  $C_1$  capacitor. Therefore, OBC connectors are used to compensate for this, as shown in Fig. 23.

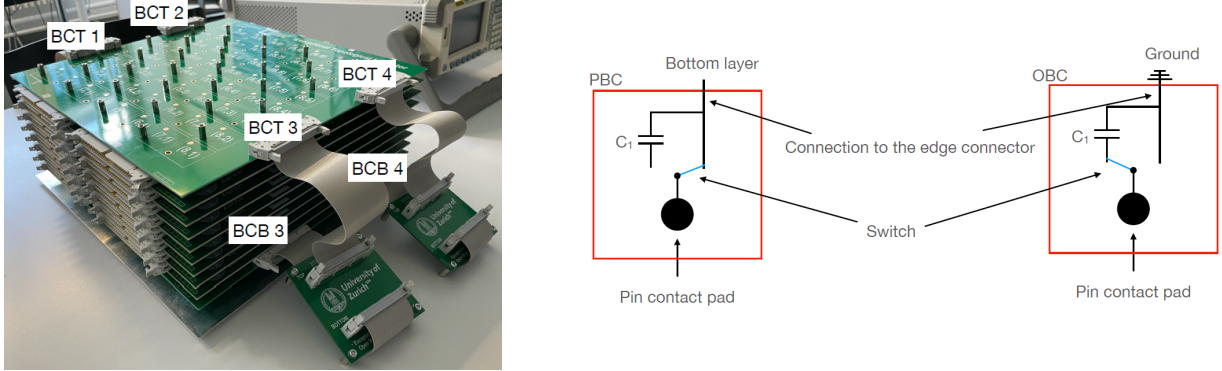


Figure 23: ETI circuit board with the OBC connector boards (left) and the schematic of the OBC connectors (right), showing the additional  $C_1$  capacitor needed to compensate for OBC.

The A sublattice is therefore connected to ground via this additional  $C_1$  capacitor. Likewise, the B sublattice capacitor is connected to ground.

### 4.2 Trivial Non-Hermitian Configuration

For the trivial NH circuit the soldering bridges change, indicated by blue rectangles, to also enable next-nearest (NN) neighbor hopping in the y-direction, indicated by the grey arrows.

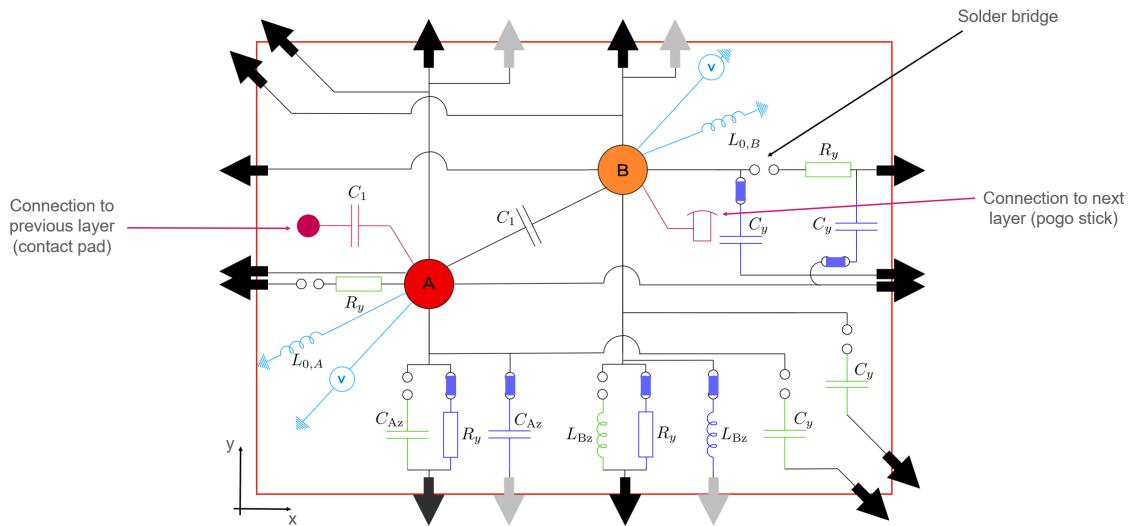


Figure 24: Schematic of the trivial NH circuit

The components and directional connections are

Table 6: Components of the trivial NH configuration that connect the nodes of the board.

|             | Same sublattice         | Different sublattice | Ground             |
|-------------|-------------------------|----------------------|--------------------|
| Inter cell  | -                       | $C_1$                | $L_{0,A}, L_{0,B}$ |
| X-direction | -                       | $C_y$                | -                  |
| Y-direction | $C_{A_z}, L_{B_z}, R_y$ | -                    | -                  |
| Z-direction | -                       | $C_1$                | -                  |

The components have the same values shown in Tab. 5, as well as the resistor with  $R_y = 15.92 \Omega$ .

This yields the matrices

$$\begin{aligned}
 D &= i\omega \begin{pmatrix} 2C_{A_z} + 2C_1 + 2C_y - \frac{2i}{\omega R_y} & 0 \\ 0 & 2C_1 + 2C_y - \frac{2}{\omega^2 L_{B_z}} - \frac{2i}{\omega R_y} \end{pmatrix}, \\
 C &= i\omega \begin{pmatrix} 2C_{A_z} \cos(2k_y) - \frac{2i}{\omega R_y} \cos(k_y) & C_1 + C_1 e^{-ik_z} + 2C_y \cos(k_x) \\ C_1 + C_1 e^{ik_z} + 2C_y \cos(k_x) & -\frac{2}{\omega^2 L_{B_z}} \cos(2k_y) - \frac{2i}{\omega R_y} \cos(k_y) \end{pmatrix}, \\
 W &= i\omega \begin{pmatrix} -\frac{1}{\omega^2 L_{0,A}} & 0 \\ 0 & -\frac{1}{\omega^2 L_{0,B}} \end{pmatrix},
 \end{aligned} \tag{38}$$

and the Laplacian

$$\begin{aligned}
 J(\omega)/i\omega &= - \left[ \left( C_{A_z} - \frac{1}{\omega^2 L_{B_z}} \right) \cos(2k_y) + i \frac{2}{\omega R_y} (1 - \cos(k_y)) \right] \sigma_0 \\
 &\quad - [C_1 (1 + \cos(k_z)) + 2C_y \cos(k_x)] \sigma_x - [C_1 \sin(k_z)] \sigma_y \\
 &\quad - \left[ \left( C_{A_z} + \frac{1}{\omega^2 L_{B_z}} \right) \cos(2k_y) \right] \sigma_z.
 \end{aligned} \tag{39}$$

This configuration separates Weyl points of the same chirality, forming a trivial point gap, and is therefore called trivial.

### 4.3 Non-Hermitian TI Configuration

The non-trivial NH configuration has again only nearest neighbor hoppings and the soldered bridges are indicated by the green rectangles.

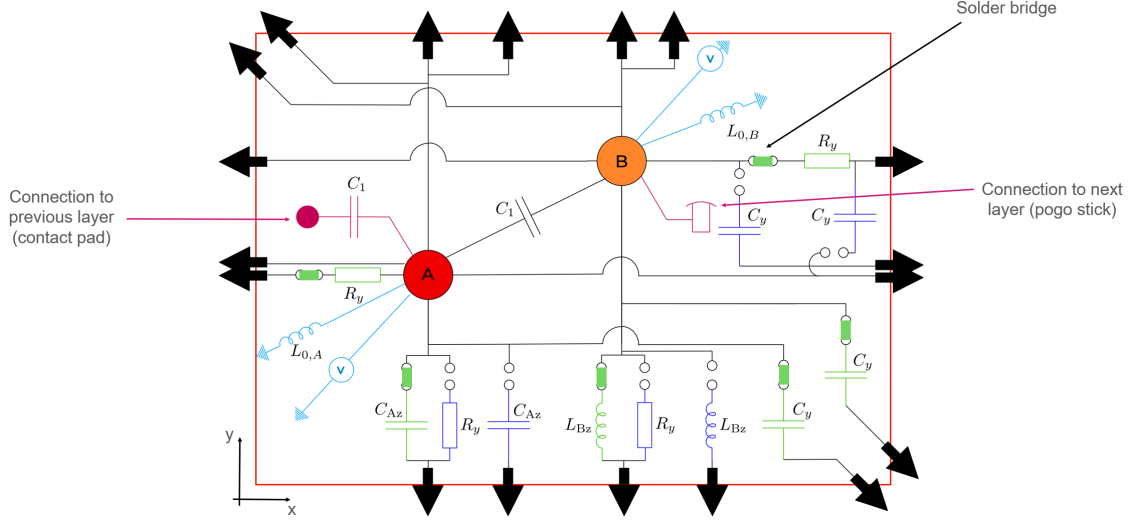


Figure 25: Schematic of the non-trivial NH circuit

The connecting component are

Table 7: Components of the NH configuration that connect the nodes of the board.

|              | Same sublattice  | Different sublattice | Ground             |
|--------------|------------------|----------------------|--------------------|
| Inter cell   | -                | $C_1$                | $L_{0,A}, L_{0,B}$ |
| X-direction  | $R_y$            | -                    | -                  |
| Y-direction  | $C_{Az}, L_{Bz}$ | -                    | -                  |
| Z-direction  | -                | $C_1$                | -                  |
| XY-direction | -                | $C_y$                | -                  |

$D, C$  and  $W$  are then given by

$$\begin{aligned}
 D &= i\omega \begin{pmatrix} 2C_{Az} + 2C_1 + 2C_y - \frac{2i}{\omega R_y} & 0 \\ 0 & 2C_1 + 2C_y - \frac{2}{\omega^2 L_{Bz}} - \frac{2i}{\omega R_y} \end{pmatrix}, \\
 C &= i\omega \begin{pmatrix} 2C_{Az} \cos(k_y) - \frac{2i}{\omega R_y} \cos(k_x) & C_1 + C_1 e^{-ik_z} + 2C_y \cos(k_y - k_x) \\ C_1 + C_1 e^{ik_z} + 2C_y \cos(k_y - k_x) & -\frac{2}{\omega^2 L_{Bz}} \cos(k_y) - \frac{2i}{\omega R_y} \cos(k_x) \end{pmatrix}, \\
 W &= i\omega \begin{pmatrix} -\frac{1}{\omega^2 L_{0,A}} & 0 \\ 0 & -\frac{1}{\omega^2 L_{0,B}} \end{pmatrix},
 \end{aligned} \tag{40}$$

and the circuit Laplacian is

$$\begin{aligned}
 J(\omega)/i\omega &= - \left[ \left( C_{Az} - \frac{1}{\omega^2 L_{Bz}} \right) \cos(k_y) + i \frac{2}{\omega R_y} (1 - \cos(k_x)) \right] \sigma_0 \\
 &\quad - [C_1 (1 + \cos(k_z)) + 2C_y \cos(k_y - k_x)] \sigma_x - [C_1 \sin(k_z)] \sigma_y \\
 &\quad - \left[ \left( C_{Az} + \frac{1}{\omega^2 L_{Bz}} \right) \cos(k_y) \right] \sigma_z.
 \end{aligned} \tag{41}$$

The complex valued  $\sigma_0$  term gives the Weyl points of opposite chirality different life times and therefore creates a point gap. The Fermi arc then fill this gap with non-Hermitian surface localized states, as illustrated in Fig. 18.

## Part III

# Experimental Setup

There are only three types of measurements performed on the circuit boards: Bandstructure, impedance or surface propagation measurements, which have a similar setup and in the simplest case only require a function generator and an oscilloscope. Here, a lock-in amplifier was used (see Fig. 26) which acts as a function generator and demodulator.



Figure 26: Picture of the MLA lock-in with the different ports in gold. 3 of the ports show the converters needed to be able to connect to BNC cables (silver).

The lock-in is used to send in a simple voltage sine wave of the form

$$V(\omega, t, \delta) = V_0 \sin(\omega t + \delta_0), \quad (42)$$

where  $V_0$  is the amplitude,  $\omega$  the angular frequency and  $\delta_0$  the initial phase shift of the signal.  $\delta_0$  is usually set to 0, while  $V_0$  and  $\omega$  can vary from measurement to measurement. The lock-in then measures an incoming signal and tries to fit Eq. (42) to a set of data points for a specified frequency  $\omega_0$ , yielding the measured quantities  $V_m$  and  $\delta_m$ . Since the lock-in generates the reference signal,  $V_0$  and  $V_m$  use the same ground and  $\delta_m$  is the phase relative to  $\delta_0$ . Using different ways of processing this data, the variety of results presented in Sec. IV can be obtained.

In the following Secs., the circuit boards, measurement methods and setups are presented.

## 5 ETI Circuit Board

Each unit cell has 16 different components, where each configuration uses only a subset thereof. The solder bridges are connected with the help of solder, which can be easily removed to open a bridge. An example can be seen in the bottom left corner of Fig. 27, where two solder bridges are connected on the right of the  $CYd$  and  $CYc$  capacitors.

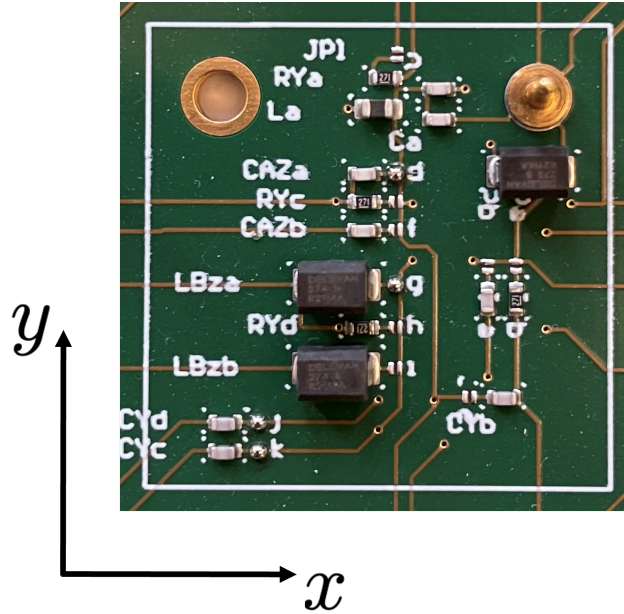


Figure 27: Unit cell with all the components required for the 3 different configurations and soldered bridges for the WSM configuration. The golden pins are the connections for the top layer, touching the golden pads seen on the right of Fig. 28. The golden ring on the top left allows to screw together the different layers using bolts, as can be seen in Fig. 29.

The voltages of the nodes can be directly accessed, if the unit cell is exposed, by measuring at the golden pin for the B sublattice, and to the right of the solder of the  $CAZa$  capacitor for the A sublattice. As mentioned before, any point that is directly connected to these points works as well. Therefore, the nodes are internally rerouted to the sides of the boards, which is not visible from the outside. At the sides, all the rerouting tracks are connected to flat band ribbons, as seen in Fig. 28.

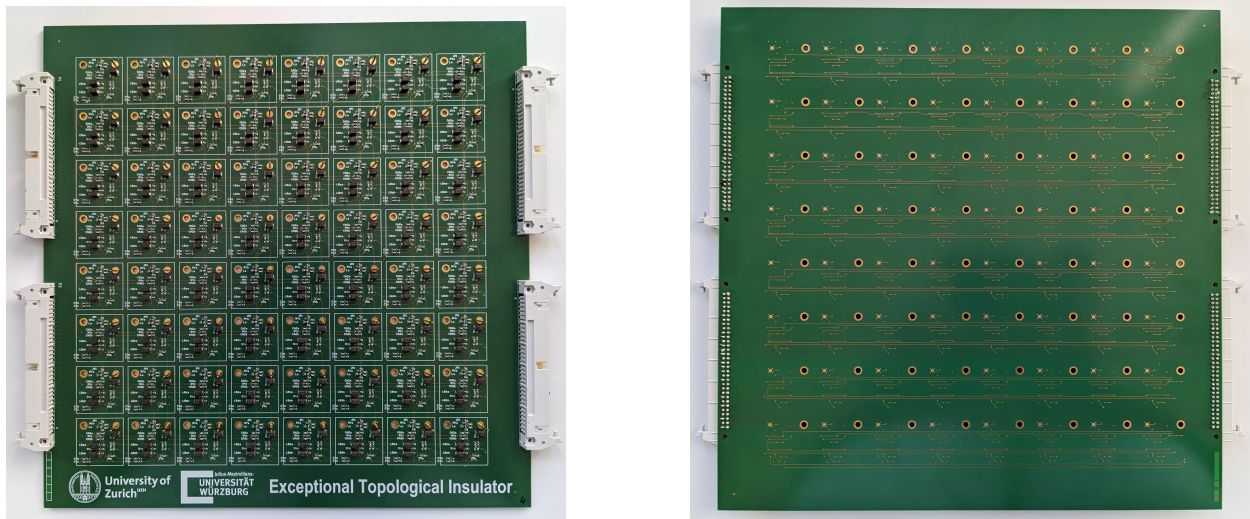


Figure 28: Front of a single layer with the  $8 \times 8$  unit cells (left) and back of the single layer with the golden pads for the z-connection and the PBC tracks in the x-direction (right). The PBC tracks in the y-direction are inside the layer and not visible from outside. Each layer has 4 connectors for the flat band ribbons, where each connector allows the measurement of a  $4 \times 4$  quadrant.

In total there are 8 such single layers, which in theory should all be equivalent. The boards are then placed on top of each other and fixated by bolts. The whole stack of boards is situated

between two connector layers, which only connect to the neighbouring boards and do not have any components built on. These connector layers also have flat band ribbons at the sides, which enable PBC in the  $z$ -direction or the OBC capacitor to be added, as explained in Sec. 4.1.1. The built circuit without the top connector layer is shown in Fig. 29.



Figure 29: ETI circuit with the 8 layers sitting on the bottom connector layer and without top connector layer. The front connectors enable to couple the top and bottom layers, while the  $x$ - and  $y$ -directions are always periodically connected. On the sides of each board are the connectors that allow for the measurements via a BNC board.

BNC boards can be connected to the flat band ribbons, which then allow the individual nodes to be accessed by the lock-in. There are a total of four BNC boards, which all look as shown in Fig. 30.

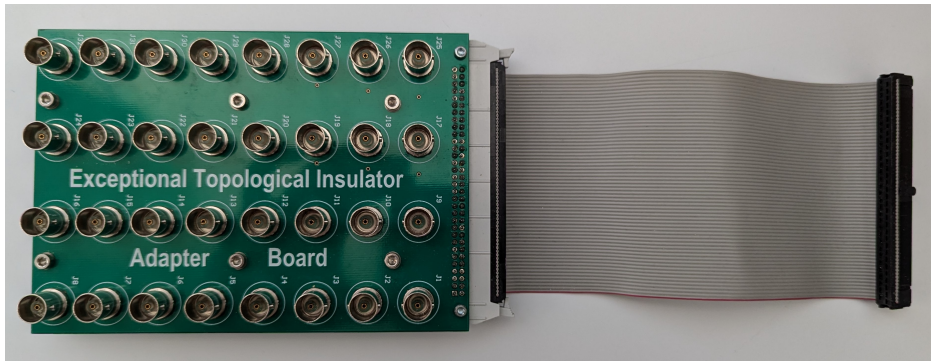


Figure 30: BNC board with the BNC adapter corresponding to different nodes, indicated as J1 to J32.

## 5.1 Multiplexer Boards

An alternative to the BNC adapters for measurements are the multiplexer boards. The boards attach at the same position as the adapters, however, they have the added benefit of being able to be controlled via software and switch between the nodes.

The boards have been built by the colleagues in Würzburg and they also wrote the code to steer them. The board itself connects one of the ETI's board's quadrants with the multiplexer unit.

Additionally, there is an LED lamp to indicate if the board is working properly. The board is also connected to the computer, which allows to switch between the different channels of the multiplexer. This corresponds to connecting to different nodes of the quadrant the board is connected to.

Since we do not have the equipment to use the multiplexer boards in Zurich, they were only used in Würzburg to measure the fully built ETI. For the search of error sources, they were not available anymore.

## 6 Board Measurements

In this Sec., the three measurement setups for the three types of experiments are presented. The setups are very similar to each other and mostly vary in the positions of input and output nodes, as well as the number of measurements needed to extract the desired information.

### 6.1 Impedance Measurements

Impedance measurements are done by applying a potential at a node and measuring the voltages as shown in Fig. 31.

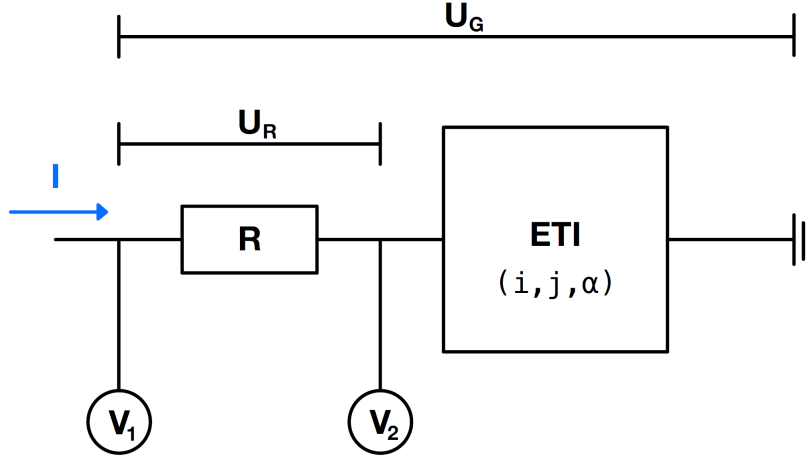


Figure 31: Measurement setup for impedance measurements showing the grounded ETI circuit, the shunt resistor  $R$  used to determine the current  $I$  and the two voltages  $V_1, V_2$  that are measured using the lock-in. The indices  $(i, j, \alpha)$  stand for the x-position, y-position and sublattice to indicate the different nodes of the ETI.

Since the ETI itself is grounded, the whole potential drop has to occur via the shunt resistor  $R$  and the ETI. Hence, a signal of the form of Eq. (42) is applied, where the specific parameters are not relevant, and  $V_1, V_2$  are measured using the lock-in. The impedance of a node of the ETI is then given by Ohm's law as

$$\begin{aligned} Z_{ETI} &= \frac{U_G - U_R}{I}, \\ &= \frac{V_1 - (V_1 - V_2)}{I}, \\ &= \frac{V_2}{I}. \end{aligned} \quad (43)$$

However, the current is not known, which is why the shunt resistor is required, as the current can be expressed as

$$\begin{aligned} I &= \frac{U_R}{R}, \\ &= \frac{V_1 - V_2}{R}. \end{aligned} \quad (44)$$

Therefore, the impedance is given by

$$Z_{ETI} = \frac{V_2}{V_1 - V_2} \cdot R \quad (45)$$

This is done for every node and for a range of angular frequencies  $\omega_0$ , usually from 1 MHz to 5 MHz, where the input and measurements of  $V_1$  and  $V_2$  are performed at the same node.

## 6.2 Frequency Determination

Impedance measurements happen at various frequencies using a frequency sweep. The range of the frequencies lies between 100 kHz and 10 MHz, and varies depending on the experiment.

For the subsequent measurement types, however, a specific frequency is needed at which the measurement happens. The suited frequency for such an experiment depends on the set-up and board configuration, and has been changed over time as new insight was acquired. Initially, the frequency was chosen to be the theoretically calculated eigenfrequency of the WSM system given by  $f = \frac{1}{2\pi} \sqrt{\frac{1}{C_{Az}L_{Bz}}} \approx 2.5$  MHz. However, due to the unsatisfactory results the frequency was adapted. The new frequency should still be in the vicinity of the theoretical eigenfrequency. However, due to the variance in the impedance spectra of the different nodes, the new frequency should also be at a position where this variance is small. Small variance in this case refers to either the absolute value of the variance or the relative variance with respect to the mean of the impedance.

In the early stages of this project, the former variance was determined by measuring the impedance spectrum of every node and then calculating the variance as a function of the frequency for the two sublattices separately. Then, the smallest variance value near 2.5 MHz was determined by adding the variances of the two sublattices, as well as the corresponding frequency. This approach, however, has two significant flaws. Firstly, the variance may be small, but so is the mean value at that position. This gives rise to a bias towards smaller impedance values. Secondly, we do not consider that the sublattices have different impedance spectra. Therefore, adding the two sublattices' variances treats them automatically equally impactful.

Furthermore, additional frequencies in the vicinity of 2 to 2.5 MHz have been explored to assess whether the results improve and how it affects the measurements.

In the second half of this project, which consisted of mainly determining the error sources of the boards, we tried to eliminate these shortcomings. The new approach was to normalize the variances of the sublattices with the corresponding means at each frequency. The new variance values were not resistances anymore, but rather numbers that expressed the variances as a multiple of the corresponding mean values. An example of the new spectra are shown in Fig. 32.

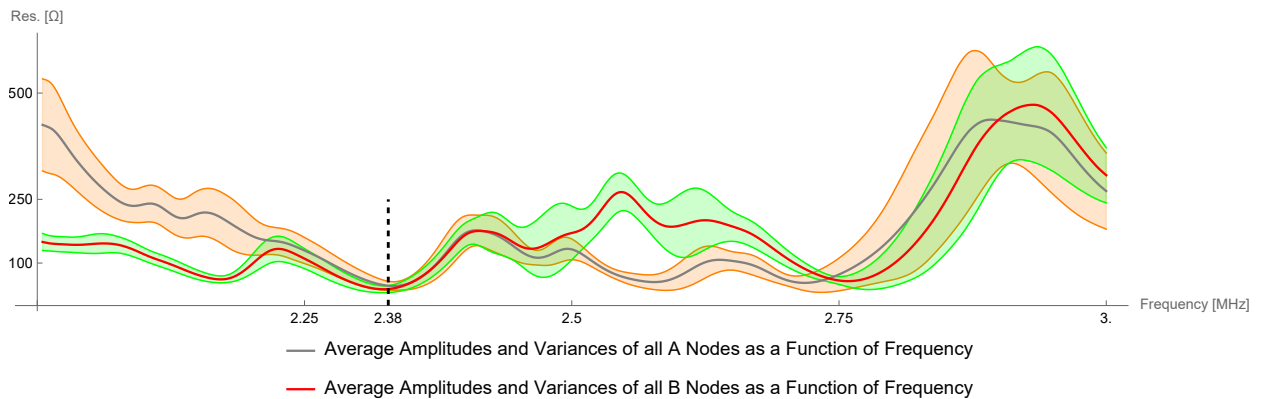


Figure 32: Average impedance and variance spectra of the two sublattices around 2.5 MHz. The vertical black line shows the frequency with minimal, added, relative variance.

Adding the relative variances of the two sublattices now includes the different means as the statistical weights. This approach also automatically accounts for the fact that smaller values yield smaller absolute variances. The minimal, added, relative variance is then the frequency we used as a suitable frequency.

### 6.3 Bandstructure Measurements

The setup for the bandstructure measurements are similar to that of the impedance measurements, which only differ by the fact that the input and measured node don't have to be the same. This means that the sent in signal travels through a portion of the ETI, depending on the input and measurement nodes, and is then measured as  $V_3$  as illustrated in Fig. 33.

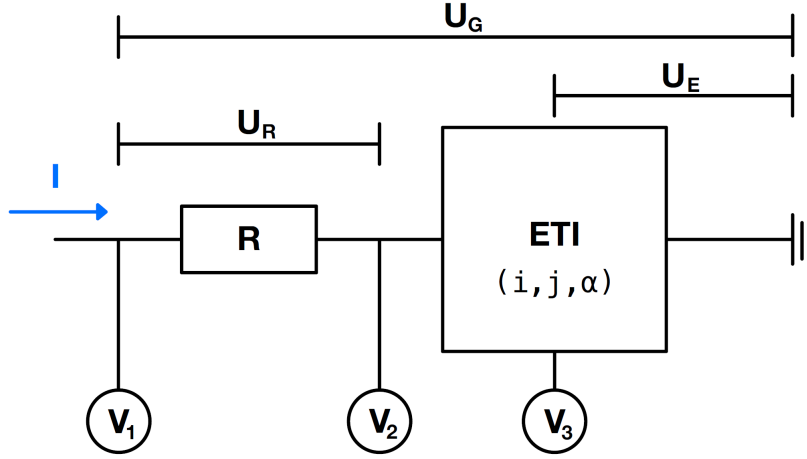


Figure 33: Measurement setup for bandstructure measurements, which only differ from the impedance setup by the point at which the voltage is measured, denoted as  $V_3$ , which can coincide with  $V_2$ .

$V_1$  and  $V_2$  do not have to be measured for each node, but only once for each required current input, assuming that the impedances of the nodes don't vary too much from each other. Since at one point the input and measured node will coincide, the bandstructure and impedance measurement setups are the same and the currents are determined as described in Eq. (44).

Therefore, for each required current input a node is chosen and the whole board is measured. Once all the  $V_3$ 's are measured and the used currents determined, the Laplacian is determined as described in Sec. 3.1.2 and its bandstructure extracted.

#### 6.3.1 Current Stabilization

Normally, during the measurement of a node, the voltage of the lock-in amplifier is kept constant with respect to the built in ground level. Under the assumption of translational invariance, this would cause an equal current to flow in to each of the nodes, while the amount depends on the sublattice. If the translational symmetry is broken, however, the current differs between each node. Due to the difficulties of the bandstructure measurements, an attempt was made to instead focus on supplying a constant current and to adjust the voltage to achieve this.

As we are working in the linear regime of Ohm's law, altering the current will proportionally alter the measured voltages. The impedances, however, are unaffected by this and therefore the admittances as well. This ensures that the bandstructure is still measured correctly.

The feedback loop compares the current from Eq. (44) to a given target value and increases the voltage if the current is too small or vice versa. This loop was set-up by the colleagues in Würzburg, as it requires equipment that was only available there. It was therefore only used for a short period of time in order to test for possible differences.

## 6.4 Surface Propagation

The excitation of the Fermi arc is the most complex of the three measurements, as it requires the largest amount of measuring ports at a time. Two B or A sublattice nodes of adjacent unit cells in the x-direction on the top or bottom layer, respectively, are chosen and are fed in a signal, whose relative phase between the two is either  $\pi/2$  or  $3\pi/2$ . This excites only one of the Fermi arcs shown in Fig. 11 and should cause the pulse to only propagate along the y-axis.

The measured quantities are again the voltages  $V_3$ , however, they are measured for a few oscillations and the measurements of all the nodes have to be timed, as well as measured simultaneously. Each node can then be fitted according to Eq. (42), which yields the amplitude and phase of each node, relative to the inputs.

However, it is not possible to instantly achieve the excitation of a relative phase of  $\pi/2$  between two sites, because this means that the individual pulses will spread in all directions until the signals are able to interact with each other and interfere. Additionally, these measurements require a lot more equipment and are therefore very elaborate. As will become apparent, the OBC bandstructure measurements did not yield the desired results and therefore the surface propagation measurement was not tested extensively, as no Fermi arc was observed.

## Part IV

# Experimental Findings

This part presents the results obtained from the experiments, provides an in-depth analysis of their interpretation, and discusses potential areas for improvement. Firstly, the findings of the WSM circuit board are presented, which include bandstructures for PBC and OBC, as well as the Chern numbers. Secondly, the analysis for possible error sources and improvements is presented, the results of which can be used for future projects of this kind.

Due to the large amount of measurements performed, generally, only one representative for one approach is shown. For the WSM circuit experiments, this means that only the results that look most similar to the theory are shown. For the second part, enough data is shown to illustrate the suspicions and justify the conclusions, but it should be noted that more data is available to support this. The data is available at <https://github.com/Hafefif/ETI-Master-Thesis.git>.

## 7 Weyl Semimetal Measurements

This Sec. will show the results of the WSM circuit board, which are divided in to two iterations: 8 and 6 boards in the vertical direction. The reason for this is the elimination of the two worst performing boards, as will become apparent in the following Secs..

Furthermore, each iteration is split in to PBC and OBC. The PBC case includes the Chern number to characterize the phase, while for OBC the surface transport experiments are shown if available. Here, the arguably best results are presented, which might have been measured at different frequencies for different properties.

### 7.1 8-Boards

The frequency of 2.5 MHz was initially used, but then quickly changed according to impedance measurements performed, where new frequencies where chosen as described in Sec. 6.2. This lead to different measurements at different frequencies, however, no ideal frequency could be determined, as some properties agreed better with the theoretical predictions at different frequencies.

#### 7.1.1 PBC Bandstructure

In Fig. 34 the bandstructure along the high symmetry path is shown for both measurement and theory at a frequency of 2.285 MHz.

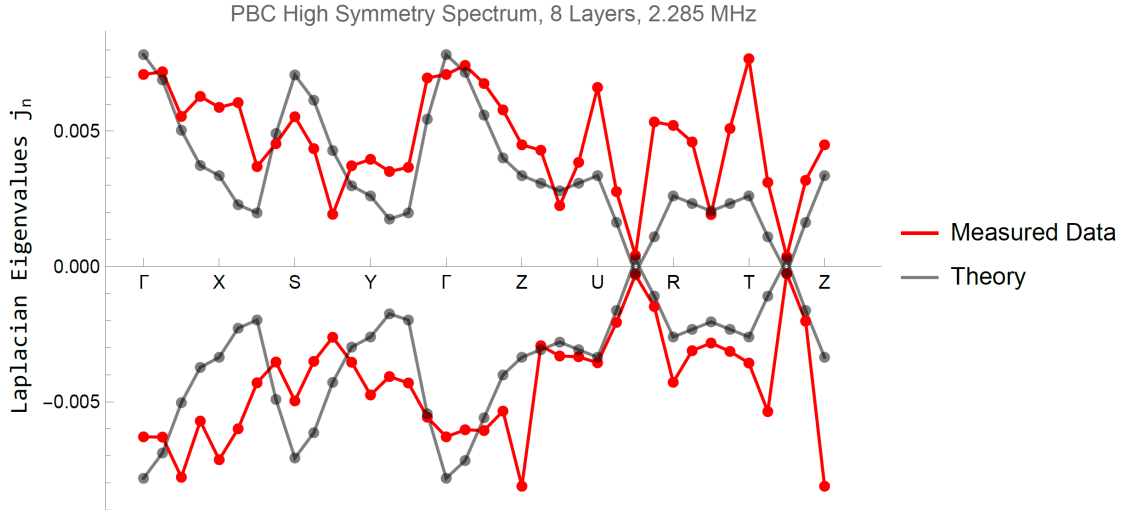


Figure 34: PBC spectrum for 8 boards in the WSM configuration. The letters of the horizontal axis indicate points in the WSM BZ as covered in Fig. 8. The theoretical bandstructure has been scaled by a factor of 120.5 to match the measurements.

As one can see, it appears that the general trend of the measured bandstructure aligns with the theoretical prediction. Especially at the location of the Weyl points, the two seem to agree quite well. However, it is clear that the circuit board does not simulate the WSM as intended, yet. Apart from the deformation of the band structure, there are also sudden spikes present in the data, as well as an asymmetry between the upper and lower bands.

The deviations in the bandstructure indicate that not all unit cells behave the same, which is also seen in the impedance spectra. Therefore, the translational symmetry of the system is broken with various possible sources. The problem could be with the components of the unit cells themselves, which would lead to deviations in the impedances. One would expect such effects to be randomly distributed and small, since the components were chosen to have a small tolerance. Another source of random deviations could be related to the boards, where it is caused by differences in the boards. Since the spikes do not seem to follow any obvious systematic pattern, it is plausible that these deviations are larger than initially expected.

Even if the 8 different boards, as well as the components on them are exact replicas, the problem could be the chosen layout of the boards. This includes connections between the unit cells within one of the boards, connections between two boards, as well as connections needed for PBC. Such effects should manifest themselves as more systematic deviations and would require the analysis of the isolated single boards.

The band asymmetry indicates that there are influences which affect the sublattices differently, which seems to be a general trend observed in many measurements, and could stem from such systematic board effects. Another conspicuous feature is the fact that the Weyl points are not sampled by the high-symmetry path, which is due to the choice of components and frequency. As mentioned in Sec. 4.1, the WSM model imposes certain conditions for the components, which could not be met for this circuit board. The result is a slight, frequency independent shift of the Weyl points. As a result of the momentum resolution in the finite circuit, it seems as if the Weyl points separated, while in reality they just moved to a different momentum. The fact that the system is still gapless can be seen from the calculation of the Chern number, as shown in Fig. 35.

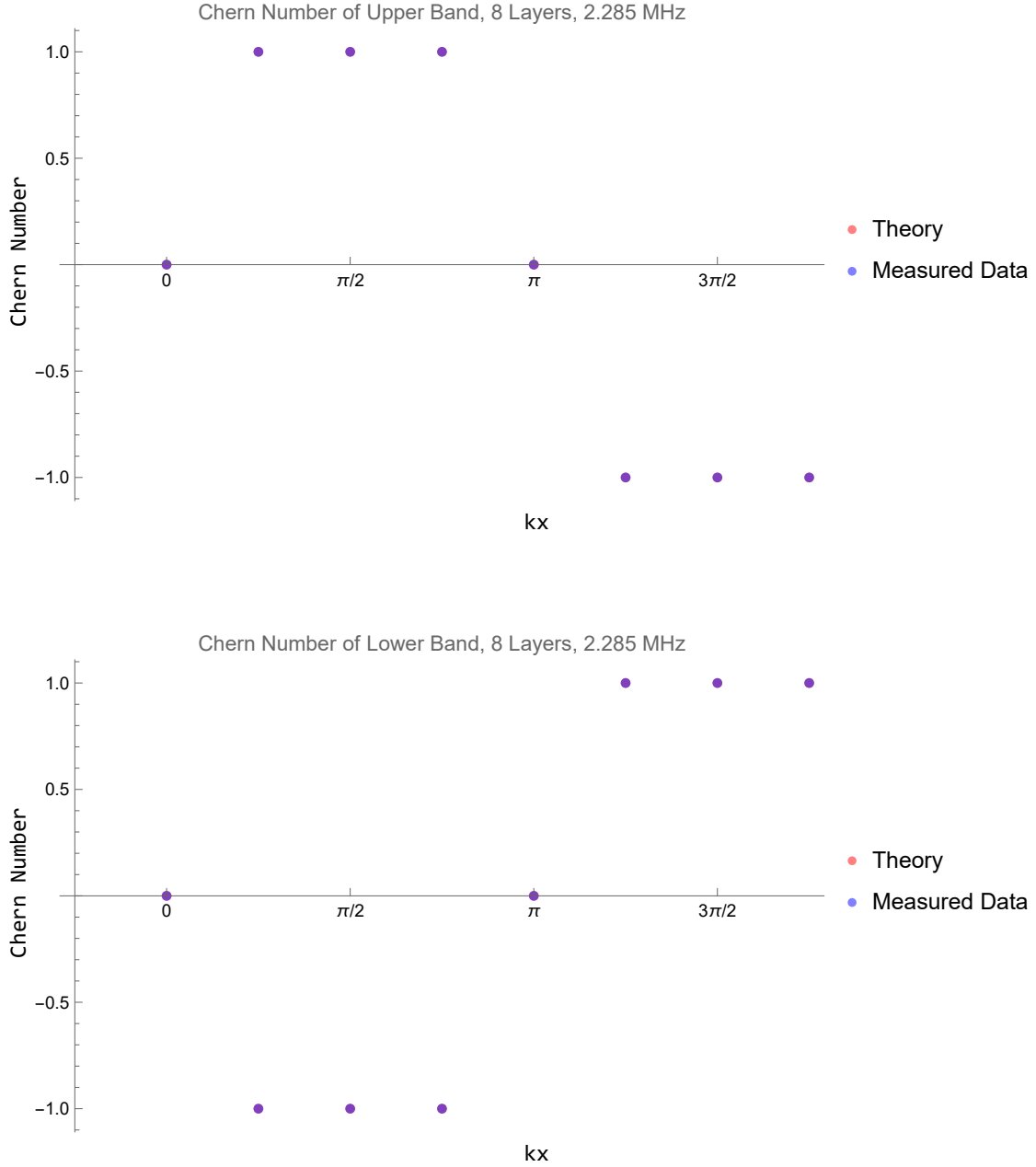


Figure 35: Chern numbers of the two bands for the 8 board WSM configuration, as a function of the  $k_x$  momentum, since the  $k_y, k_z$  have been integrated over. The two bands should always exhibit opposite Chern numbers, since the WSM as a whole is not gapped and therefore has a total Chern number 0 for each  $k_x$ .

The experimental Chern numbers, calculated as described in Sec. 1.1.1, agree with the theory, despite the deviations in the bandstructures. The topological nature of the system could be the reason why it remains stable against such variations.

### 7.1.2 OBC Bandstructure

In the case of OBC, each board will yield two bands, resulting in 16 bands whose bandstructure are shown in Fig. 36.

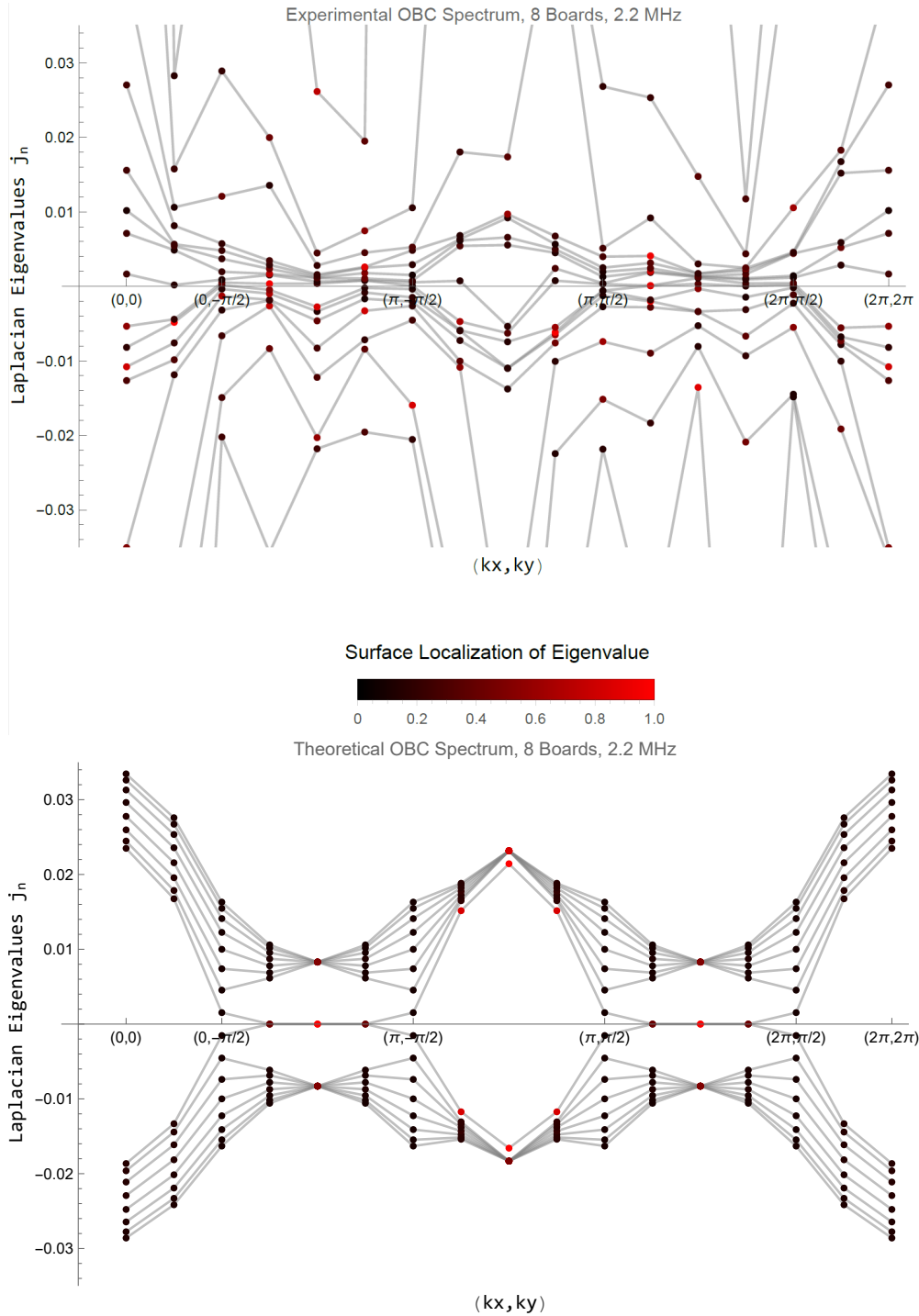


Figure 36: OBC spectrum along the high symmetry path of the 8 board WSM configuration (top), where the range of the eigenvalues  $j_n$  is limited to maintain the overview and the theoretical bandstructure (bottom) for comparison.

The measured OBC bandstructure doesn't really resemble the theoretical one at all, except maybe the center part. The eigenvalues of the outer most bands are too high, the Fermi arc is not really recognizable as the bands cluster together around the zero energy and the surface localization of

the eigenvalues seems to be completely random. The OBC spectrum suggests that the system is more sensitive to deviations for OBC than for PBC, but the reason for this is not known.

The initial measurements showed strong deviations from the theoretical bandstructure, where the sources are not yet known. The next step was thus to study the system in order to optimize the circuit. As mentioned above, the current suspicions are disorder, either from the components or the boards, as well as unexpected influences on the behaviour due to the board layout. Further, to ensure the problem is not with the way the measurements are made, the measurement process has been rechecked.

Due to the large discrepancy, no surface transport measurements were performed and instead the system size was reduced to only 6 boards, as explained in the following Sec..

## 7.2 6-Boards

The bad results of the previous Sec. led to the reduction of the layers from 8 to 6, where the two boards with the most variance in their impedance spectra were discarded. The idea was to reduce disorder and therefore increase the similarity of the unit cells. Apart from the change in layers and drive frequency that is adjusted to the new system, the current input was stabilized to a constant value using a feed-back loop in order to counteract the variance in impedance. Then the measurements were repeated analogously to the 8 board case.

### 7.2.1 PBC Bandstructure

In the 6 board configuration, the new, suitable frequency is 2.4 MHz, which has been determined using the same criteria as described in Sec. 6.2. The bandstructure can be seen in Fig. 37.

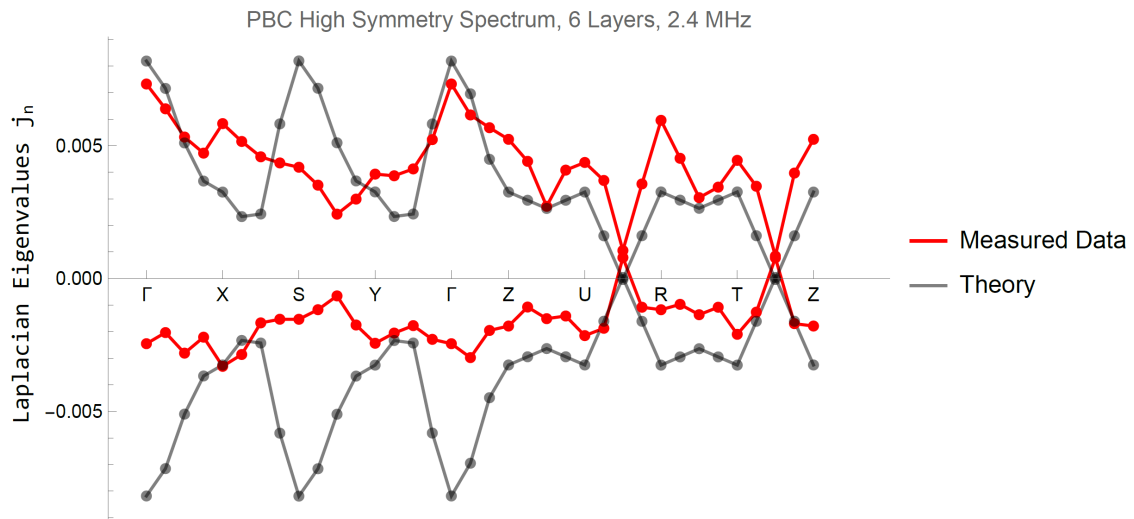


Figure 37: PBC spectrum for 6 boards in the WSM configuration with a current stabilized input. The theoretical bandstructure has been scaled by a factor of 120.5 to match the measurements.

The bandstructure for 6 boards has a few differences from its 8 board counterpart. Firstly, the bands are not centered around 0 anymore, which is not reflected in the theoretical bandstructure. It is therefore strange to observe this shift when changing the number of layers. It could therefore be an indication that the PBCs of the system do not behave as expected. This was not specifically tested, as the fine-tuning of the bandstructure had no priority and other experiments were planned already to test for the system's translational invariance.

Secondly, the sudden spikes seem to be smaller in magnitude but the bandstructure as a whole still does not match. Thirdly, the lower band seems to yield consistently lower eigenvalues than expected. This asymmetry in the bands is hard to account for, since the theoretical bandstructure does not indicate such a behaviour either. The effects of the current stabilization are too weak, as will be seen in the later Sec. 9.2, to cause this, and the only difference left is the number of boards again. It could therefore very well be due to the same reason the energies are not centered around zero.

Except for the reduction in the magnitude of the lower band eigenvalues, the bandstructure seems to resemble the theory. It is however difficult to judge if it improved or not. Interestingly enough, even with the shifts and asymmetries of the bandstructure, the calculated Chern numbers of the bandstructure match very well with the theory again, as can be seen in Fig. 38.

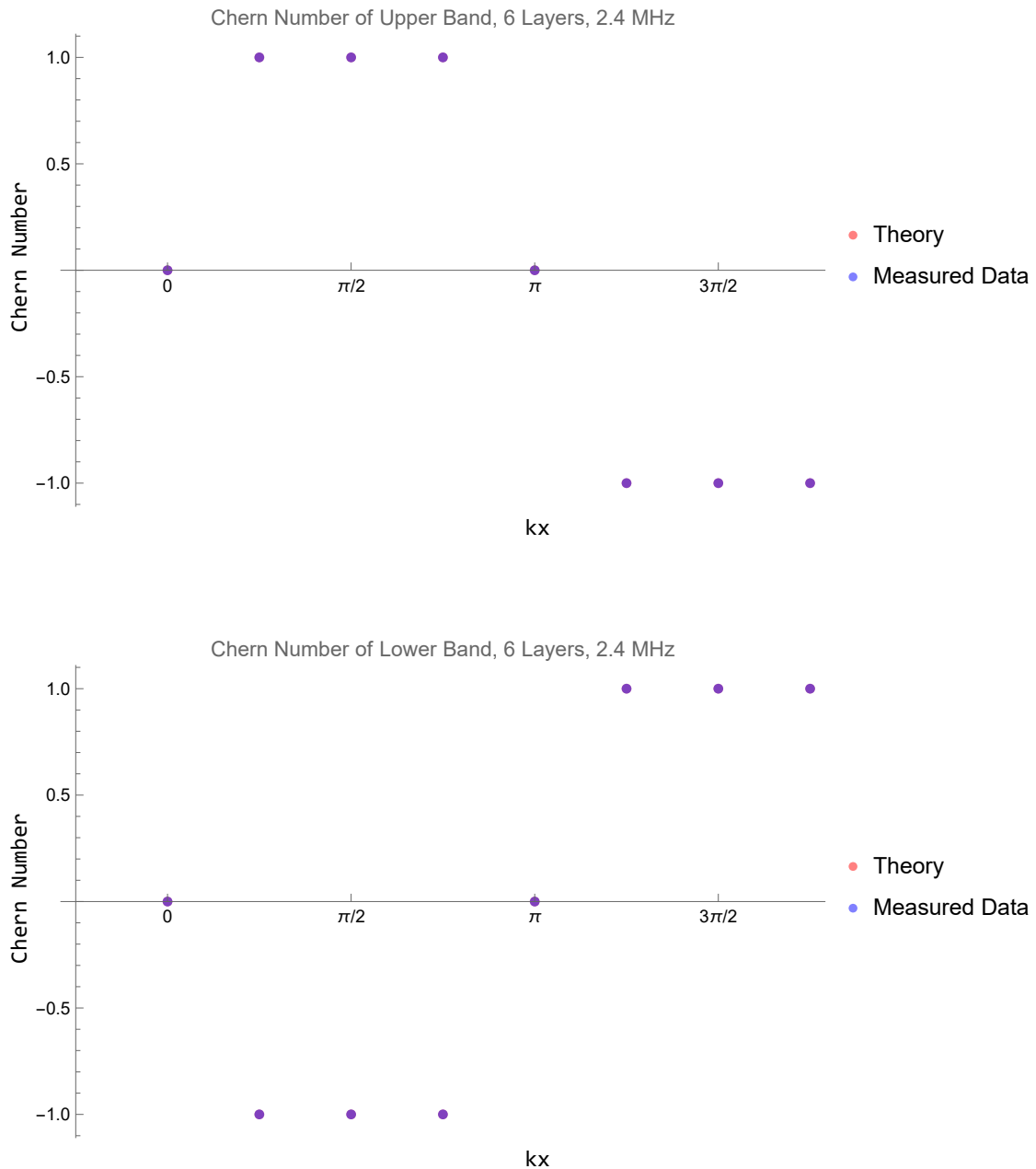


Figure 38: Chern numbers of the two bands for the 6 board WSM configuration with a current stabilized input.

### 7.2.2 OBC Bandstructure

The suitable frequency analysis for the OBC measurement of the 6 board WSM yielded the same frequency of 2.4 MHz and the bandstructure can be seen in Fig. 39.

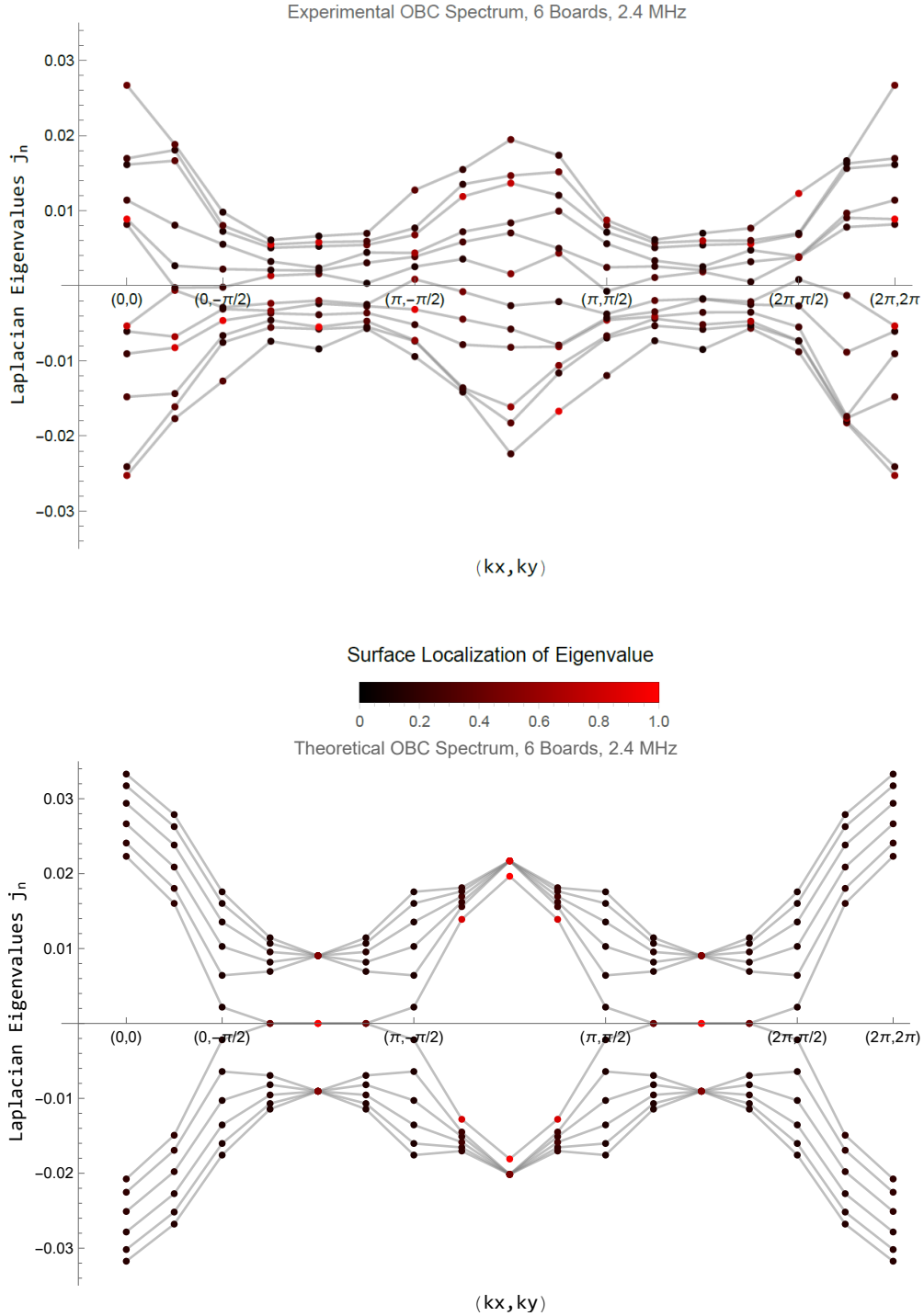


Figure 39: OBC spectrum along the high symmetry path of the 6 board WSM configuration with a current stabilized input (top) and the theoretical bandstructure (bottom).

Compared to its 8 board counterpart, the general structure of this bandstructure resembles the theory much more. The eigenvalues are of the same magnitude, but the Fermi arc is still not visible. Again, the bands seem to cluster together where the Fermi arc should be and there is also no surface localization of the eigenvalues to indicate its observation.

Lastly, an attempt was made to observe the monodirectional propagation of the Fermi arc on the surface. However, the results were not sufficient to observe it, mainly due to the difficulties mentioned in Sec. 6.4. Because the measurement is very elaborate and the experimental OBC spectrum does not exhibit any Fermi arcs, the measurement was not further improved on. It is, however, very unlikely to have observed the monodirectional pulse propagation even with a better experimental setup.

## 8 Measurement Simplification

To measure the voltage of a node, as mentioned in Sec. 5, one needs direct access to the board and be able to reach the conductor tracks. To be able to do this, one either spreads out the boards and connects the individual boards with long cables to maintain accessibility, or one reroutes the conductor tracks such that they are accessible even when the boards are stacked on top of each other. The former is simply not manageable since the boards would take too much space and the connection in z-direction would require 128 connections to the previous layer, as well as another 128 connections to the next layer. Thus, the rerouting approach was taken, where the nodes are now accessible at the sides using flat band ribbons.

Further, the BNC board is connected to these connections at the side, where one can now access each individual node. However, after each measured node one would need to manually move the BNC cable to the next node until all the 1024 nodes are measured for PBC. This way, a single PBC bandstructure measurement would take about two days and for OBC, minimum a week. Alternatively, one can use a multiplexer that switches between the nodes and can be controlled via software. We use an adapter board in order to connect the multiplexer to the flat band ribbon connectors at the sides. Installing these multiplexers allows for a PBC bandstructure to be measured in just two hours.

However, the effects of the flat band ribbons and the multiplexer boards on the results are not known. Hence, due to the unsatisfying results in the previous Sec., their influence is studied in the following Secs. in order to spot any possible error sources.

### 8.1 Flat Band Ribbons

To see the impact of the flat band ribbons one can compare the voltage measurements when measuring with the BNC board and measuring at the node directly. The former requires the connection to the flat band ribbons, while the later does not. The comparison for one node is shown in Fig. 40.

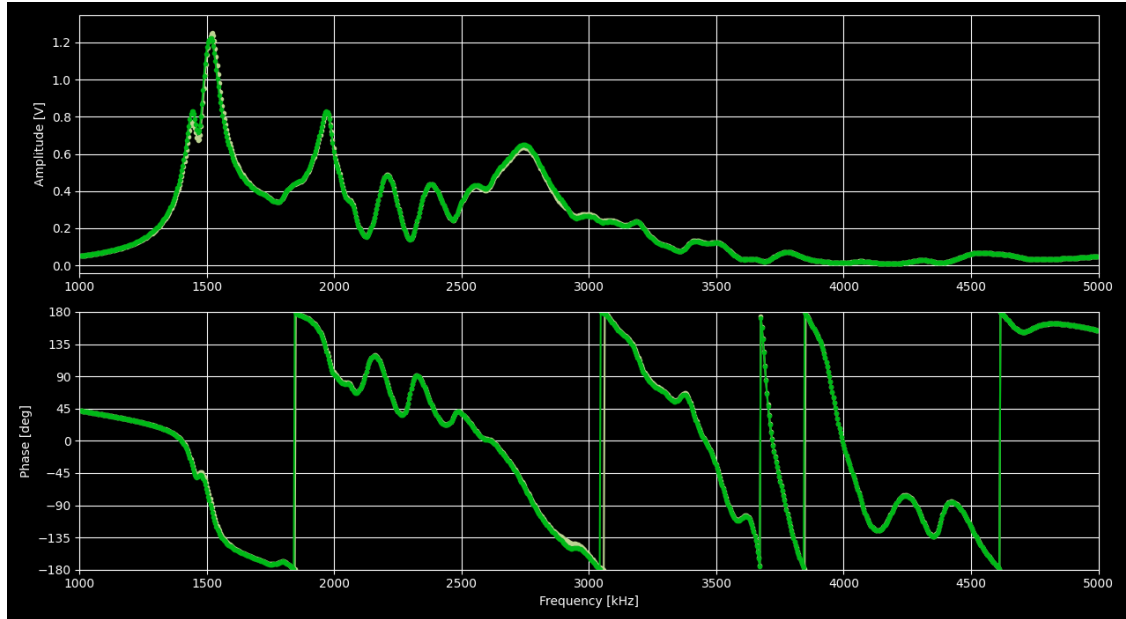


Figure 40: Frequency sweep of the same node done once using the BNC board (yellow) and once by directly measuring the voltage at the node (green).

As one can see, the two curves are almost identical and the frequencies at which they might differ a tiny bit are not of interest for the measurements. This is also observed for other nodes, which will not be shown for reasons of redundancy.

Due to limitations of the set-up, the input signal is fed in through the BNC board, therefore not eliminating the flat band ribbons entirely. However, since the source signal is the same for both measurements, differences in the measured signals are solely due to the flat band ribbons.

It is therefore easy to see that there are no drawbacks in the use of BNC boards or the flat band ribbons.

## 8.2 Multiplexer Measurements

In a similar fashion one can compare the effects of the multiplexer boards by comparing the results of multiplexer board measurements and BNC board measurements. However, the results are not as straight forward as in the previous Sec., because the multiplexers add many components to the system. Additionally, the multiplexer set-up was not available in Zurich, which makes the comparison of single node measurements difficult. That is why in this case it we compared how the averages and variances of the two types of set-ups behave. The results for the respective sublattices can be seen in Figs. 41 and 42.

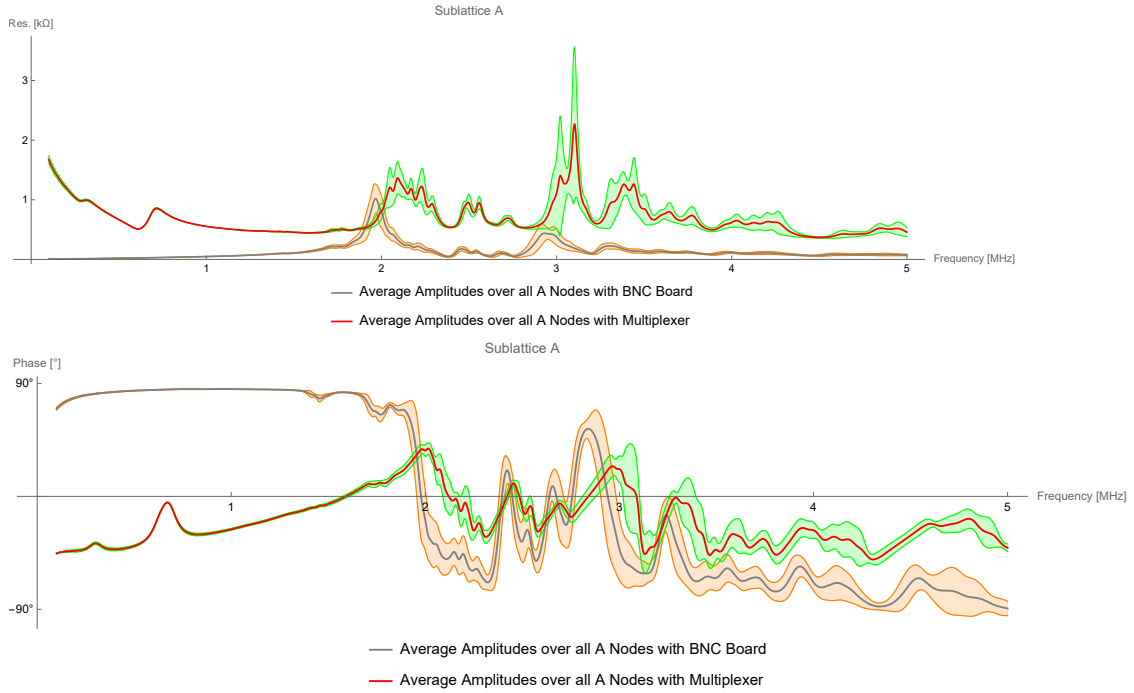


Figure 41: Averages and standard deviations of the impedance spectra’s absolute values (top) and phases (bottom) for all sublattice A nodes of the board measured once using the BNC boards (grey with orange error bar) and once using multiplexer boards (red with green error bar).

As one can see, both methods deliver quite different spectra. Looking at top of Fig. 41, the multiplexer impedance spectrum never goes to zero, seems to diverge as the frequency approaches 0 Hz and the peaks’ positions differ from the BNC measurement. However, there seems to be a correspondence between the peaks of both measurements, which seem to have shifted or gotten broader and deformed slightly. This is especially true in the vicinity of 2.5 MHz, which is the domain of interest, where the shape of both spectra seems to agree very well.

It was to be expected that the multiplexer board changes the spectrum, as the multiplexer itself is modelled by multiple RLC components. However, these components are always and only present between the measured node and the measurement device. Hence, such a constant load on the system should not influence any two nodes differently. This argument is supported by the fact that the base impedance of the multiplexer measurements is constantly higher across all frequencies or that the variance seems to be affected the same way as the averages.

This constant shift in the impedance has a simple background, which comes from the resistance that is added by the multiplexer board. As for the divergence when the frequency approaches 0, this is probably due to the multiplexer board acting dominantly as a capacitor at low frequencies. This would agree with the observation in the bottom of Fig. 41, where the phase seems to be trending towards  $-90^\circ$ , which would indicate capacitive behaviour.

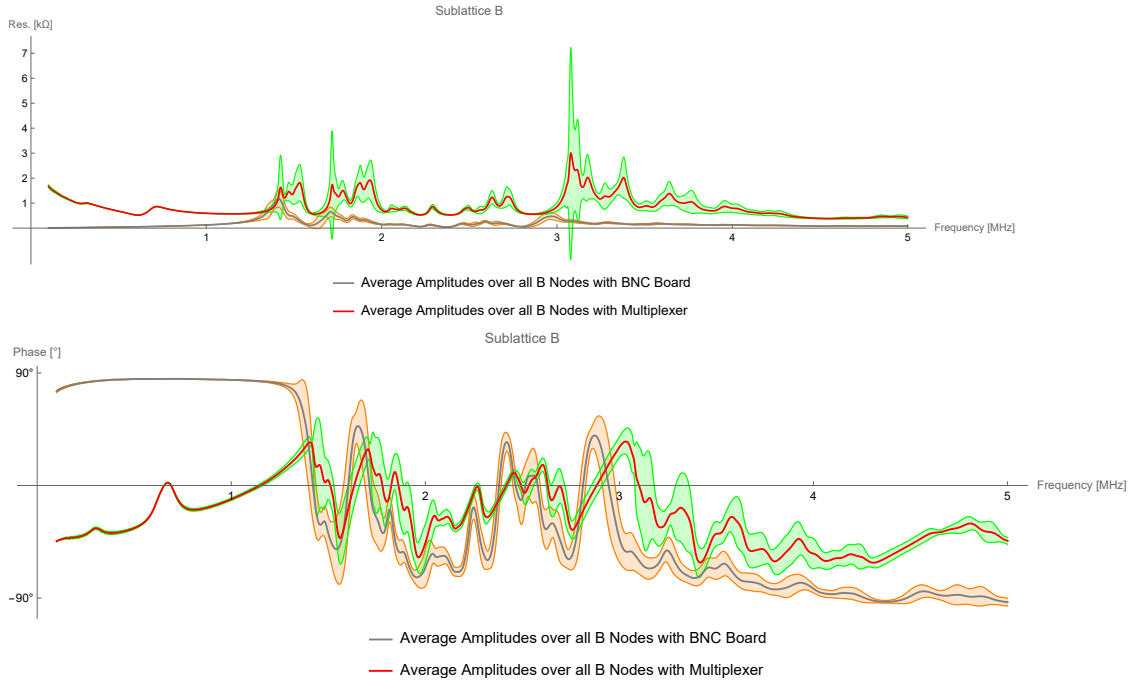


Figure 42: Averages and standard deviations of the impedance spectra’s absolute values and phases for all sublattice B nodes of the board measured with BNC and multiplexer boards.

The fact that the constant shift in the impedance and the low frequency behaviour seen in Fig. 42 match with that of Fig. 41 is another indication, that the multiplexer influence affects all nodes equally.

One troublesome observation, which is more pronounced in the B sublattice, is the increase in variance, which is especially noticeable in the peaks. This suggests that the multiplexer board amplifies deviations between nodes, which can be detrimental. However, the saving grace in this case is the fact that the spectra near 2.5 MHz seem to be almost exempt from the multiplexer’s influence, apart from the constant shift in resistance.

The multiplexer board seems to only amplify the spread in impedance, not actually cause it. Thus, it is unlikely to be the source of the inaccurate bandstructures and allows for their measurement in a reasonable time, which is a reasonable trade off in our opinion.

## 9 Disorder

In the search for the cause of the variance of the nodes' impedances, disorder is usually one of the first suspicions. However, it is quite difficult to understand its influence on the impedance spectra without dismantling, measuring and replacing the individual components. The components can be measured while still being on the board, however, in this case one cannot measure the isolated component due to the load of the whole circuit being connected to it. This leads to an interesting observation, namely that each component exhibits an effective value that corresponds to an average over the whole board. Thus, deviations in the components are difficult to spot unless isolated.

To better understand the effects of disorder, the system size was reduced to a single layer, which has the added benefit that it's quicker to measure. The board's bandstructure was then measured in order to get an idea of the gravity of the situation and to have a comparison later on. This was done using the BNC boards, since the multiplexer boards are only available in the laboratory of the Würzburg colleagues and these measurements were done in Zurich. The results are shown in Fig. 43.

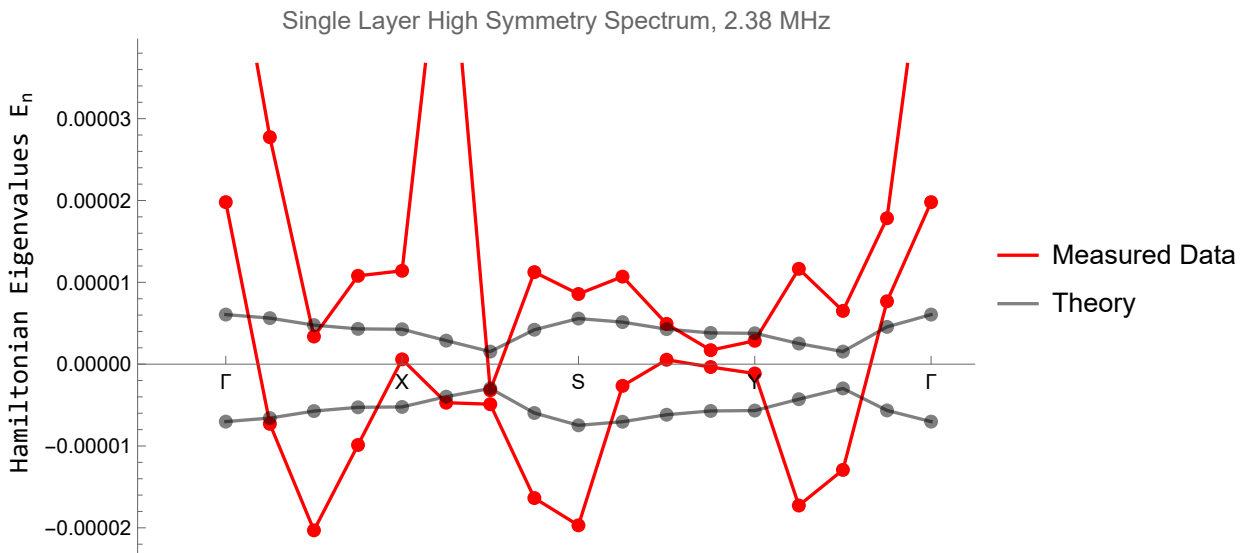


Figure 43: Measured bandstructure of a single layer and the simulated bandstructure of the same board. Since it's a single board, there is only one loop starting at  $\Gamma$  and no change in  $k_z$ . The theoretical bandstructure has been scaled by a factor of  $10^4$  to match the measurements.

The experiment did not seem to produce comparable data at all. On top of that, it is quite counter intuitive that simplifying the system yields worse and more chaotic results. However, this might be due to the averaging effect mentioned before, which would suppress deviations more for the 3D circuit board compared to a 2D single board. It is difficult to check if this is the case, but the layering is really the only thing that separates this bandstructure from that of Sec. 7.1.1. The almost complete lack of structure indicates a break down of the translational invariance of the nodes, which is an essential assumption for the evaluation of the bandstructure. This is the reason why the board was measured with only two different current inputs, one for each sublattice, and the Laplacian reconstructed as described in Sec. 3.1.2.

While a nice bandstructure is the final goal, it is not a good measure to further inquire about the disorder of the system. For this, it is much more useful to consider impedance spectra of the board and the nodes.

## 9.1 Component Deviations

Simulations of the impedance spectra would be a great help to understand the role of the components. Therefore, the next step was to adjust the parameters of the simulation to match the measurement as closely as possible. The comparison of the impedances with the simulation using the parameters of the circuit are shown in Fig. 44.

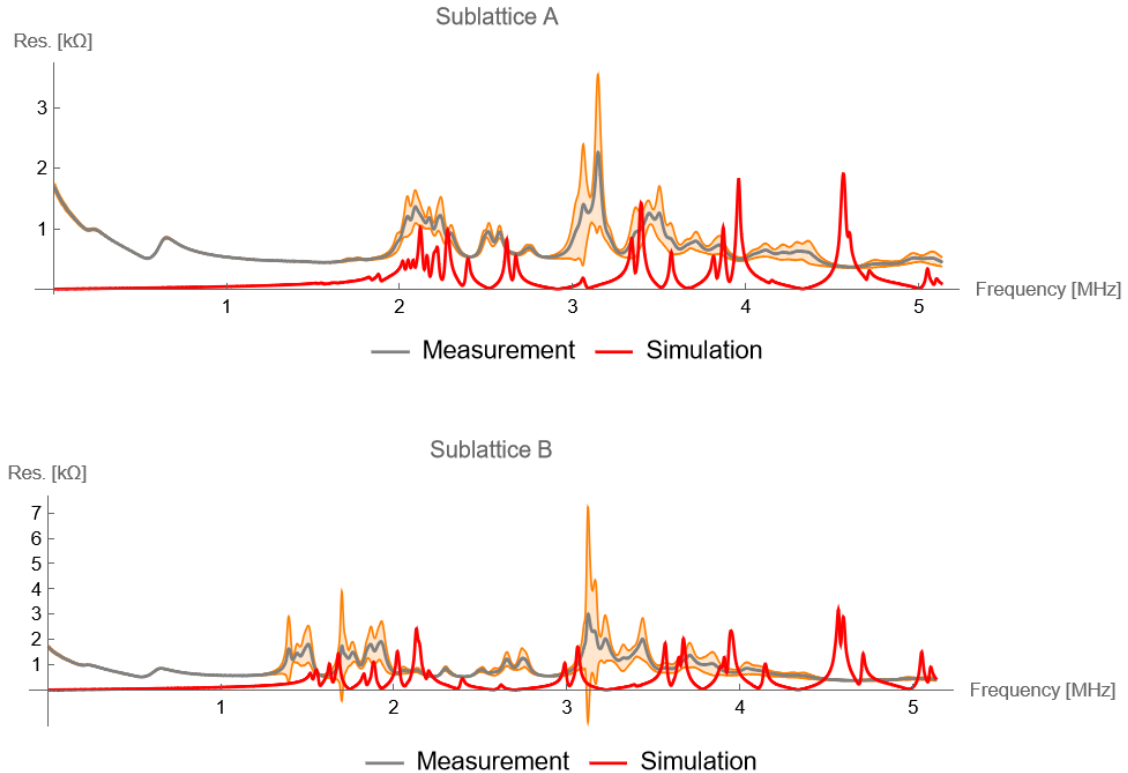


Figure 44: Comparison between the averages and standard deviations of a board's impedance measurement and the simulations of the same board. Since in theory all nodes of the same sublattice should behave the same, simulation is compared to the average rather than individual nodes. The data was measured using the multiplexer boards, as it was the only available result at the time.

The approach to simulate disorder was to sample each component from a Gaussian as described in Sec. 3.2, as well as changing the means and standard deviations of the Gaussians in order to account for components that might be worse than expected. Another problem one encounters is the fact that due to disorder, all the nodes have different impedance spectra, even if the differences are minimal. Previously, all the nodes of the same sublattice were identical due to translation symmetry, which is now broken by disorder. Hence, it is not a time-effective method to find error sources by tuning parameters, as the sheer amount of possibilities is too large.

During the construction of the circuit boards there had been one set of components that were troublesome, the coils connecting the B sublattice to ground, which corresponds to the  $L_{0,B}$  component in Fig. 22. Some components were mislabeled and therefore displayed inductances 10 times the desired value. These were replaced, however, were the next point of focus due to past problems.

To check for this plausibility, simulations were run where some coil values had been increased to 10 times their initial value and compared to the measured impedance spectra of the board. Surprisingly, the simulation where a good match as can be seen in Fig. 45.

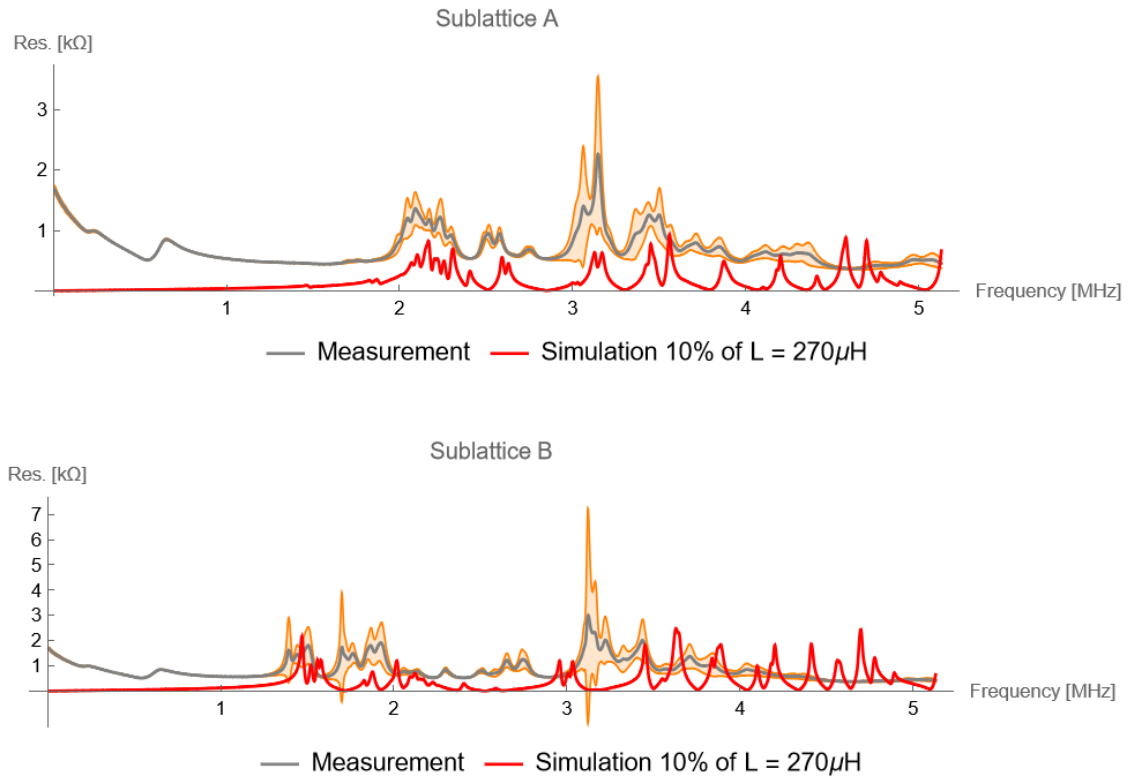


Figure 45: Comparison between the averages and standard deviations of a board's impedance measurement and the simulations of the same board, but 10% of the  $L_{0,B}$  coil connecting the B sublattice to ground have been replaced by a coil with 10 times the value.

However, this agreement has to be taken with a grain of salt. Should there still be coils left whose values are one whole magnitude larger, this would have been measurable locally by a LCR meter, even if the coils are still built in to the board. Smaller deviations in the coils' inductances on the other hand are harder to detect without removing the component from the circuit. This is due to the fact that a built in component is connected to the whole circuit and therefore the measured quantity can deviate from the manufacturer's specified value. Thus, measuring built in components measures an averaged value of the equivalent circuit including all the other components that are connected. Only strong deviations are not overshadowed by this averaging and therefore detectable without isolating the component. Therefore, the more realistic interpretation would be that a substantial amount of the coils have higher values than expected, which stems from a large variance in the components.

With this, the next step was to replace some of the above mentioned coils and observe how it affects the behaviour of the nodes. For this, the information obtained from averages of the sublattices like in Fig. 45 are not very useful, as they yield no information about the local behaviour of a node. Instead, they are useful to determine well suited frequencies with low variance. The criteria in this case was to find the frequency with minimal, added relative variance of both sublattices in the vicinity of 2.5 MHz, as described in Sec. 6.2. A frequency of 2.38 MHz with an added relative variance of 0.7 fulfilled this criterion. For this purpose, newly made single layer measurements with the BNC boards were used, since, as discussed in Sec. 8.2, these can lead to undesired influences, which were to be eliminated.

The nodes are then plotted as histograms, where the height corresponds to the absolute deviation of the impedance from the mean of the sublattice nodes at 2.38 MHz, as can be seen in Fig. 46.

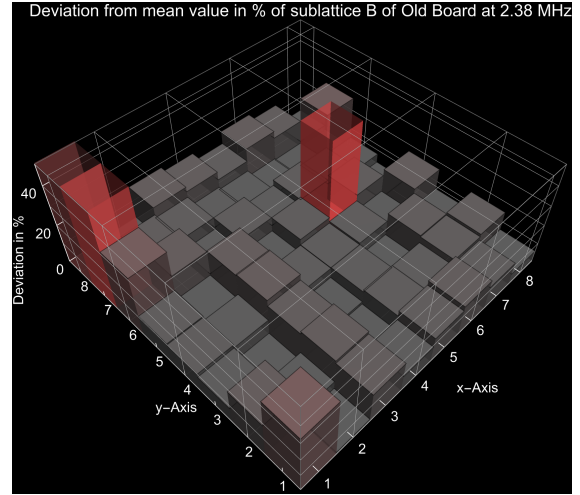
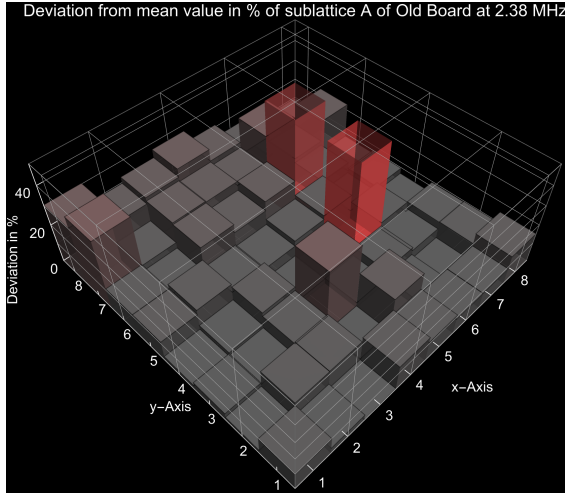


Figure 46: Histogram representation of the deviation from the mean of the nodes of a single board. The plots show the absolute value of the deviation and the scale is cut-off at 50% of the mean value.

Most nodes show considerable deviations, which hover around 10%, while some nodes have extreme deviations reaching over 50%. The sublattices' nodes seem to vary independently, except for the nodes (1,7) and (1,8) in the left corners of Fig. 46. This could indicate that the deviating components of the unit cells are only directly connected to one of the sublattices, therefore influencing them differently. It could also be the case that the responsible components affect the two sublattices differently independent of their location. Exploring all these possibilities is an interesting future endeavor, however, we focused on the effects of exchanging the  $L_{0,B}$  coils. The chosen unit cells were (1,7) and (1,8) since they show high deviations in both sublattices.

Upon dismantling and measuring the coils, they exhibited values which differed by 2-3% from the nominal value, while the tolerance specified by the manufacturer was 1%. This is quite a substantial mismatch, which is why new coils have been built in with values within the 1% tolerance range. The resulting impedance measurements can be seen in Fig. 47.

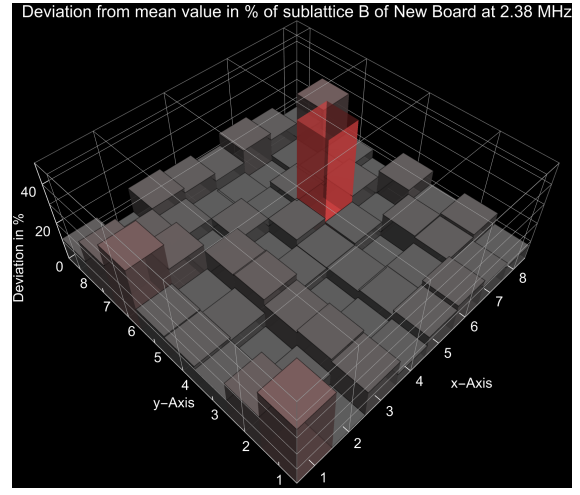
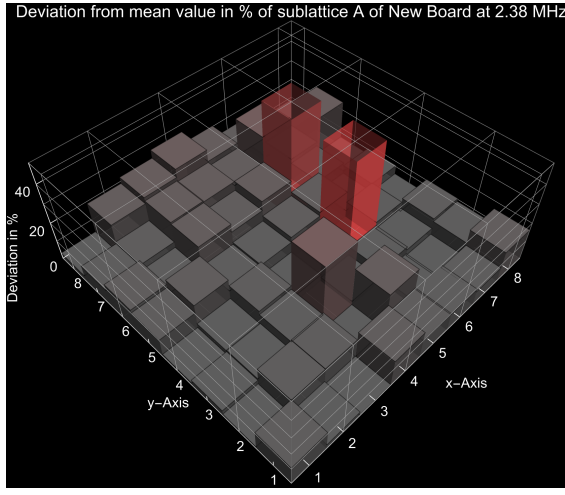


Figure 47: Histogram of the deviation from the mean of the nodes of the single board where the (1,7) and (1,8)  $L_{0,B}$  coils have been replaced.

The (1,7) and (1,8) unit cells now show much smaller deviation from the means, which led to the assumption that this approach could help to restore a good degree of translational invariance.

Hence, more unit cells'  $L_{0,B}$  coils were replaced, where no threshold was defined and the worst cells were estimated by eye. Additionally, the measured voltages from the left of Fig. 43 were compared with simulated voltage values in order to find further possible candidates. A portion of the further replaced coils exhibited deviations outside of the specified tolerance as well, however, even if the tolerances were inside the norm, the coils were replaced by new ones. The new board's impedance spectra were measured again, which revealed a surprising development that was not noticed before, namely that replacing these coils leads to a shift in frequency in the spectra as seen in Fig. 48.

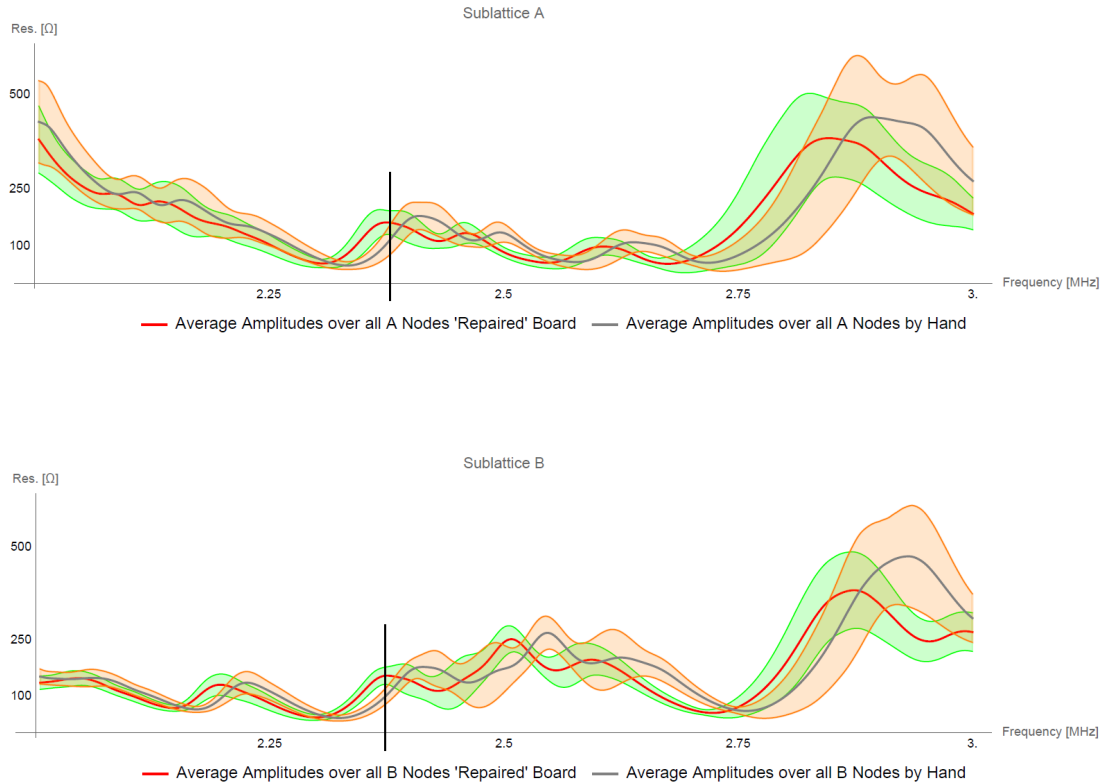


Figure 48: Shift of board impedance spectra due to the replacement of the  $L_{0,B}$  coils (red with green error bar) compared to old device setting (grey with orange error bar). The black bar indicates the former best suited frequency of 2.38 MHz and the frequency range was restricted to make the shift more visible.

Since now a good portion of the coils have been replaced, this shift of the individual nodes' impedance spectra is collectively significant enough to influence the whole board. Now the frequency with minimal, added relative variance of both sublattices has shifted to 2.35 MHz with 0.4 added relative variance. With this new knowledge, the observation seen in Fig. 47 is even more surprising, as Fig. 48 suggests a higher impedance at 2.38 MHz, indicated by the black vertical bar, after replacing the coil. However, just from the single cell spectra this could not have been anticipated, as can be seen in Figs. 49 and 50.

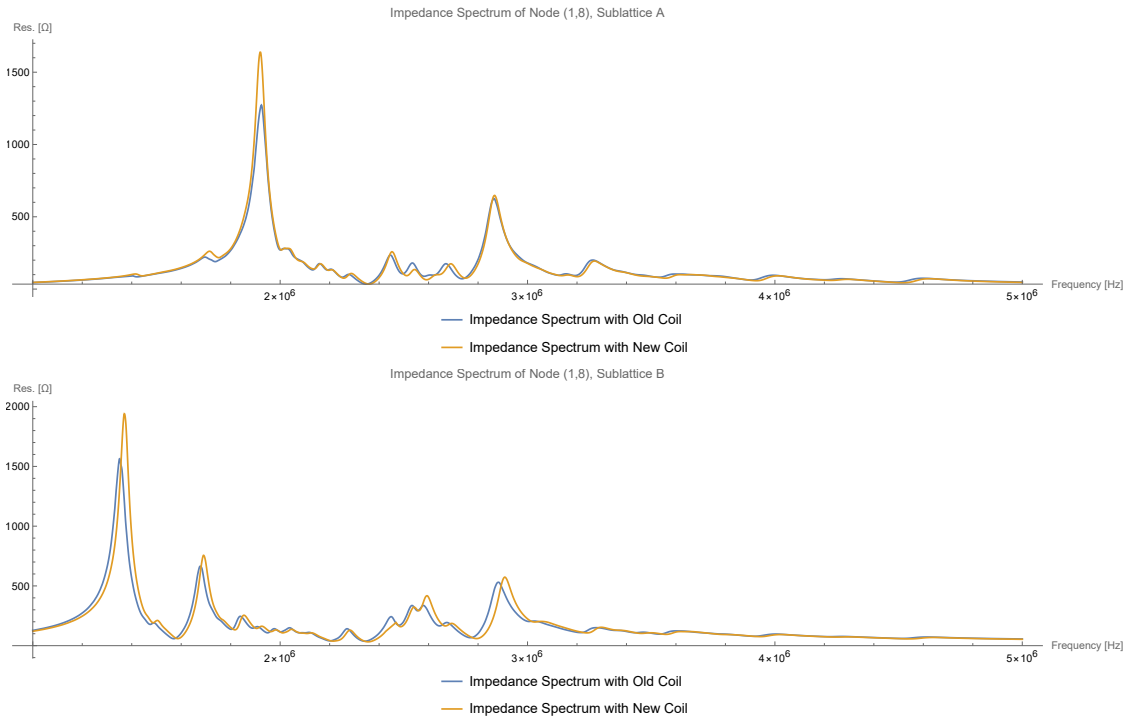


Figure 49: Comparison of impedance spectra of node (1,7) before (blue) and after (orange) replacing the  $L_{0,B}$  coil.

The sublattice A of the node (1,7) shows just a little shift near 2.6 MHz, as well as some changes in the peaks' amplitudes. The B sublattice on the other hand exhibits a shift towards higher frequencies and shows a similar behaviour at the peaks near the 2.6 MHz mark.

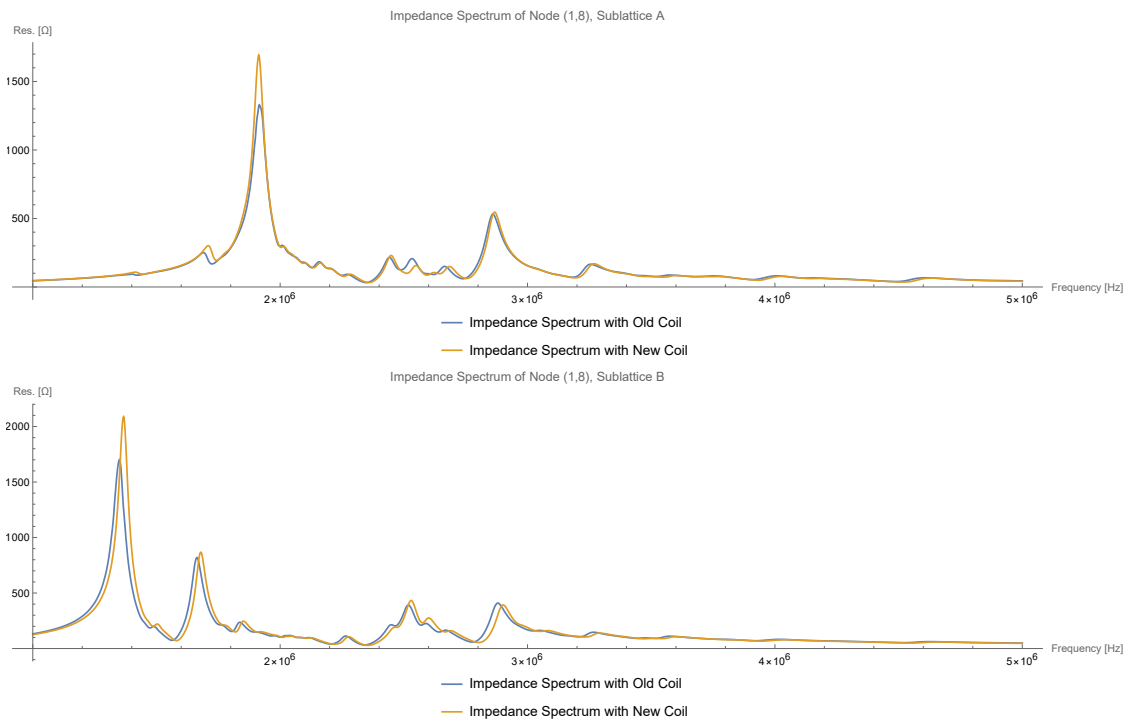


Figure 50: Comparison of impedance spectra of node (1,8) before and after replacing the  $L_{0,B}$  coil.

The (1,8) node displays almost the exact same behaviour as the (1,7) node, which is a slight shift towards the right. Comparing this with the collective behaviour seen in Fig. 48, one can see that on average the shift has happened towards the left, so exactly the opposite. However, since this is only a single example, it is not statistically relevant and was not further studied.

Because of this shift in the spectrum it makes more sense to see how the now coil replaced board's impedance spectra behave at 2.35 MHz, which is the new frequency with minimal, added relative variance. The new setting shown in Fig. 51 is then compared to the old board in Fig. 46.

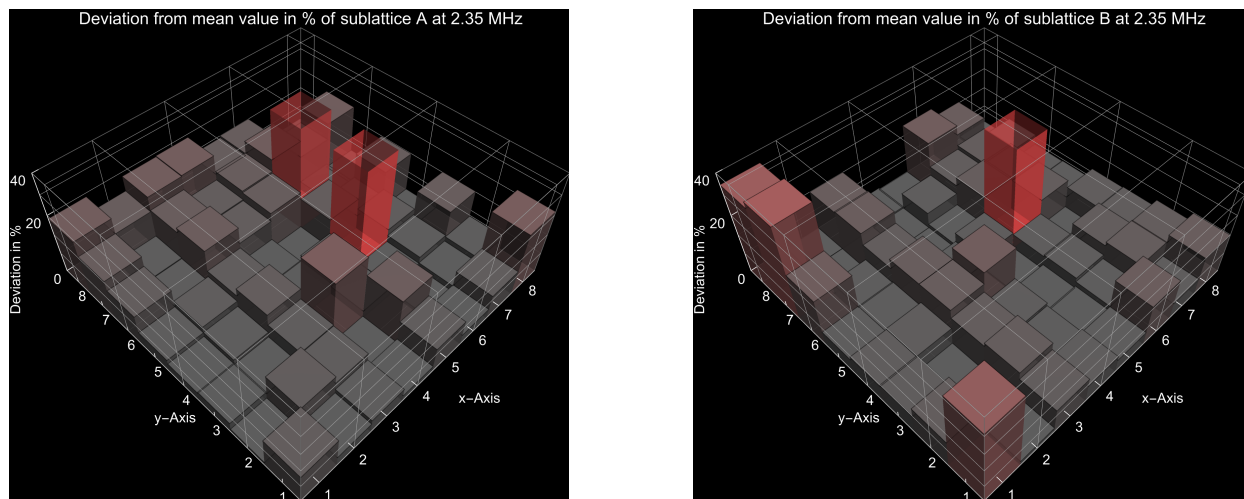


Figure 51: Histogram of the deviation from the mean of the nodes for the new single board, where a significant portion of the  $L_{0,B}$  coils have been replaced. Plot is shown for a frequency of 2.35 MHz which corresponds to the new ideal frequency.

Fig. 51 could be mistaken for Fig. 46 because they look so similar, meaning that exchanging those coils simply shifted the ideal frequency, but left the variance of the nodes nearly unchanged. Especially the nodes (1,1), (1,7), (1,8), (6,4), (6,5) and (6,6) are very reminiscent of the board without any swapped coils. However, as mentioned above, the minimal, added relative variance at the ideal frequency has decreased from 0.7 to 0.4.

To finish the analysis of the influence of the suspected  $L_{0,B}$  coils, the bandstructure was measured anew, this time at a frequency of 2.35 MHz.

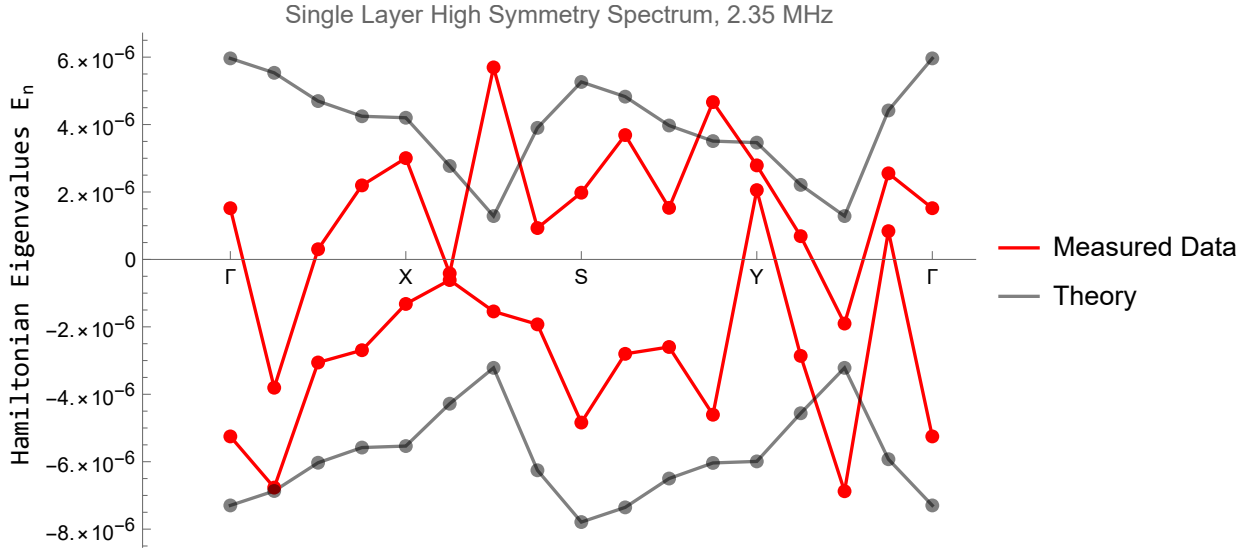


Figure 52: Measured bandstructure of the new single layer after the replacement of the  $L_{0,B}$  coils and the simulated bandstructure. The theoretical bandstructure has been scaled by a factor of  $10^4$  to match the measurements.

As expected, the new board does not yield the desired bandstructure yet, however, there seems to be at least more structure. This suggests some degree of periodicity under the assumption of translational invariance needed for the evaluation. Though it is hard to tell if the bandstructure is becoming progressively more similar to the theoretical one, as the features seem to emerge at random positions.

The results are rather disappointing after such a long and tedious attempt to reduce disorder in a single type of component. It is thus clear that repeating these procedures for other components is just not feasible and it would simply be quicker to replace all components with previously measured ones. This is also an important lesson, in the future, one should do the assembly of the boards in house and characterise the components during the process.

## 9.2 Current Stabilization

In an attempt to reduce the effects of disorder, the input current, as described in Sec. 6, was kept constant during a bandstructure measurement using a feedback loop. The approach was justified, since the circuit board is operated in the linear regime of Ohm's law. A comparison of the same measurement between a non current stabilized and a current stabilized bandstructure is shown in Fig. 53.

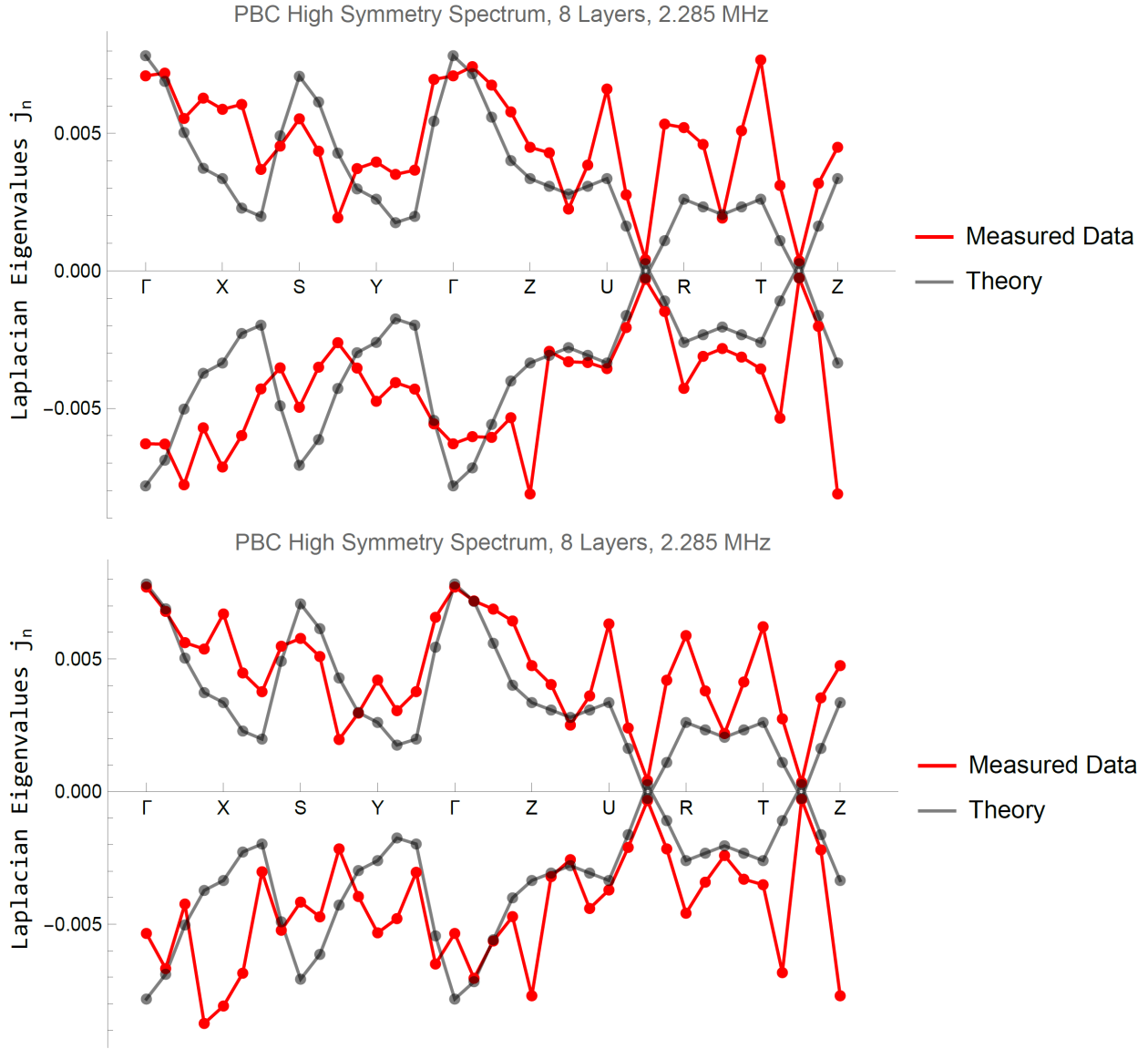


Figure 53: Comparison of the same bandstructure once measured without current stabilization (top) and once with current stabilization (bottom).

As can be seen, the difference is minimal and there seems to be no improvement or worsening with respect to the theoretical bandstructure. This was to be expected, since the Laplacian, from which the bandstructure is extracted, is independent of the current. However, this approach helps to make the measurement results more stable and reproducible, which was especially useful when using the multiplexer boards.

The stabilization of the current requires additional lock-ins, which were not available in the later part of this thesis, where the measurements were done using the BNC boards and not the multiplexer boards.

## 10 Layout Influence

Lastly, due to the fact that the methods in Sec. 9 showed little to no effect, the underlying problem could be the layout of the boards. Specifically, the conductor paths could influence each other and thus alter the measurements.

The individual boards are only a few millimeters thick and all the layers have to be accommodated into this space, which are a total of 6 layers, 3 with considerable conductive track lengths. Even though there are some additional insulating layers to prevent such influences, the continuous failed attempts at improving the boards performance lead to grasping at straws. It was also not a straight forward decision to pursue this path, as it requires the unit cells to be isolated in order to check for conductor path induced signals. This means that all the connections have to be destroyed, which is not reversible and therefore makes the board unusable for future bandstructure measurements.

There is only one layer that is directly accessible from outside, namely the measurement layer seen in Fig. 54.

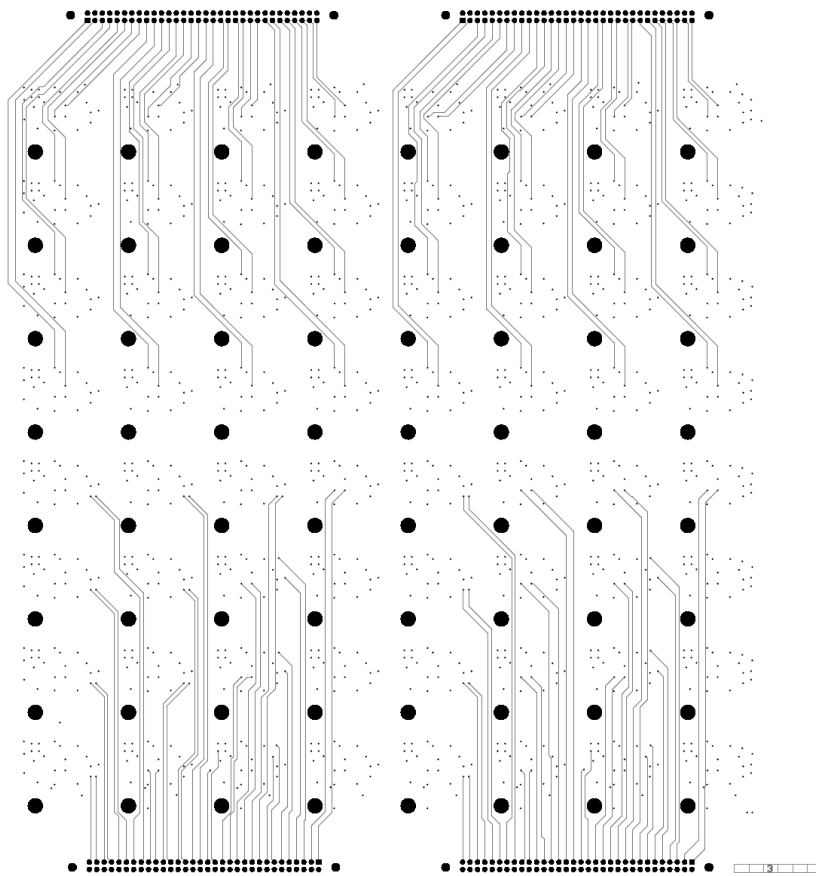


Figure 54: Board Layout of the measurement layer showing the measurement tracks from the nodes to the flat ribbon connectors.

In the ideal case, each conducting track has the same potential as the nodes they are connected to, however, the conducting tracks are not directly accessible as they are inside the board, and therefore the voltages at the two points cannot be compared to each other. Though, the comparison between BNC board and direct measurements discussed in Sec. 8.1 suggests that the potential across the conducting track is equal to that of the node itself. This also means, however, that the direct measurements alone do not suffice to check for induction influences of the conductor tracks.

The only way to verify this is to isolate the cells and only allow for communication between cells via induction. However, the measurement layer's tracks are not the only possible tracks that could act as antennas, there still are the PBC condition layers that could induce signals. The layout of the layers can be seen in Fig. 55.

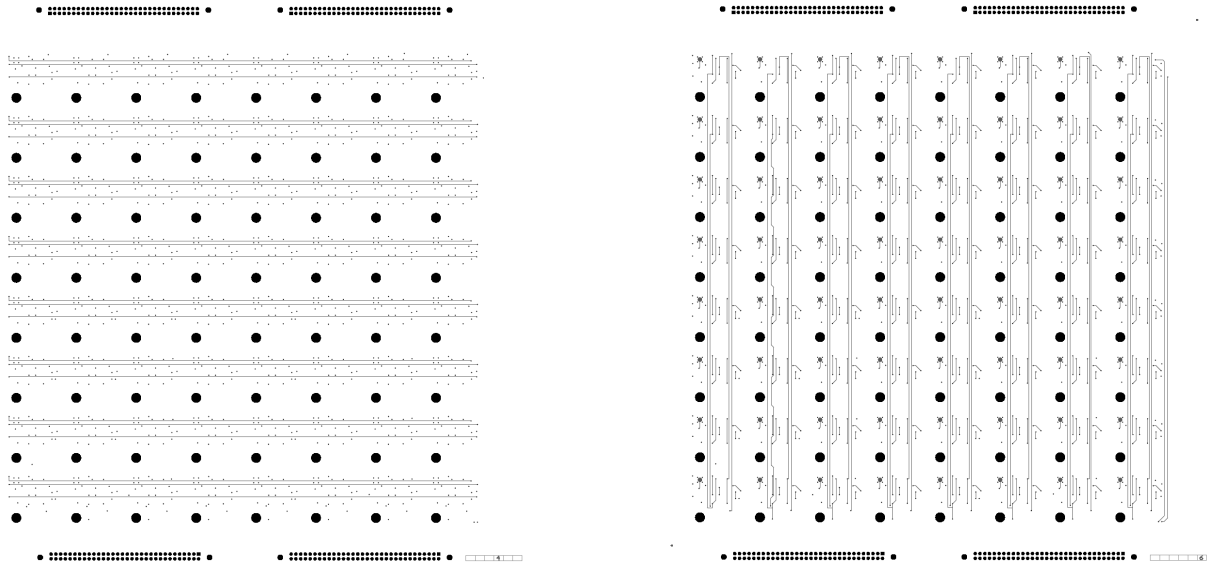


Figure 55: Layout of the PBC tracks in the x-direction (left) and y-direction (right) of a single layer.

These two layers are separated from the measurement layer by an insulating layer to block outgoing signals from each other, though it is not clear how effective this isolation is. The difference between these two layers and the measurement layer is the fact that they connect two edge unit cells with each other and due to the inaccessibility of these layers, the connection is permanent. This causes a restriction to the unit cells that can be isolated.

The approach is now to isolate a selected number of unit cells in a smart way, as illustrated in Fig. 56, in order to test for any kind induction.

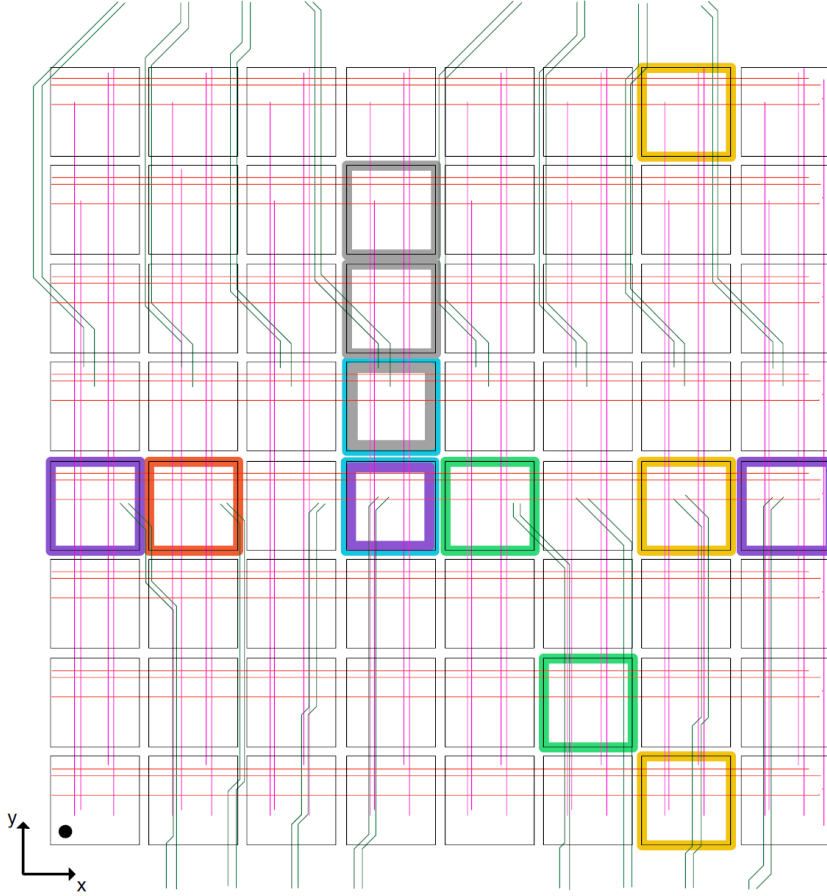


Figure 56: Illustration of the isolated unit cells (colored squares) with the single board tracks shown for orientation. The pink, vertical lines are the PBC connections in the y-direction, the red, horizontal lines are the PBC connections in the x-direction and the green lines are the measurement tracks of the two middle rows. The tracks are not true to size, nor are they complete and are only included to better understand the choice of unit cells.

The purpose of the different scenarios are summarized in Table 8:

Table 8: Correspondence between the color of the nodes in Fig. 56 and the type of induction one aims to measure.

| Color  | Type of Induction  |
|--------|--|
| Orange | PBC tracks have same orientation as measuring tracks: Induction between measurement tracks and y-direction PBC tracks                            |
| Violet | PBC tracks have perpendicular orientation as measuring tracks: Induction between measurement tracks and x-direction PBC tracks                   |
| Green  | Measurement track runs beneath another cell: Induction between measurement tracks and components of another unit cell                            |
| Blue   | Two unit cells are next to each other: Induction between components of two unit cells  |
| Red    | Unit cell is isolated and sublattices are decoupled: Induction between the measurement tracks of the different sublattices of the same unit cell |
| Grey   | Multiple measurement tracks run close to each other: Induction between measurement tracks of different unit cells                                |

Each scenario was tested separately in order to isolate the effects, however, one should bear in mind that in a bandstructure measurement they are all present at once and it is not clear how the interplay affects the measurement.

Most scenarios did not show a significant response, with maximum induced voltage amplitudes that are less than 1% of the input signal and will therefore not be shown. However, some responses reached surprisingly high amplitudes which include the orange, grey and red scenarios described in Table 8.

The first scenario of study is the orange case. The PBC tracks running in parallel orientation underneath the measuring tracks showed, as expected from classical electrodynamics, a larger response than the perpendicular orientation. The perpendicular setup showed little to no response, while in the parallel case the peak amplitude reached about 1.5% of the source amplitude, as shown in Fig. 57.

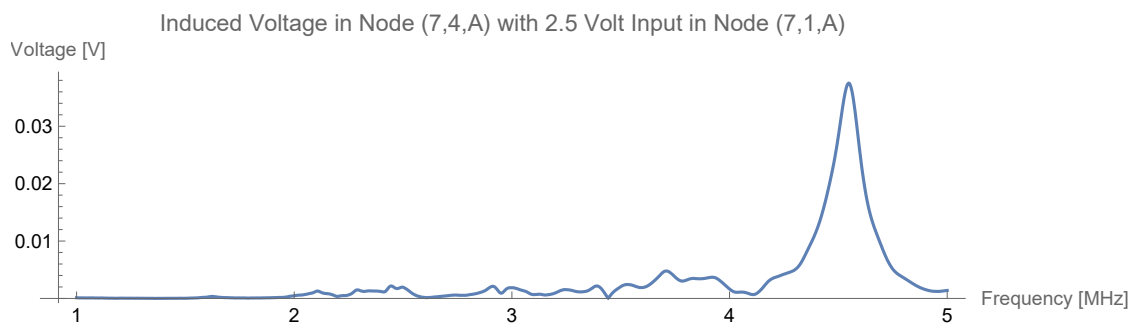


Figure 57: Induced voltage amplitude as a function of frequency from the PBC tracks running parallel to the measuring tracks. Input in cell (7,1) and measurement in cell (7,4) occur in the sublattice A.

The signal shows a clear resonance behaviour, which was generally the case for all scenarios regardless of the responses' strength, however, the frequency range of the resonance lies outside of the range of frequencies used for the bandstructure measurements. Though it is not clear where this resonance frequency moves to in the case of a fully connected board, which is why an influence on the bandstructure measurements cannot be ruled out.

Fig. 57 showed the induction when the input and measurement are both done on the sublattice A, however, the response for the BB, AB or BA cases seems to be much lower. This could indicate a very strong positional dependence in the x-direction, where the PBC connection and the measuring track for the A sublattice overlap quite well, while being further apart for the B sublattice.

The second case of relevancy is that of three consecutive unit cells whose measurement tracks run close to each other, which corresponds to the grey cells in Fig. 56. This measurement inputs the signal in node (4,5) and measures the induced signals in the nodes (4,6) and (4,7), then inputs the signal in node (4,6) and measures the voltage in (4,7). The strongest response, as shown in Fig. 58, was observed in the former case in the (4,6,A) node.

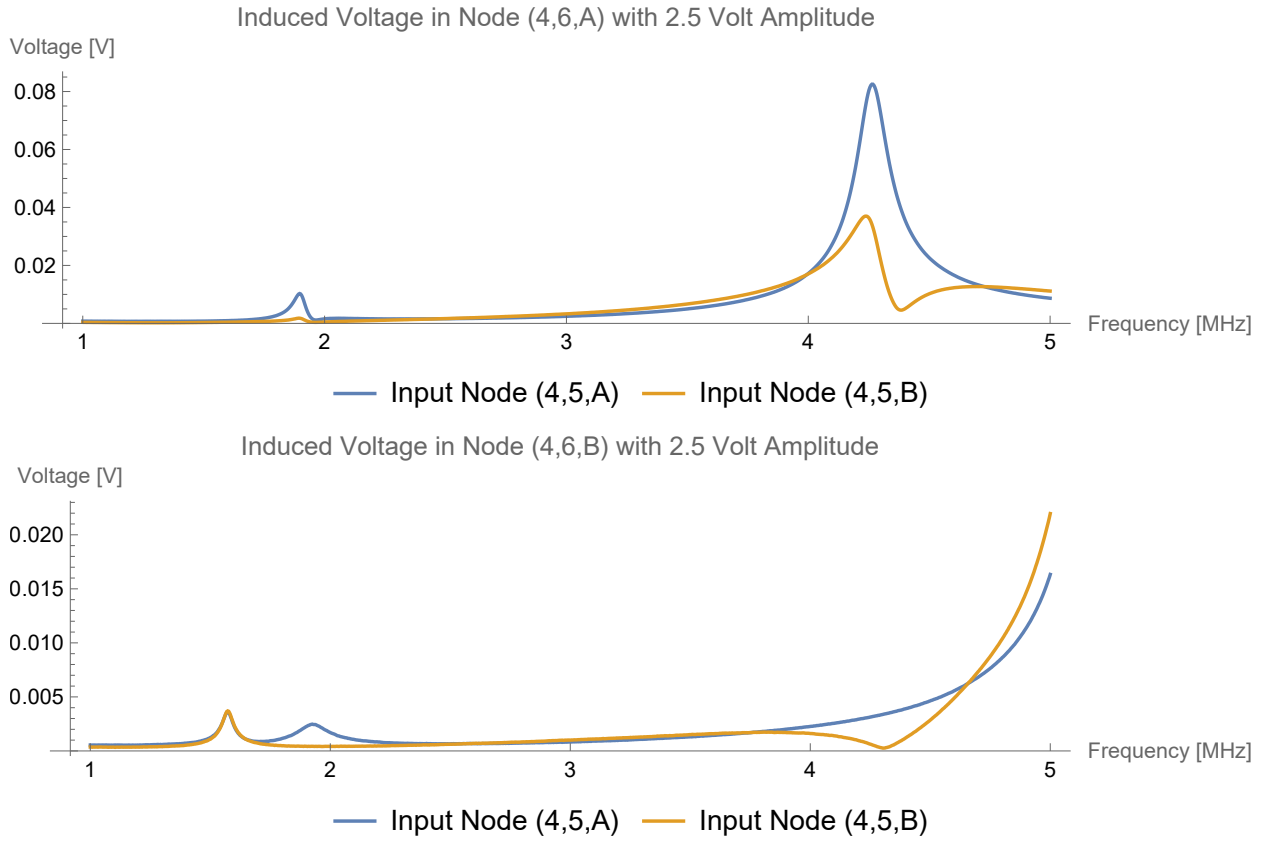


Figure 58: Induced voltages in the Nodes (4,6,A) (top) and (4,6,B) (bottom) from the multiple measurement tracks that run close together. Input Nodes are (4,5,A) and (4,5,B).

The peak voltage of the stronger signal is around 3% of the input signal's and the resonance frequency is as well in the 4 MHz range. A weaker response, with a peak voltage of approx. 1.5%, was observed when the input was changed to the (4,5,B) node. The two resonance curves look very similar and have almost identical resonance frequencies, the only difference being the magnitudes of the measured voltages. A similar behaviour can be observed in the node (4,6,B), however, the signals seem to peak above 5 MHz. It is unclear if and how the resonances shift in the non-isolated case. Therefore, the resonances could still be at different frequencies when fully connected and therefore influence the sublattices differently. This is consistent with the previous observation above.

The induced signals in the (4,7) node are at least one magnitude lower and are therefore not shown. The absence of induction in the (4,7) node could be explained by the fact that the (4,6)'s measurement tracks run in between and therefore, the distance would be too great to induce a signal. However, putting the signal in node (4,6) and measuring in node (4,7) should yield similar results, since the track layout between (4,6) and (4,7) is similar to that between (4,5) and (4,6), with the exception of the length of the tracks that run parallel. But the results show responses that are at least one order of magnitude lower as well. A similar scenario, the blue cells in Fig. 56, checked for induction due to unit cell proximity. The difference here is the fact that there are no parallel segments of measurement tracks and the measurements showed no significant results either. This suggests that the proximity of the cells is irrelevant and that the length of parallel running tracks is one of the most important factors.

Another idea was thus to check whether there is some sort of correlation between the impedance spectra in the connected versus the isolated cases as a function of track length. The results of the sublattice A of this analysis is shown in Fig. 59.

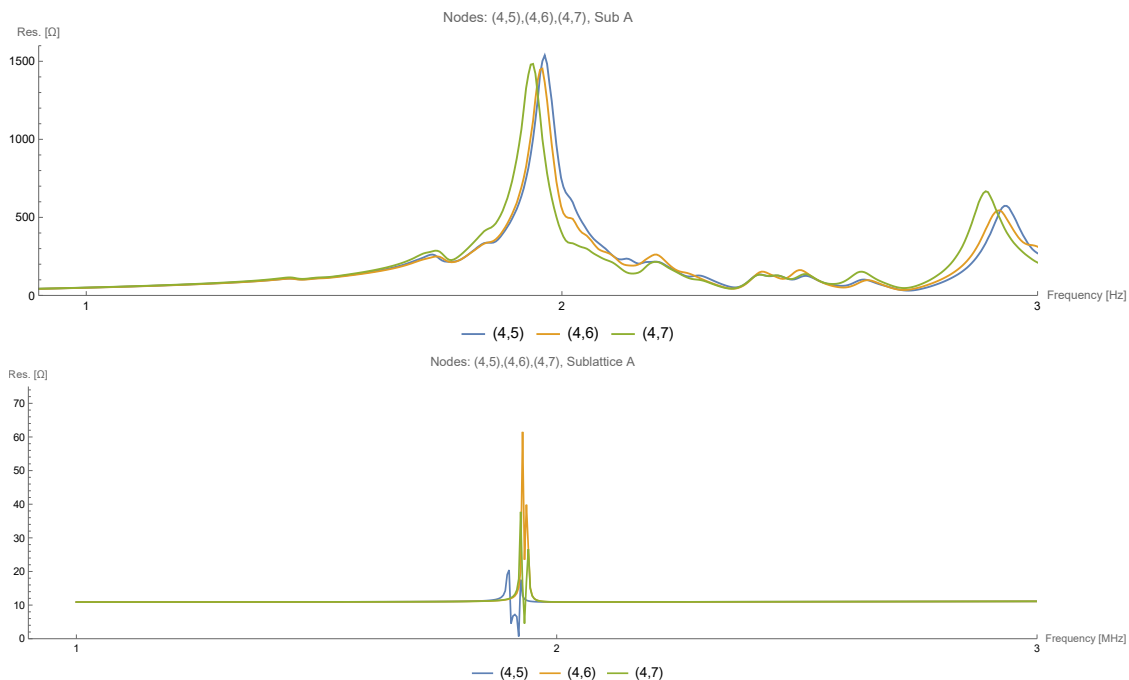


Figure 59: Comparison of the individual (4,5),(4,6) and (4,7) node's impedance spectra while connected (top) versus isolated (bottom). The data shown is only from the sublattice A.

As one can see in the upper part, the shift of the impedance spectra shifts to the left as the tracks become shorter from (4,5), having the longest tracks, to (4,7), having the shortest tracks. However, this is not reflected in the case of the isolated unit cells and suggests no such connection between deviation and induction due to track length either. This is strong evidence that induction is indeed one of the leading causes for the shifts in the spectra, especially when long, parallel running tracks are present.

The most extreme case of inductance was observed in conducting tracks of different sublattices of the same unit cell. This corresponds to the red cell marked in Fig. 56 and requires to remove the connection between the two sublattices in addition to isolating the unit cell, which consisted of dismantling a single capacitor. The induced signal in the sublattice B is shown in Fig. 60, with a maximum voltage amplitude of about 3% of the input signal.

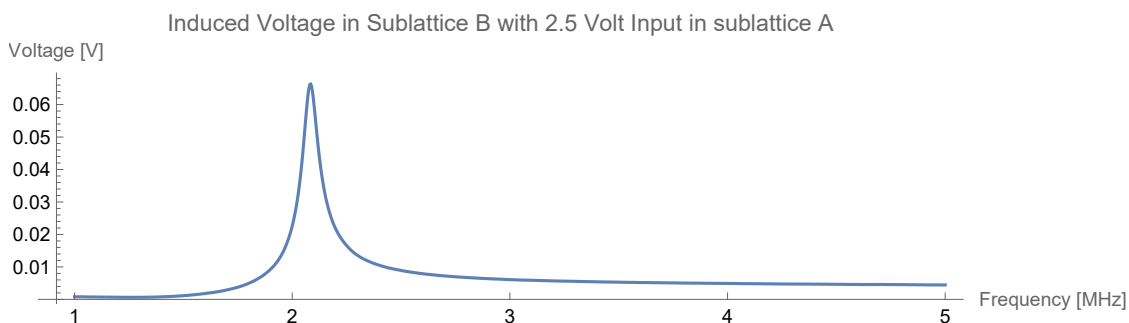


Figure 60: Induced voltage from the sublattice measurement track proximity. Here, the induction from the A sublattice on the B sublattice is shown.

In the B sublattice the resonance lies near 2 MHz, which could very well play a role in the band-structure measurements. The reversed case shows an even higher peak of around 5% of the input signal and can be seen in Fig. 61.

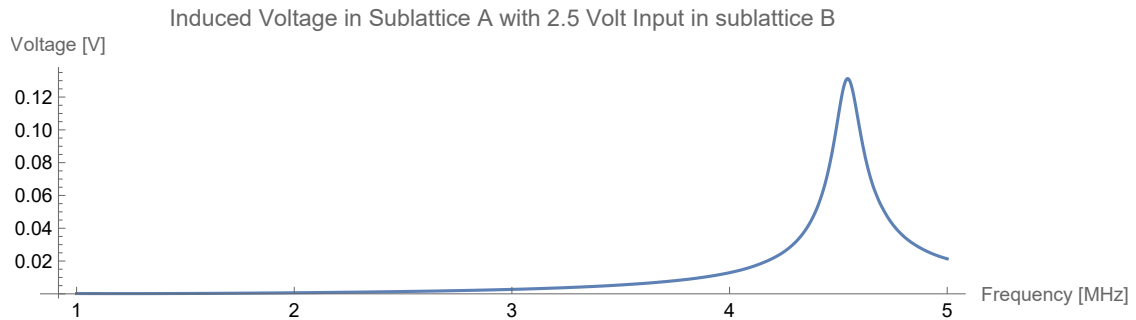


Figure 61: Induced voltage of the B sublattice on the A sublattice.

This scenario showed by far the largest response, which is to expect if the most important criteria is the distance. However, the asymmetry shown between Figs. 60 and 61 could help to understand the problems encountered above, as the conducting tracks of the A sublattice seem to get influenced more strongly than the B sublattice. This is further supported by that fact that the strongest responses always involve the A sublattice and that the resonances seen in the Figs. 58 and 58 are located close to 4 MHz as well.

The experiments have shown that there is significant induction on the measurement layer for the case of isolated cells, though the effects on the bandstructure measurements are still unexplored. It does not seem to affect all unit cells and the two sublattices equally, whereby the largest contribution seems to come from the length of parallel running tracks. It is therefore safe to assume that the board layout leads to positional dependent influences of the signals, which may very well be the reason for the unsatisfactory results encountered above.

## Part V

# Conclusion

In conclusion, this thesis has investigated the modelling of a WSM using a classical RLC circuit board. The experiments have shown that the produced bandstructures and therefrom derived quantities like the Chern number or Fermi arc can indeed be identified with that of a quantum mechanical system, the WSM. However, they also showed a level of disorder that is too high to achieve satisfying results under OBC. This led to strong deviations from the expected bandstructure, or even seemingly random features.

Thus, after attempting to improve the performance of the ETI, such as adjusting the frequency and removing the most varying single boards, it was decided to focus on the behaviour of the individual boards in order to find the cause for this misbehaviour. This thesis, therefore, aimed at understanding the origin of the observed misbehavior, by systematically analyzing possible causes.

The possible influences on the results due to component deviations and the board layout were identified as the key aspects. Regarding the former, even for a single board the system complexity was too great to cover for all the possibilities in the limited time that was available. Therefore, the focus was set on one type of coil specifically. The coil replacements did not change the system's behaviour very much, indicating that the coils were probably not the cause. Analysis of the replaced coils' specifications indicates that the variance is comparable to the values provided by the manufacturer. This makes it unlikely that the other components' disorder is to blame.

Systematically isolating different unit cells on one of the boards led to the conclusion that the fault was with the layout. Conducting tracks that run parallel over a significant distance and in close proximity induce currents that distort the signals. Since this effect depends on the position of the unit cell on the board, the influence varies and the translational symmetry is broken.

This does not mean that the data collected is of no use, rather, the insights gained from these experiments highlighted the fact, that the system's real and expected behaviour differ even on the most basic level. It is therefore imperial for future projects to begin the characterization of the circuit at an early stage. Then, one could gradually increase the system complexity should the results agree with the expected behaviour, which are obtained from tight-binding model and RLC board simulations.

Given the successful creation of a topological WSM, one can study trivial and non-trivial NH systems. In the present case, the design limitations of the employed circuit prohibited a progression towards these intricate phases.

It would have been very interesting to observe the trivial NH phase, as well as the anomalous surface states inside the point gap for the non-trivial case. The point gap spectrum is guaranteed for a WSM precursor and one can compute the corresponding 3D winding number that indicates the topological phase. The surface states are the manifestation of the Fermi arc in the NH system in the form of an anomalous single sheet of complex eigenvalues per surface. In our case, due to time-inversion symmetry, the number of Weyl points and Fermi arcs are doubled, yielding two sheets per surface. Such surface states could not be realized in purely 2D systems, as the Fermi arcs would appear as open contours. In 3D, such open contours can be connected via the bulk, e.g. a WSM, restoring the closed Fermi surface.

Even though this project did not get as far as initially anticipated, the educational value was still immense. Should this project be continued, either by repairing or completely rebuilding the ETI circuit, there is already a good foundation of knowledge and data processing, which will certainly lead to a successful result.

The exploration of non-Hermitian systems and metamaterials have ushered in a new era of possibilities in science. These developments have the potential to reshape our understanding of fundamental physical principles, as researchers continue to delve deeper into the rich landscape of non-Hermitian physics and metamaterial design. The implications of these non-conventional systems are vast and promising, offering a glimpse into a future where unconventional materials and non-Hermitian phenomena play a pivotal role in shaping our world.

# References

1. Armitage, N. P., Mele, E. J. & Vishwanath, A. Weyl and Dirac Semimetals in Three Dimensional Solids. *Reviews of Modern Physics* **90**. doi:10.1103/RevModPhys.90.015001 (May 2017).
2. Xu, N. *et al.* Observation of Weyl nodes and Fermi arcs in tantalum phosphide. *Nature Communications* **7**, 11006. ISSN: 2041-1723. doi:10.1038/ncomms11006 (Mar. 2016).
3. Weyl, H. GRAVITATION AND THE ELECTRON. *Proceedings of the National Academy of Sciences* **15**, 323–334. ISSN: 0027-8424. doi:10.1073/pnas.15.4.323 (Apr. 1929).
4. Morimoto, T. & Nagaosa, N. Weyl Mott Insulator. *Scientific Reports 2016 6:1* **6**, 1–6. ISSN: 2045-2322. doi:10.1038/srep19853 (Jan. 2016).
5. Yan, B. & Felser, C. Topological Materials: Weyl Semimetals. <http://dx.doi.org/10.1146/annurev-conmatphys-031016-025458> **8**, 337–354. ISSN: 19475462. doi:10.1146/ANNUREV-CONMATPHYS-031016-025458 (Mar. 2017).
6. Ovchinnikov, D. *et al.* Topological current divider in a Chern insulator junction. *Nature Communications 2022 13:1* **13**, 1–6. ISSN: 2041-1723. doi:10.1038/s41467-022-33645-7 (Oct. 2022).
7. Wang, A. Q., Ye, X. G., Yu, D. P. & Liao, Z. M. Topological Semimetal Nanostructures: From Properties to Topotronics. *ACS Nano*. ISSN: 1936086X. doi:10.1021/ACS.NANO.9B07990/ASSET/IMAGES/MEDIUM/NN9B07990{\\_}0010.GIF (2020).
8. Moore, J. E. Optical properties of Weyl semimetals. *Natl Sci Rev* **6**. doi:10.1093/nsr/nwy164 (2019).
9. Kharzeev, D. E. & Li, Q. The Chiral Qubit: quantum computing with chiral anomaly. *Arxiv* (Mar. 2019).
10. Xu, S. Y. *et al.* Discovery of a Weyl fermion semimetal and topological Fermi arcs. *Science* **349**, 613–617. ISSN: 10959203. doi:10.1126/SCIENCE.AAA9297/SUPPL{\\_}FILE/XU.SM.PDF (Aug. 2015).
11. Chern, R. L. & Chou, Y. J. Photonic Weyl semimetals in pseudo-chiral metamaterials. *Scientific Reports 2022 12:1* **12**, 1–13. ISSN: 2045-2322. doi:10.1038/s41598-022-23505-1 (Nov. 2022).
12. Rafi-Ul-Islam, S. M., Bin Siu, Z. & Jalil, M. B. Topoelectrical circuit realization of a Weyl semimetal heterojunction. *Communications Physics 2020 3:1* **3**, 1–11. ISSN: 2399-3650. doi:10.1038/s42005-020-0336-0 (Apr. 2020).
13. Denner, M. M. *et al.* Exceptional topological insulators. *Nature Communications 2021 12:1* **12**, 1–7. ISSN: 2041-1723. doi:10.1038/s41467-021-25947-z (Sept. 2021).
14. Bergholtz, E. J., Budich, J. C. & Kunst, F. K. Exceptional topology of non-Hermitian systems. *Reviews of Modern Physics* **93**, 015005. ISSN: 15390756. doi:10.1103/REVMODPHYS.93.015005/FIGURES/7/MEDIUM (Feb. 2021).
15. Grushin, A. G. Introduction to topological Phases in Condensed Matter. *CNRS*. [https://grushingroup.cnrs.fr/wp-content/uploads/2021/06/intro\\_to\\_topo-5-1.pdf](https://grushingroup.cnrs.fr/wp-content/uploads/2021/06/intro_to_topo-5-1.pdf).
16. Ryu, S., Schnyder, A. P., Furusaki, A. & Ludwig, A. W. Topological insulators and superconductors: tenfold way and dimensional hierarchy. *New Journal of Physics* **12**, 065010. ISSN: 1367-2630. doi:10.1088/1367-2630/12/6/065010 (June 2010).
17. Chiu, C. K., Teo, J. C., Schnyder, A. P. & Ryu, S. Classification of topological quantum matter with symmetries. *Reviews of Modern Physics* **88**, 035005. ISSN: 15390756. doi:10.1103/REVMODPHYS.88.035005/FIGURES/14/MEDIUM (Aug. 2016).

18. Vasseur, R., Friedman, A. J., Parameswaran, S. A. & Potter, A. C. Particle-hole symmetry, many-body localization, and topological edge modes. *Physical Review B* **93**, 134207. ISSN: 24699969. doi:10.1103/PHYSREVB.93.134207/FIGURES/7/MEDIUM (Apr. 2016).
19. Yoshida, T., Peters, R., Kawakami, N. & Hatsugai, Y. Exceptional rings in two-dimensional correlated systems with chiral symmetry. *Physical Review B* **99**. doi:10.1103/PhysRevB.99.121101 (Oct. 2018).
20. Altland, A. & Zirnbauer, M. R. Nonstandard symmetry classes in mesoscopic normal-superconducting hybrid structures. *Physical Review B* **55**, 1142–1161. ISSN: 0163-1829. doi:10.1103/PhysRevB.55.1142 (Jan. 1997).
21. Alba Cazorla. *File:Rhoxy.jpg* 2020. <https://commons.wikimedia.org/wiki/File:Rhoxy.jpg>.
22. Abouzaid, A., Dai, J., Feiler, S., Kessler, P. & Waddell, C. The Integer Quantum Hall Effect. *University of British Columbia*. <https://phas.ubc.ca/~berciu/TEACHING/PHYS502/PROJECTS/18IQHE.pdf> (2018).
23. Thouless, D. J., Kohmoto, M., Nightingale, M. P. & Den Nijs, M. Quantized Hall Conductance in a Two-Dimensional Periodic Potential. *Physics Faculty Publications* **49**, 405–408. ISSN: 00319007. doi:10.1103/PhysRevLett.49.405 (Jan. 1982).
24. Thonhauser, T. & Vanderbilt, D. Insulator/Chern-insulator transition in the Haldane model. *Physical Review B - Condensed Matter and Materials Physics* **74**, 235111. ISSN: 10980121. doi:10.1103/PHYSREVB.74.235111/FIGURES/9/MEDIUM (Dec. 2006).
25. Haldane, F. D. Model for a quantum Hall effect without Landau levels: Condensed-matter realization of the. *Physical review letters* **61**, 2015–2018. ISSN: 00319007. doi:10.1103/PHYSREVLETT.61.2015 (1988).
26. Bernevig, B. A. & Hughes, T. L. Topological insulators and topological superconductors. *Topological Insulators and Topological Superconductors*. doi:10.1515/9781400846733/PDF (Mar. 2013).
27. Baocheng Zhu. *Lecture 2 : Berry Phase and Chern number — Physics 0.1 documentation* 2014. <https://phyx.readthedocs.io/en/latest/TI/Lecture%20notes/2.html>.
28. Meng, S. Integer Quantum Hall Effect. *ETHZ*. [https://ethz.ch/content/dam/ethz/special-interest/phys/theoretical-physics/itp-dam/documents/gaberdiel/proseminar\\_fs2018/07\\_Meng.pdf](https://ethz.ch/content/dam/ethz/special-interest/phys/theoretical-physics/itp-dam/documents/gaberdiel/proseminar_fs2018/07_Meng.pdf) (2018).
29. Batra, N. & Sheet, G. Understanding Basic Concepts of Topological Insulators Through Su-Schrieffer-Heeger (SSH) Model. *Resonance* **25**, 765–786. doi:10.1007/s12045-020-0995-x (June 2019).
30. Fukui, T., Hatsugai, Y. & Suzuki, H. Chern Numbers in Discretized Brillouin Zone: Efficient Method of Computing (Spin) Hall Conductances. *Journal of the Physical Society of Japan* **74**, 1674–1677. ISSN: 00319015. doi:10.1143/JPSJ.74.1674 (Nov. 2013).
31. Kitaev, A. Periodic table for topological insulators and superconductors. *AIP Conference Proceedings* **1134**, 22–30. doi:10.1063/1.3149495 (Jan. 2009).
32. Moore, J. E. & Balents, L. Topological invariants of time-reversal-invariant band structures. *Physical Review B - Condensed Matter and Materials Physics* **75**, 121306. ISSN: 10980121. doi:10.1103/PHYSREVB.75.121306/FIGURES/2/MEDIUM (Mar. 2007).
33. Ringel, Z., Kraus, Y. E. & Stern, A. The strong side of weak topological insulators. *Physical Review B - Condensed Matter and Materials Physics* **86**. doi:10.1103/PhysRevB.86.045102 (May 2011).
34. Fu, L., Kane, C. L. & Mele, E. J. Topological Insulators in Three Dimensions. *Physical Review Letters* **98**. doi:10.1103/PhysRevLett.98.106803 (July 2006).

35. Hasan, M. Z. & Kane, C. L. Topological Insulators. *Reviews of Modern Physics* **82**, 3045–3067. doi:10.1103/RevModPhys.82.3045 (Feb. 2010).
36. Fu, L. & Kane, C. L. Topological Insulators with Inversion Symmetry. *Physical Review B - Condensed Matter and Materials Physics* **76**. doi:10.1103/PhysRevB.76.045302 (Nov. 2006).
37. Weng, H., Dai, X. & Fang, Z. Exploration and prediction of topological electronic materials based on first-principles calculations. *MRS Bulletin 2014 39:10* **39**, 849–858. ISSN: 1938-1425. doi:10.1557/MRS.2014.216 (Oct. 2014).
38. Xie, B. *et al.* Dirac points and the transition towards Weyl points in three-dimensional sonic crystals. *Light: Science & Applications 2020 9:1* **9**, 1–9. ISSN: 2047-7538. doi:10.1038/s41377-020-00416-2 (Dec. 2020).
39. Soluyanov, A. A. *et al.* Type-II Weyl semimetals. *Nature 2015 527:7579* **527**, 495–498. ISSN: 1476-4687. doi:10.1038/nature15768 (Nov. 2015).
40. Halász, G. B. & Balents, L. Time-reversal invariant realization of the Weyl semimetal phase. *Physical Review B - Condensed Matter and Materials Physics* **85**, 035103. ISSN: 10980121. doi:10.1103/PHYSREVB.85.035103/FIGURES/5/MEDIUM (Jan. 2012).
41. Schnyder, A. P. Topological Semimetals. *Max-Planck-Institute*. [https://www.fkf.mpg.de/7143520/topological\\_semimetals.pdf](https://www.fkf.mpg.de/7143520/topological_semimetals.pdf).
42. Zhang, D., Wang, H., Ruan, J., Yao, G. & Zhang, H. Engineering topological phases in the Luttinger semimetal  $\text{Pb}_1-x\text{Sn}_x$ . *Physical Review B* **97**, 195139. ISSN: 2469-9950. doi:10.1103/PhysRevB.97.195139 (May 2018).
43. Wan, X., Turner, A. M., Vishwanath, A. & Savrasov, S. Y. Topological semimetal and Fermi-arc surface states in the electronic structure of pyrochlore iridates. *PHYSICAL REVIEW B* **83**, 205101. doi:10.1103/PhysRevB.83.205101 (2011).
44. Durnev, M. V., Budkin, G. V. & Tarasenko, S. A. Splitting of Dirac Cones in HgTe Quantum Wells: Effects of Crystallographic Orientation, Interface-, Bulk-, and Structure-Inversion Asymmetry. *Journal of Experimental and Theoretical Physics* **135**, 540–548. ISSN: 10906509. doi:10.1134/S106377612210003X/METRICS (Oct. 2022).
45. Thiang, G. C. On Spectral Flow and Fermi Arcs. *Communications in Mathematical Physics* **385**, 465–493. ISSN: 0010-3616. doi:10.1007/s00220-021-04007-z (July 2021).
46. Tsukerman, E. Inverse participation ratios in the XX spin chain. *Physical Review B* **95**, 115121. ISSN: 2469-9950. doi:10.1103/PhysRevB.95.115121 (Mar. 2017).
47. Kozii, V. & Fu, L. Non-Hermitian Topological Theory of Finite-Lifetime Quasiparticles: Prediction of Bulk Fermi Arc Due to Exceptional Point. *Arxiv* (Aug. 2017).
48. Schindler, F., Gu, K., Lian, B. & Kawabata, K. Hermitian Bulk – Non-Hermitian Boundary Correspondence. *PRX Quantum*. doi:10.1103/PRXQuantum.4.030315 (Apr. 2023).
49. Nakamura, D., Bessho, T. & Sato, M. Bulk-boundary correspondence in point-gap topological phases. *Arxiv* **46**, 106 (May 2022).
50. Heiss, W. D. The physics of exceptional points. *Journal of Physics A: Mathematical and Theoretical* **45**, 444016. ISSN: 1751-8121. doi:10.1088/1751-8121/45/44/444016 (Oct. 2012).
51. Denner, M. M. *Doctoral Thesis: Emergent non-Hermitian topology & unconventional orders in quantum materials* PhD thesis (UZH, Zurich, 2023).
52. Yang, Z., Schnyder, A. P., Hu, J. & Chiu, C. K. Fermion Doubling Theorems in Two-Dimensional Non-Hermitian Systems for Fermi Points and Exceptional Points. *Physical Review Letters* **126**, 086401. ISSN: 10797114. doi:10.1103/PHYSREVLETT.126.086401/FIGURES/2/MEDIUM (Feb. 2021).

53. Berry, M. V. Physics of nonhermitian degeneracies. *Czechoslovak Journal of Physics* **54**, 1039–1047. ISSN: 00114626. doi:10.1023/B:CJOP.0000044002.05657.04/METRICS (Oct. 2004).
54. Zhang, X., Zhang, T., Lu, M.-H. & Chen, Y.-F. A review on non-Hermitian skin effect. *Advances in Physics: X* **7**, 2109431. ISSN: 2374-6149. doi:10.1080/23746149.2022.2109431 (Dec. 2022).
55. Okuma, N., Kawabata, K., Shiozaki, K. & Sato, M. Topological Origin of Non-Hermitian Skin Effects. *Physical Review Letters*. doi:10.1103/PhysRevLett.124.086801 (Oct. 2019).
56. Zhang, K., Yang, Z. & Fang, C. Correspondence between winding numbers and skin modes in non-hermitian systems. *Physical Review Letters* **125**. doi:10.1103/PhysRevLett.125.126402 (Oct. 2019).
57. Gong, Z. *et al.* Topological phases of non-Hermitian systems. *Physical Review X*. doi:10.1103/PhysRevX.8.031079 (Feb. 2018).
58. Kawabata, K., Shiozaki, K., Ueda, M. & Sato, M. Symmetry and Topology in Non-Hermitian Physics. *Physical Review X*. doi:10.1103/PhysRevX.9.041015 (Dec. 2018).
59. Lee, C. H. *et al.* Topoelectrical Circuits. *Communications Physics 2018 1:1* **1**, 1–9. ISSN: 2399-3650. doi:10.1038/s42005-018-0035-2 (July 2018).
60. Qi, X.-L. & Zhang, S.-C. Topological insulators and superconductors. *Reviews of Modern Physics* **83**. doi:10.1103/RevModPhys.83.1057 (Aug. 2010).